Technische Universität Braunschweig
Leichtweiß-Institut für Wasserbau
Abteilung Hydromechanik und Küsteningenieurwesen
Prof. Dr.-Ing. Hocine Oumeraci

LWI Bericht. Nr. 944

Processes Affecting the Hydraulic Stability of Geotextile Sand Containers

-Experimental Studies-

DAAD Stipendiat M.Sc. Juan Recio
Professor Dr.-Ing. Hocine Oumeraci

BRAUNSCHWEIG
May 2007

Beethovenstraße 51a · 38106 Braunschweig · Telefon: 0531/391 3930 · Fax: 0531/391 8217
E-Mail: h.oumeraci@tu-bs.de · www.lwi.tu-bs.de

Table of Contents Page

Chapter 1: Wave Induced Flow on GSC-Structures

Chapter 2: Internal Movement of Sand inside GSCs

Beethovenstraße 51a · 38106 Braunschweig · Telefon: 0531/391 3930 · Fax: 0531/391 8217
E-Mail: h.oumeraci@tu-bs.de · www.lwi.tu-bs.de

Chapter 3: Wave Induced Forces on a Structure made of Geotextile Sand Containers (GSC)

Chapter 4: Preliminary Model Tests on the Stability of a GSC and a Geotextile Mattress Placed on the Seabed

Beethovenstraße 51a · 38106 Braunschweig · Telefon: 0531/391 3930 · Fax: 0531/391 8217
E-Mail: h.oumeraci@tu-bs.de · www.lwi.tu-bs.de

Process Affecting the Hydraulic Stability of Geotextile Sand Containers

-Experimental Studies-

Introduction

New shore protection structures such as seawalls, groins, breakwaters, revetments and artificial reefs are increasingly being developed. Softer and low cost protection alternatives, such as structures made of geotextile sand containers (GSC) are often used instead of more expensive and hard coastal structures made of concrete or rubble material.

To achieve a better understanding of the processes that affect the stability of GSC-structures several types of hydraulic model experiments and analyses were performed focusing on (i) wave induced flow on GSC-structures, (ii) internal movement of sand in the containers and its effect on the stability, (iii) wave-induced loads on the sand containers used for coastal structures and (iv) wave-induced loads on scour protection systems made with geotextile sand containers.

Chapter 1 shows the results obtained from model tests on the wave-induced flow around a GSC-revetment visualized by using PIV-techniques.

Chapter 2 is focused on the understanding of the internal movement of sand inside a container and its influence on the hydraulic stability of coastal structures made with geotextile sand containers.

Chapter 3 explains in detail the wave-induced loading on geotextile sand containers and its influence on the overall stability of the structure.

Chapter 4 summarizes the results and analysis obtained from model tests involving scour protection systems made of geotextile sand containers.

Based on the results of the experimental studies presented in this report, a better understanding of the processes which affect the stability of the coastal GSC-structures has been achieved.

Chapter 1

Wave Induced Flow on GSC-Structures
-Flow Visualisation using PIV-Techniques -

This chapter focus on the wave-induced flow around a GSC-revetment visualized by using PIV-techniques.

The **objectives** of this Chapter are:

(i) Clarification of the coherent structure of the flow on GSC-revetments.
(ii) The measurement of the spatial and temporal distribution of the velocity field on GSCs.
(iii) Derivation of pertinent data for the validation of a VOF-RANS type numerical model which is being used to investigate the stability of GSC-Structures.

1.1. PIV-Theoretical Background

The principle of Particle Image Velocimetry (PIV) is very simple. By adding tracer particles into a fluid, the particles follow the flow and the flow field can be visualized. The particles clarify the interaction between the flow and the structure. Images of the flow field can be analyzed to create velocity vectors throughout the entire flow field at any time step (Figure 1- 1).
In practice, however, the method is much more complicated. The details of the PIV-principles and theoretical background are explained in Annex 1.

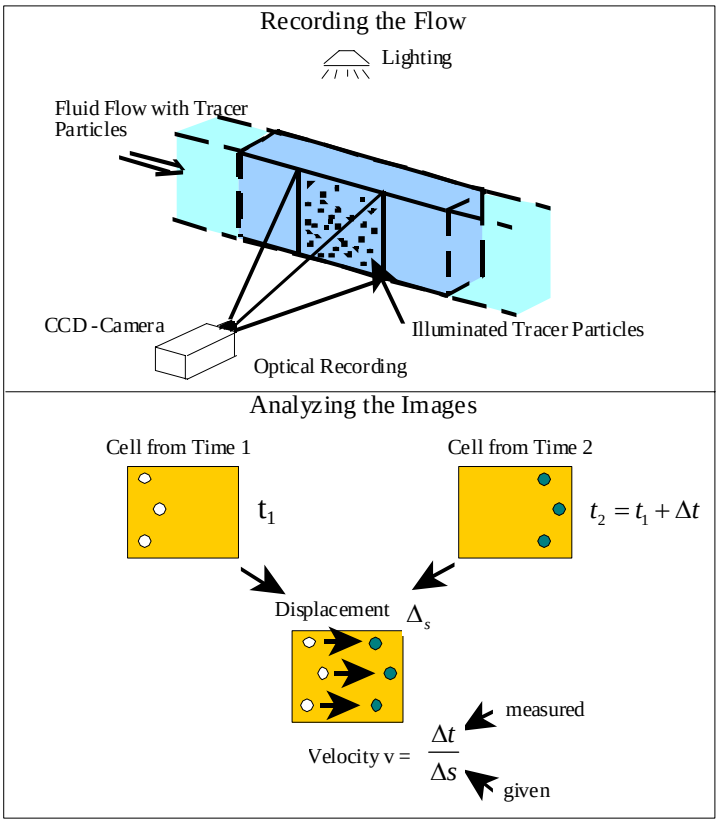

Figure 1- 1: The Principle of Particle Image Velocimetry (modified from Bleck, 2001)

1.2. Experimental Set-Up, Test Programme and Data Processing

A “low-cost” PIV flow visualisation system was implemented at LWI (Figure 1- 2). The wave flume from LWI was divided in two sections: (i) a “PIV” section and (ii) a “normal” section (Figure 1- 3). Inside the “PIV section”, a one column GSC-revetment was constructed (Figure 1- 3) and was subjected to different wave conditions (Table 1.1). Over the “PIV-section” two vibrating trays were constructed, from where the amount of tracer particles in the flow was controlled (Figure 1- 4). To visualize the flow, the “PIV section” was illuminated using halogen lamps (Figure 1- 4) and the flow was recorded using a specially design CCD-chip-camera. This camera and the PIV section were covered with a textile “tent” to avoid disturbance from other light (and noise) sources (Figure 1- 3). After the images were recorded, a specially designed PIV-software (DaVis-PIV) was used and the velocity vectors were processed (Section 1.3)

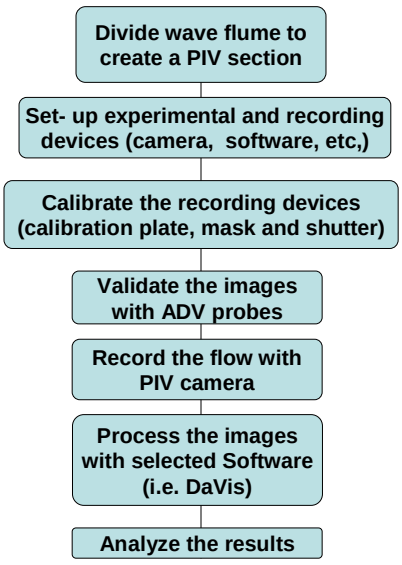

Figure 1.2: Implementation of a “Low Cost PIV”

The main characteristics of the PIV set-up are summarized in Figure 1- 5. The general PIV characteristics consisted in a measurement area of 2 x 1 meters, lighted with halogen lamps and using seeding particles with the same density as water.

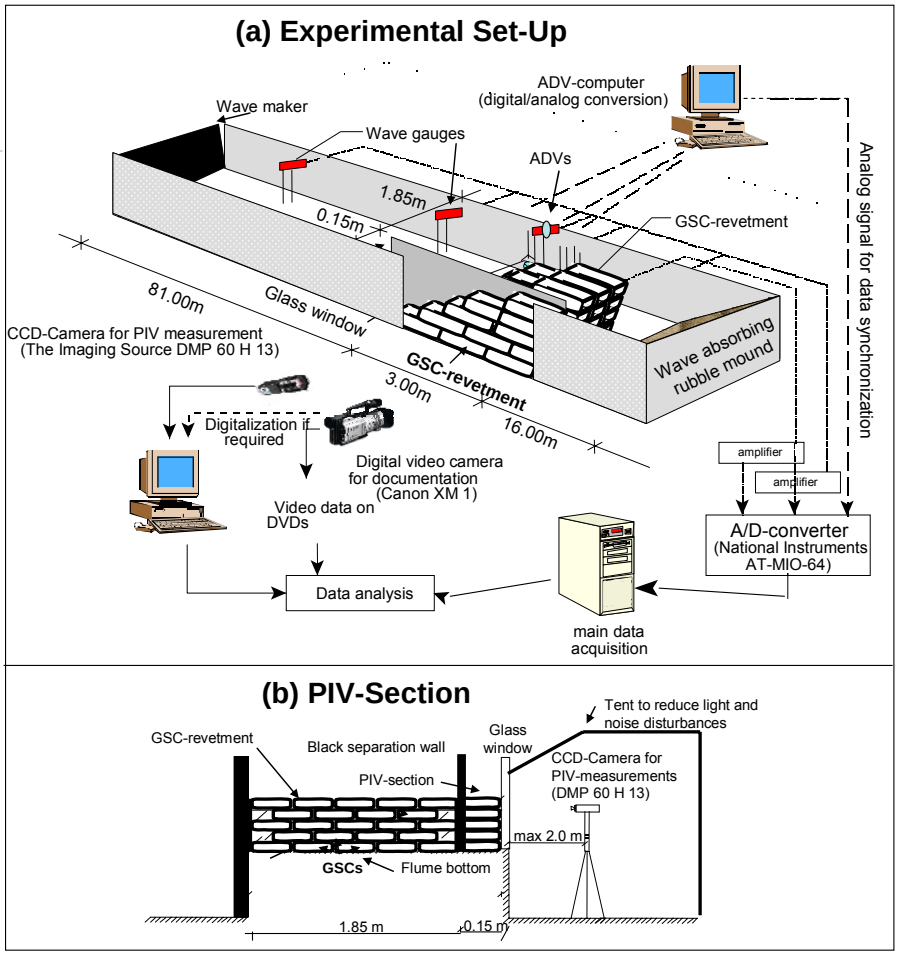

Figure 1- 3: Experimental Set-Up

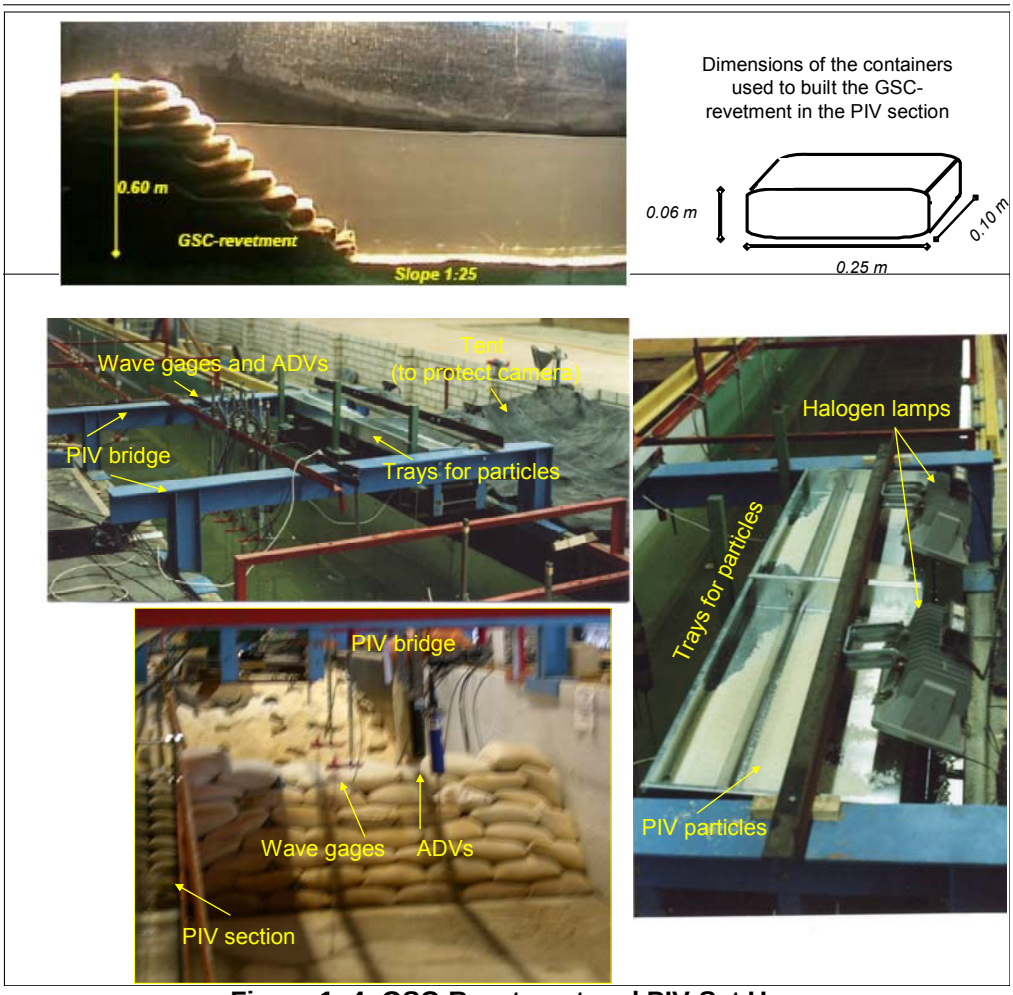

Figure 1- 4: GSC-Revetment and PIV-Set Up

(a) PIV General Characteristics

- Measurement area: 2.0 x 1.0m over a width of 0.15m (black training wall parallel to glass window)
- Seeding particles: PA12 Mix with $=\rho_s = 1.01 t/m^3$, d_s=3mm(≅1.3 Pixel) and w_{S0}=4.9cm/s
- Lightening: White light (2 x 1500 W and 1 x 500 W)
- Time interval between PIV-pictures: Δt=1/10s

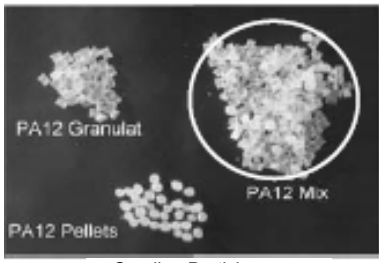

Seeding Particles

(b) CCD-Camera Characteristics

Camera	The Imaging Source DMP 60H13
CCD-chip	Sony ICX084AL: 1/3“, 659x494 Pixel, Pixel size 7.4x7.4 µm
Sampling frequency	30 Hz and 60 Hz
Scanning mode	Interlaced or progressive scan
Shutter	Electronically: off ÷ 1/10,000 s
Amplification	0-25 dB
Lens	f_n = 4.8 mm k_n = 1.8-16

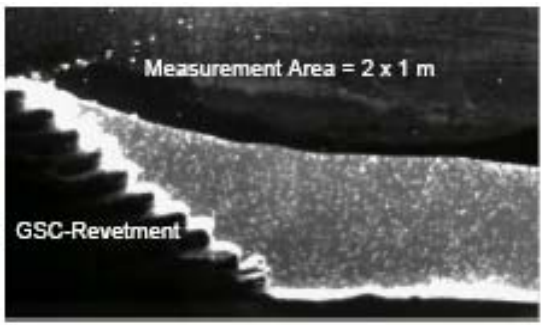

Figure 1- 5: Main Characteristics of PIV-Set-Up

Regular wave conditions generated in the flume are summarized in table 1.1:

Table1.1: Wave Parameters to be Used in the PIV Model Tests (Regular Waves)

		Wave Period (seconds)				
Depth (meter)	Wave Height (meter)	1.50	2.00	2.50	3.00	3.50
0.700	0.08		R	R	R	R
	0.12		R	R	R	
	0.16	R	R	R		
	0.20	R				
0.610	0.08		R	R	R	R
	0.12		R	R	R	
	0.16	R	R	R		
	0.20	R				
0.520	0.08		R	R	R	R
	0.12		R	R	R	
	0.16	R	R	R		
	0.20	R				

1.2.1 Measurements

1.2.1.1 Common Measurements and Observations

Water level elevations were recorded along the flume and near the revetment using common wave gauges. Acoustic Doppler Velocimeters (ADV) were used to measure the horizontal and vertical velocity at two points near the revetment and also to validate the PIV data (Figure 1- 6).
Digital video recordings were performed using commercially availably digital cameras.

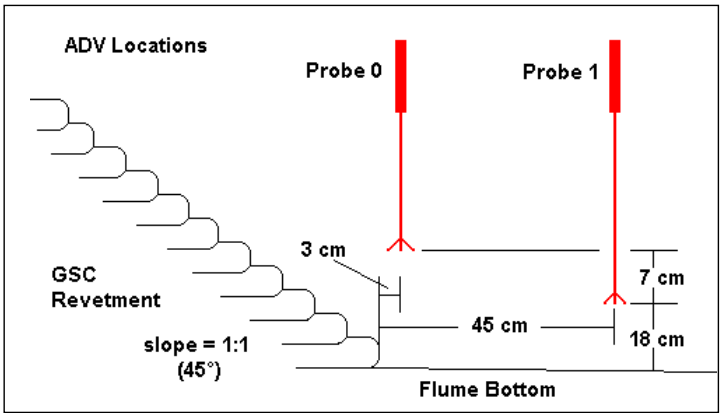

Figure 1- 6: Location of the Velocity Probes in the Wave-flume

1.2.1.2 Flow Visualisation and Optical Measurements

To get an insight into the coherent structure of the flow next to the revetment and the associated processes, the wave-induced flow was visualized by means of PIV-

techniques (the CCD-camera records the flow with the tracer particles for quantitative velocity measurements).

1.2.2 Calibration Tests and Data Processing

The measuring devices and PIV-camera and software (DaVis) were calibrated and adjusted before performing the model tests.

2.2.1 Calibration Plate

Since the lens of the CCD-camera consist in a “fisheye-type” lens (round lens), a **calibration plate** need to be fabricated to account for the “roundness” of the images (Figure 1- 7). On the calibration plate, crosses with equal distance were drawn (0.01m) to make the pertinent adjustments. Since the distance between the crosses is known, the software can account for the variation in velocity vectors due to the “roundness” of the images. In addition, the distance between crosses is used to convert the distances from pixels to meters (velocity = distance / time).

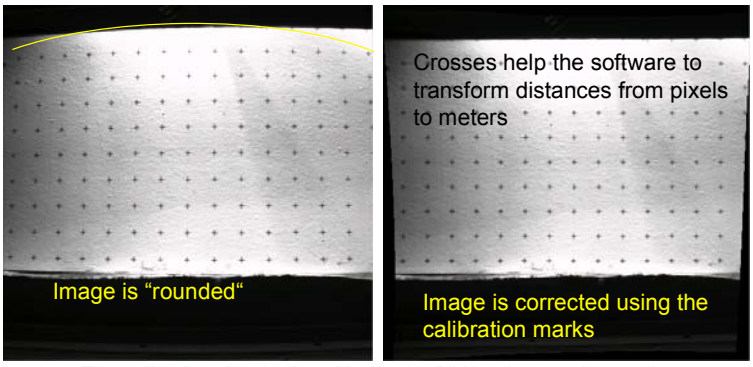

The calibration plate is placed inside the PIV section to calibrate distances

Figure 1- 7: Calibration Plate

1.2.2.2 Shutter Calibration

The CCD-camera can record up to 60 pictures per second; however, this velocity depends on the capacity of the used computer. In order to calibrate the shutter velocity, the camera was calibrated using a commercial watch (Figure 1- 8). The exact time between pictures could be obtained and thus, more accurate velocity vectors could be obtained.

Using a personal computer (512 MB in RAM) the maximal amount of reliable images per second is found to be 10. $(\Delta t = 1/10\,\mathrm{sec})$. With higher sampling rate, it was not guaranteed that the time within pictures will remain constant and thus, to assure reliable results, a maximal of 10 pictures per second were used for the analysis. For future analysis, it is recommended to use a PC with at least 1GHz processor.

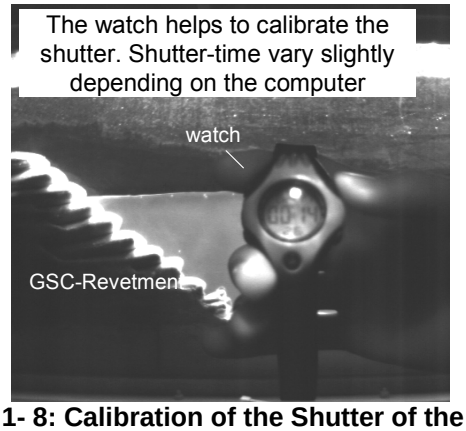

Figure 1- 8: Calibration of the Shutter of the camera

1.2.2.3 Mask

Finally, the area where the flow is going to be calculated needs to be defined. This is done by implementing a “Mask“ in the visualized area. Processing of velocity vectors is performed only in the areas outside the “mask”, thus saving computational time.

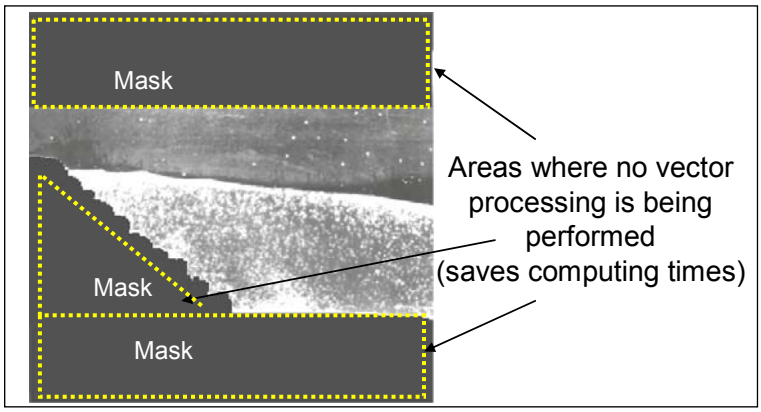

Figure 1- 9: Mask

1.2.2.4 Pre-processing

Pre-processing of the images was performed to subtract a sliding background or an offset in intensity of light in order to obtain better images (and thus velocity vectors). Subtraction of a sliding background is basically the application of a “filter” to the image to reduce any “noise” that might affect the calculation of velocity vectors. Figure 1- 10 shows vector fields for the same wave. The vector field on the left contains no pre-processing, while the vector field on the right does. It is clearly seen that by using pre-processing, thereby reducing background noise, it is possible to obtain a better, clearer, and more accurate vector field.

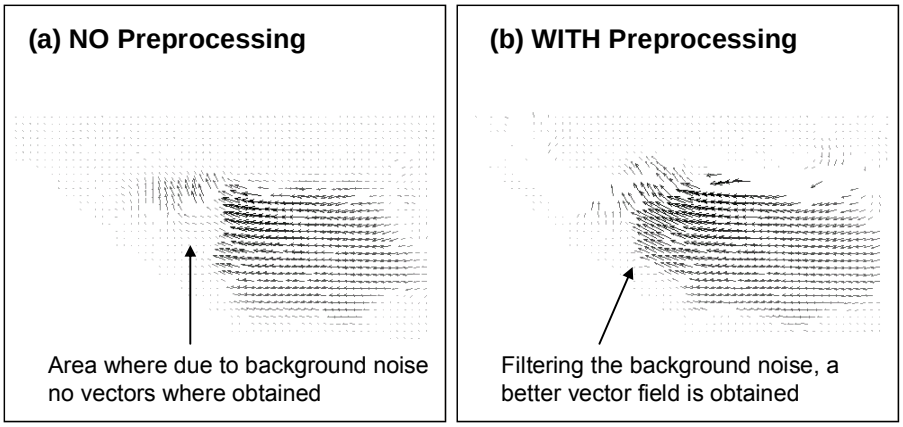

Figure 1- 10: Effect of using Pre-Processing on the Analysis of Velocity Vectors (Same wave for a) and b)

1.2.2.5 Image Processing

Processing of images is the most complicated and time consuming aspect of PIV. Processing the images is a rather complicated process. Details of the image processing can be found in Gemme (2005).

The recorded images were processed using a cross correlation method. This means that two consecutive images were used to process one velocity vector image. In each image “interrogation cells” were defined. These cells are the initial interrogation areas within the image, where the PIV-software will look for the displacement of the tracer particles (see Annex 1 and Raffell et al 1998 for more details). The PIV-software begins to calculate vectors within large interrogation cells and uses this as a reference vector field for the next calculation, which uses interrogation cells that are half the size of the initial cells. The final obtained “interrogation cells” are correlated using an FFT- algorithm (Fast Fournier Transformation) to obtain the desired velocity vectors.

1.2.2.6 Post-Processing

Finally, post-processing of the vector fields may be necessary to remove any false vectors. To perform this, first vectors that are not within a user specified range (given in pixels or m/s) are deleted. Vectors with Q-factor (the ratio of the highest correlation peak to the second highest peak) smaller than a given value are then deleted. With both of these post processing methods, there is danger of deleting good vectors, so caution and conservative values where used during post processing.

Another available option is to the fill the areas where no velocity vectors were obtained (due to noise and/or image limitations) by using average and statistical values of the neighbouring vectors. This option, however, was not implemented, since it was believed that these “calculated vectors” may not represent the actual flow.

1.3. Image Processing Results

First, the obtained velocity vectors were validated by comparing the results with the velocities recorded by the ADVs. The limitations of the PIV-system were quantified and finally, the wave-induced flow field was analyzed.

1.3.1 Validation of PIV Measurements

Regarding the fact that the set-up implemented at LWI does not correspond to a standard PIV system, simultaneous velocity measurements using ADVs (velocity probes) at two points in the flume were compared with the velocities evaluated at these points within the PIV measurements. Results were found to be in relatively good agreement (Figure 1- 11). However, not optimal correlation was obtained in waves with shorter periods (T=1.5s). This could be explained due to the fast change of direction of the flow that cannot be always recorded by the software.

1.3.2 Limitations of PIV Results

After processing the velocity vectors it was observed that the area next to the revetment was free of velocity vectors (Figure 1- 12). Several attempts were performed to try to improve the resolution in this area but the results were not satisfactory. The reasons behind this limitation may be summarized as follows:

(i) The containers reflect light and this causes a disturbance of the recording,
(ii) During up and downrush many bubbles appeared in the flow which disturb the recording process (specially with breaking waves).
(iii) Finally, the flow just next to the containers is very complex (very small vortices), which cannot be recognized by the PIV-software.

Therefore, the non-resolved flow was visualized and analyzed using digital documentation obtained from the CCD-camera and video camera (see next sections).

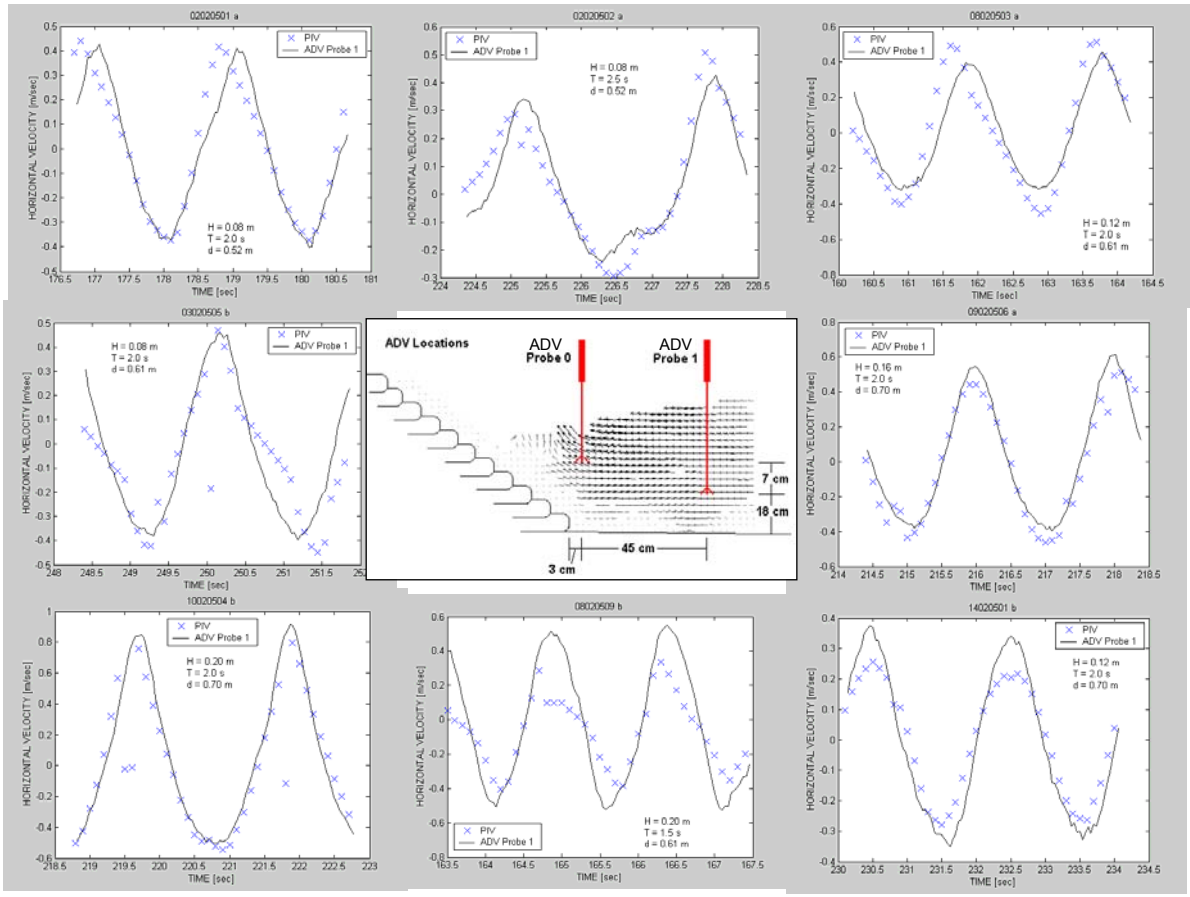

Figure 1- 11: Accuracy of PIV Measurements in Terms of Horizontal Velocity (PIV/ADV Correlation)

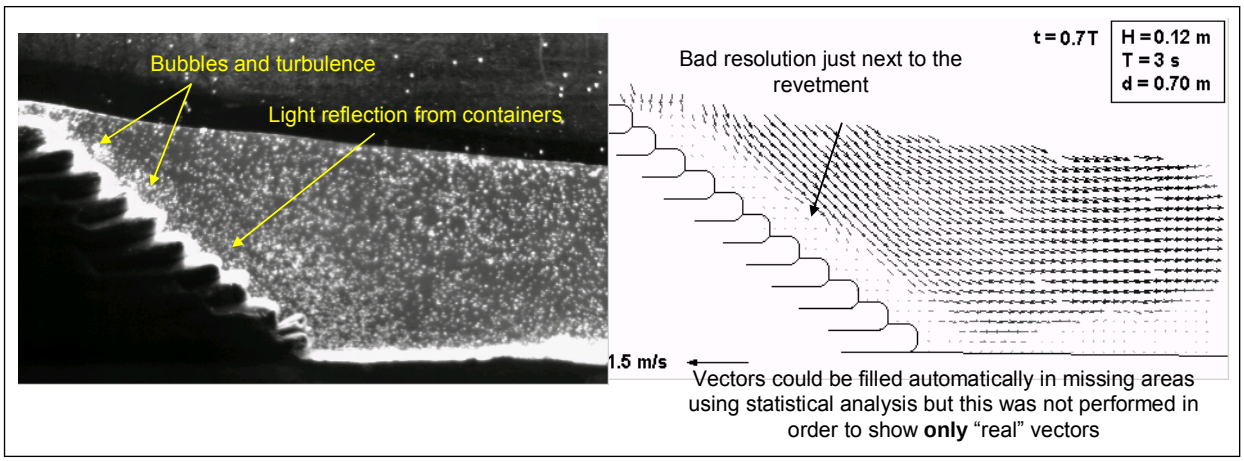

Figure 1- 12: Limitation of the PIV Results

1.4. Analysis of Flow Visualization

1.4.1 Global effects

For each model test (Table 1.1), several waves were recorded and the velocity fields were obtained. The velocity field as well as the visualization of the particles clarify the

flow process on the revetments. Figure 1-13 and 1-14 show examples of the processed data. The flow is better understood when the images are observed in rapid succession (“movie”). However, the Figures show clearly how the flow is changing at every phase of the wave. It was found that the flow in front of the revetment is initially an orbital flow induced by the wave motion.

Regarding the up and downrush, it was observed that the flow is separated into the main flow running up and down and local flows that are “trapped” between the containers (see local effects for details). The main flow vectors mostly occur during up and downrush parallel to the revetment slope.

Regarding the effect of wave breaking on the global effects it is found that the containers are flexible structures, are uplifted and deformed at the front part by the impact of the breaking waves. PIV techniques allowed the entire wave breaking process (Figure 1-15); however, after breaking, high turbulence interferes with the recording and no accurate vectors can be obtained.

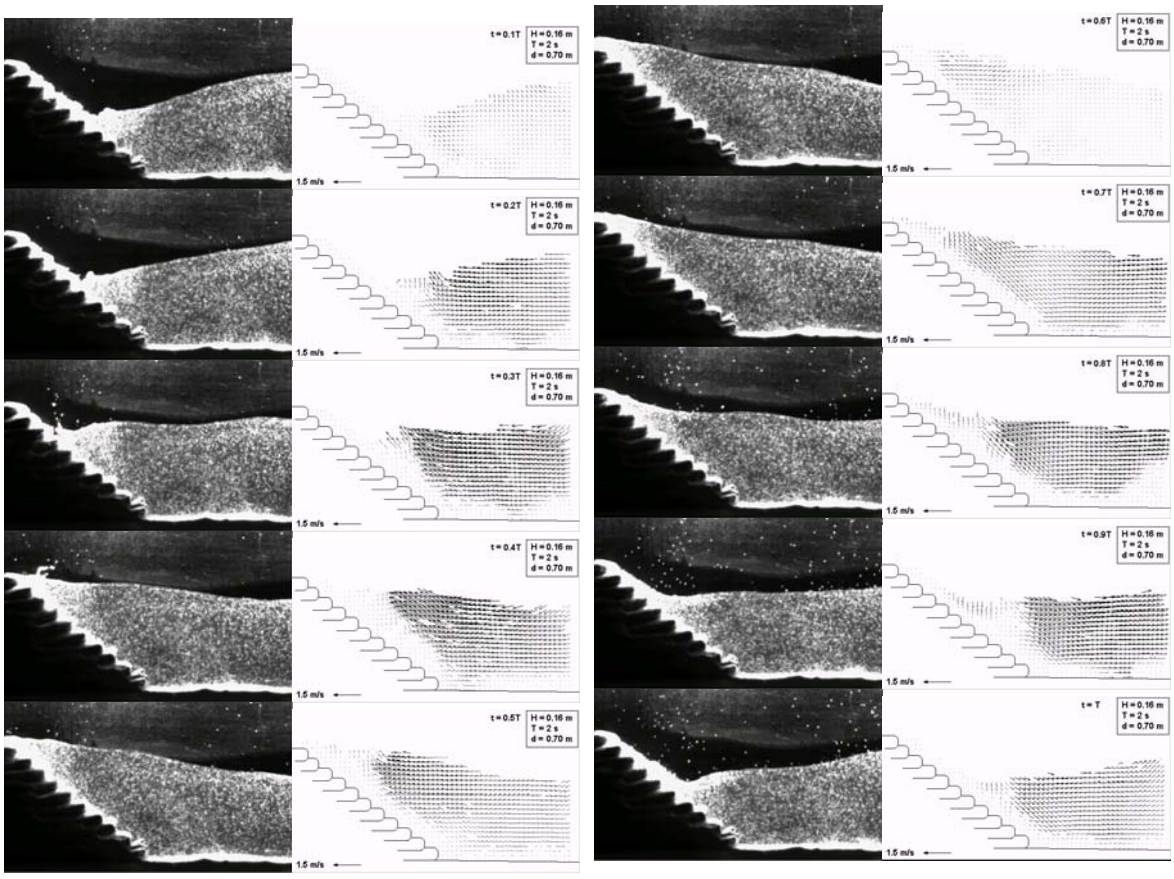

Figure 1- 13: Flow Visualization for a Wave Cycle (H=0.16m T= 2s)

Note: All processed data can be found in the “Student project work” conducted by Mister Douglas Gemme (Gemme 2005).

1.4.2 Local effects

Among the local effects at the revetment, vortex generation was investigated.

During wave action two different types of vortices were observed:

a) **Well structured vortices:** The motion is characterised by fluid particles moving around a common centre. These vortices are generated during up and downrush and appear in the areas between containers. These vortices affect the stability of the structure by applying a small rotational force on the container (Figure 1- 16).

b) **Non-structured vortices**: They occur during uprush with higher waves (higher than 0.12m) which break before reaching the revetment (Figure 1- 17).

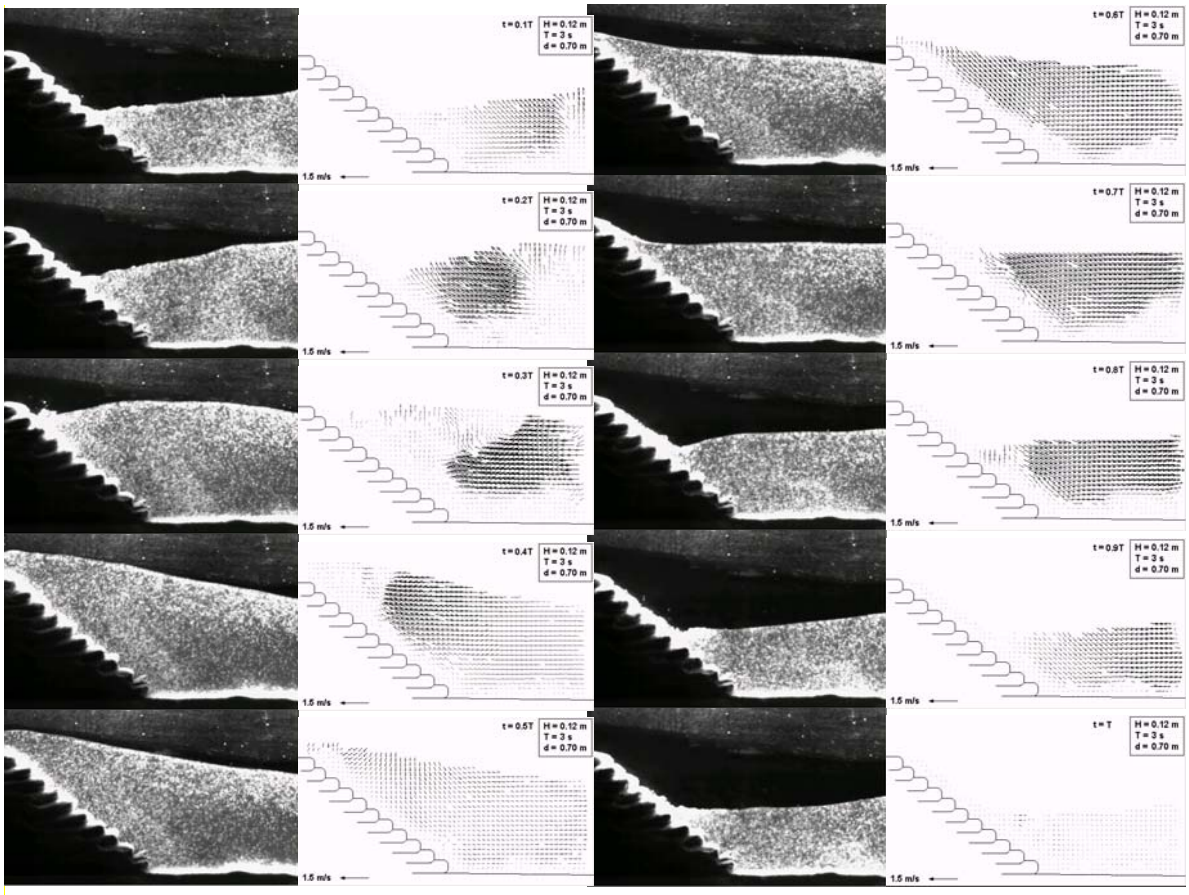

Figure 1- 14: Flow Visualization of a Wave Cycle (H=0.12m T= 3s)
(wave is recorded each 1/10 sec)

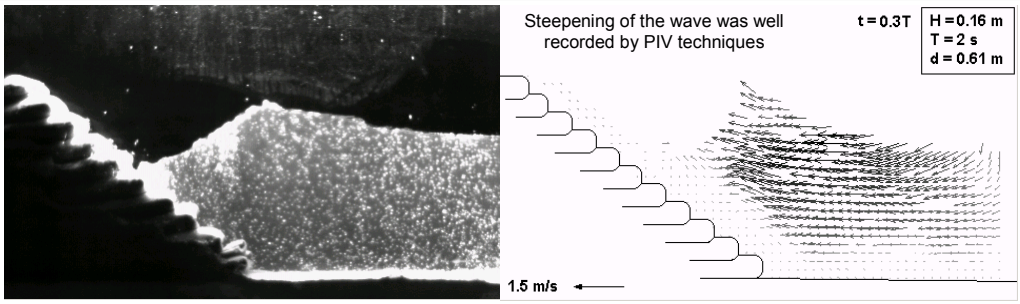

a) Wave Steepening

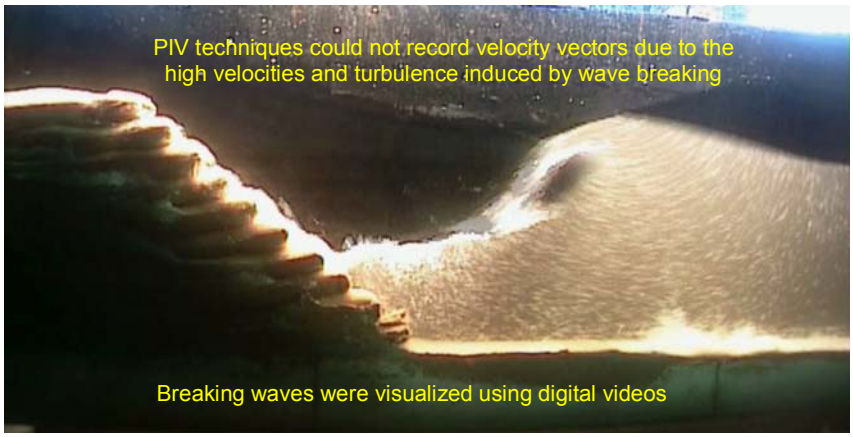

b) Wave Breaking

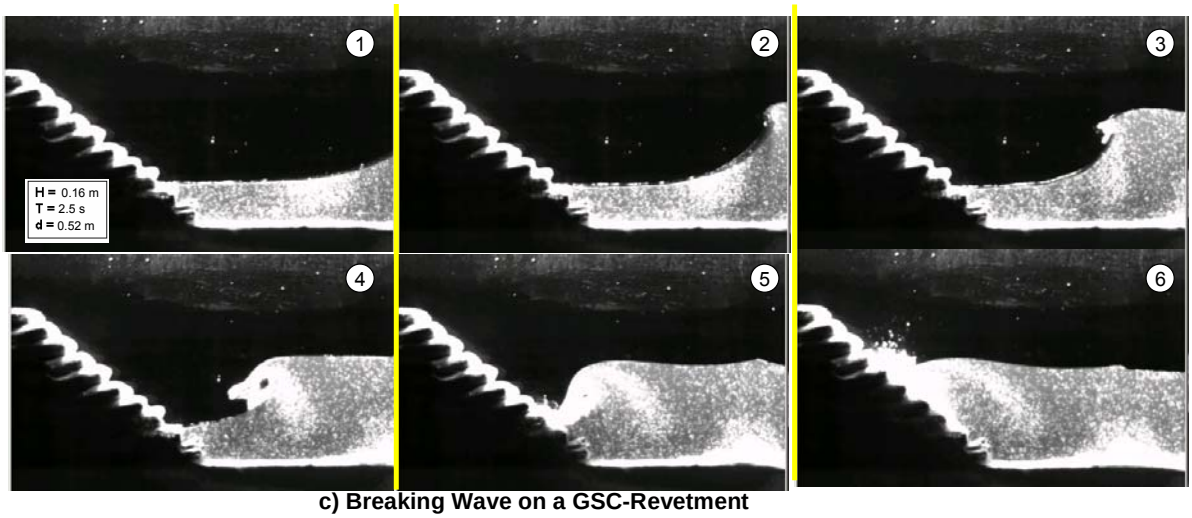

c) Breaking Wave on a GSC-Revetment

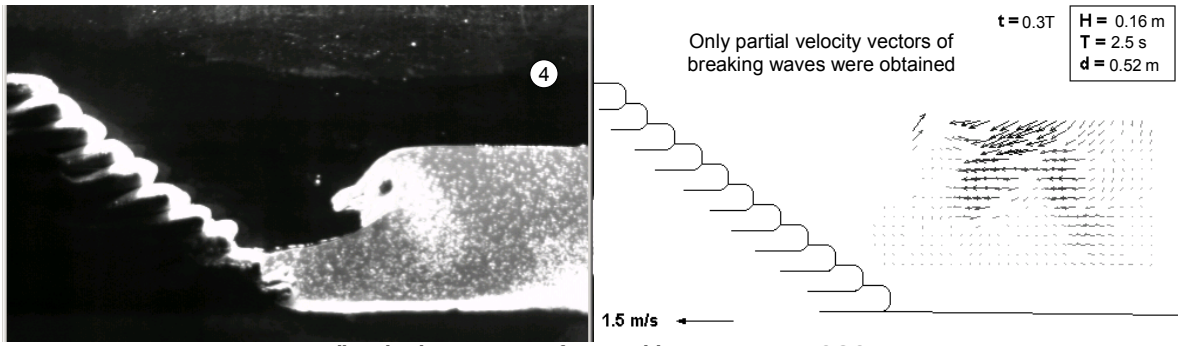

d) Velocity Vectors of a Breaking Wave on a GSC-Revetment

Figure 1- 15: Breaking Waves Recorded with PIV-techniques

Figure 1- 16: Vortices Appearance During Wave Up and Downrush

Figure 1- 17: Turbulence During Wave Up and Downrush of High Waves

1.5. Run-Up Friction Coefficient for GSC-Revetments

Based on the PIV-results, the run-up friction-coefficient for GSC-revetments was calculated. This coefficient is required for the prediction of the maximal run-up velocity and height.
The theoretical background for the run-up friction-coefficient as well as the procedure to obtain the latter are addressed.
The main objective of the following investigation is to determine a friction coefficient for GSC-revetments but also to set the basis for future analysis regarding uprush and overtopping of these revetments.

1.5.1 Theoretical Background

The results from a state of the art review on hydraulic processes affecting GSC-revetments (Recio 2004, Figure 1-18), have shown that no investigation was performed on wave run-up on GSC-revetments. Wave run-up is very important because it directly affects the stability of revetments.

The approach for obtaining wave up-rush velocities proposed by Schüttrumpf (2001) was used for obtaining the friction coefficient for GSC-revetments.

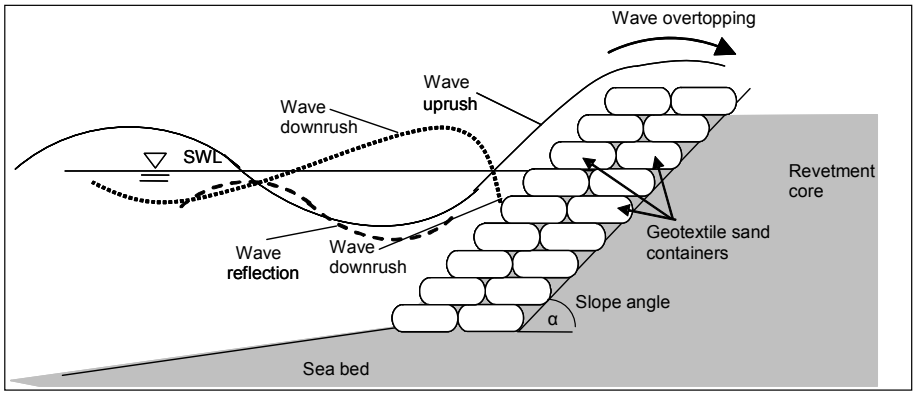

Figure 1- 18: Hydraulic Processes Affecting GSC-Revetments Subject to Wave Attack

Figure 1-19 shows the definition sketch proposed by Schüttrumpf (2001). The maximal run-up height depends on the maximal wave run-up velocity at SWL.

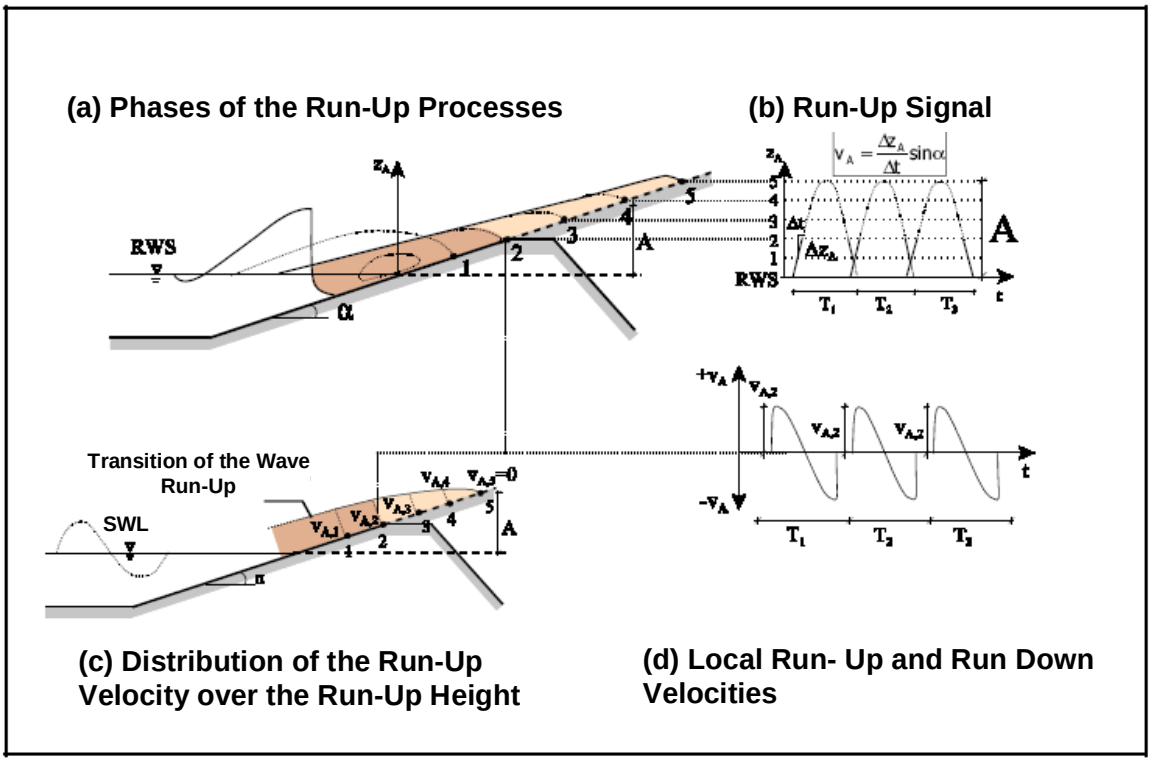

Figure 1- 19: Definition of Run-Up Velocities (after Schütrumpf 2001)

Considering that from the point $z_a(v_{a,max})$ a reduction of run-up velocity until the maximal run-up height takes place, then energy conservation will require:

$$\Delta E_{kin} - \Delta E_{pot} - \Delta E_{friction} = 0 \qquad (1)$$

with

variation of the kinetic energy $\Delta E_{kin} = \frac{m_g}{2}\left(v_{A,\max}{}^2 - \left[v_A(z_A)\right]^2\right)$ (2)

variation of the potential energy $\Delta E_{pot} = m_g \cdot g \cdot z_A$ = (3)

variation of the friction energy $\Delta E_{friction} = f(v_A, h_A, z_A, roughness)$ (4)

$h_A(z_A)$ = thickness of the wave run-up
m_g= mass of water
$z_A(v_{A,max})$= height on the revetment slope where the maximal run-up velocity occurs.
$v_A(A)$=0 = maximal wave run-up height

Using equation (1) together with equations 2, 3 and 4 yields:

$$v_A(z_A) = \sqrt{v_{A,\max}^2 - 2 \cdot g \cdot z_A - \Delta E_{friction}} \quad (5)$$

This equation is the basis for most of wave run up investigations (Shen u.Meyer, 1963; Freeman u. Le Méhauté, 1964; Franzius, 1965; Tautenhain, 1981; Van der Meer u. Klein Breteler, 1990; Schüttrumpf et al., 2000)

The influence of the friction is obtained through an empirical coefficient k^*
The maximal wave up run velocity $v_{a,max}$ is then obtained with:

$$v_{A,\max} = k^* \cdot \sqrt{2 \cdot g \cdot A} \quad (6)$$

where $v_{a.max}$ is valid only for SWL (z_A=0)

1.5.2 Wave Run-Up Friction Coefficient for GSC-Revetments

Considering equations 2, 3 and the results obtained from PIV-model tests, the maximal run-up velocity and the run-up height could be easily obtained.
Therefore an attempt to obtain the friction coefficient k^* was performed by using the results from model tests without wave overtopping (Figure 1- 20 and Table 2).

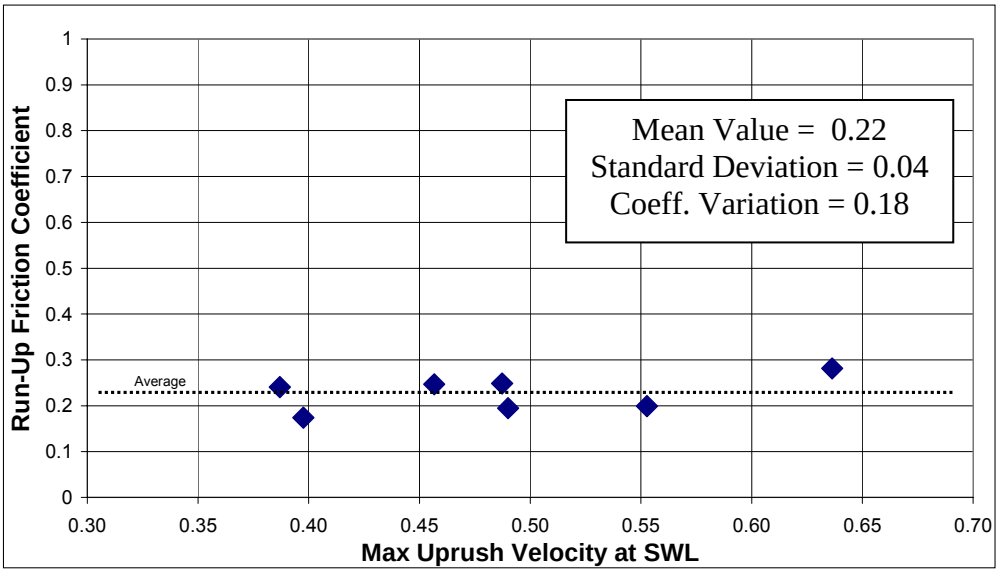

Figure 1- 20: Friction Coefficients for GSC-Revetments

It can be seen that the run-up friction coefficient is about 0.22. This value is reasonable considering that for a perfectly smooth slope is around 1 (Shen et al 1963 $k^*= 1$, Franzius 1965 $k^*= 1$, Tautenhain 1981 $k^*= 0.97$). The unevenness of the slope of GSC-revetments makes it very rough, thus, causing a considerable reduction of the wave run up velocity (see also model tests with a transparent container).

Table 1.2: Model Test Results Used to determine the run up friction coefficient

Exp No.	H	T	d	Vmax m/s	Vmin m/s	R Uprush (m)	k*
02020501a	0,08	2,00	0,52	0,46	-0,32	0,17	0,25
02020503b	0,08	3,00	0,52	0,49	-0,58	0,32	0,19
02020504a	0,12	2,00	0,52	0,64	-0,33	0,26	0,28
02020505b	0,12	2,50	0,52	0,55	-0,36	0,39	0,20
03020505b	0,08	2,00	0,61	0,40	-0,35	0,27	0,17
08020501c	0,08	2,50	0,61	0,49	-0,37	0,20	0,25
08020502c	0,08	3,00	0,61	0,39	-0,23	0,13	0,24

1.5.3 Friction Factor for Roughness for GSC-Revetments

Additionally the friction factor for roughness of a GSC revetment was obtained. This factor is used when the maximal run up height needs to be obtained from wave parameters (*H* and *T*).

Wave run-up is often indicated by $R_{u2\%}$, the run-up level, vertically measured with respect to the still water level (SWL), which is exceeded by two per cent of the incoming waves. The relative run-up is given by $R_{u2\%}/H_s$, with H_s being the significant wave height.
The relative run-up is usually given as a function of the surf similarity parameter:

$$\xi_o = \tan\alpha / \sqrt{\frac{H_o}{L_o}} \qquad (7)$$

where α is the slope angle of the revetment, H_o/L_o the deepwater wave steepness, H_o is the deepwater wave height, L_o is the deepwater wavelength ($gT2/2\pi$), T the wave period, g the gravitational acceleration. Moreover, the general design formula for wave run-up for a revetment is:

$R_{u2\%} / H_s = 1.6\gamma_b\gamma_f\gamma_\beta\xi_o$ with a maximum of 3.2 $\gamma_f\gamma_\beta$ (8)

with γ_b being reduction factor for a berm, γ_f being the reduction factor for slope roughness and γ_β the reduction factor for oblique wave attack. Considering equation (8) and considering γ_b and γ_β equal to 1 and using data from the model tests, the reduction factor for slope roughness γ_f was derived. The roughness reduction factor for GSC-revetments is 0.24 with a standard deviation of 0.07.

The conclusions from this section (section 1.5) can be summarized as follows:

(i) The run-up friction-coefficient for GSC-revetments with no-breaking waves with a slope of 1:1 is approx 0.22 with a standard deviation of σ=0.04.
(ii) The reduction factor for slope roughness is approx 0.24 with a standard deviation of 0.07.

1.6. Conclusions

The conclusions of all the PIV model tests and analyses are summarized as follows:

(i) The structure of the flow around GSC-revetments has been clarified.
(ii) It was found that the wave particles follow orbital trajectories until they reach the revetment, then the up and downrush flow is divided into a main flow and local flow that is trapped between the containers.
(iii) The main flow is essentially parallel to the revetment slope
(iv) Vortices are generated between the containers and could affect the stability of the containers.
(v) Pertinent data for validating a numerical flow model such as a RANS-VOF was obtained.
(vi) A run –up friction coefficient for GSC-revetments for no-breaking waves was obtained from model tests (f=0.22)
(vii) The limitations of a “low cost” PIV-set-up were quantified to improve future PIV projects at LWI showing that the low-cost PIV-system originally proposed by Bleck and Oumeraci (2001) can be reliably used to visualize wave-induced flow on coastal structures.

Acknowledgments

- The financial support of the first author by DAAD (Deutsche Akademischer Austausch Dienst) is deeply appreciated.
- Geotextiles for the sand containers and technical support was provided by NAUE GmbH & Co. KG
- The model tests were supported by the Leichtweiss Institute.
- The experimental set-up was constructed with the continuous help, support and advice obtained from Dr. Mattias Bleck.
- The PIV images were processed with the help of Mister Douglas Gemme.

Their help to this project is deeply appreciated.

References:

PIV Theory and Theoretical Background:

LaVision 1999 DaVis PIV Manual; LaVision, Göttingen

LaVision 2000 PIV FlowMaster Manual; LaVision, Göttingen

Raffel, M.; Willert, C.; and Kompenhans, J. (1998) Particle Image Velocimetry – A Practical Guide; Springer Verlag, Berlin, Heidelberg, New York

“Low Cost PIV-Techniques” at LWI:

Bielenberg, B. 2000. Geschwindigkeitmessungen an künstlichen Riffen zur Entwicklung eines innovativen Bemessungsansatzes, Diplomarbeit, LWI, Germany (in German)

Bleck, M. and Oumercaci H. 2003. Hydraulische Wirksamkeit künstlicher Riffe am Beispiel einer rechteckigen Struktur, PhD Thesis, LWI, Germany (in German)

Bleck, M. and Oumercaci H. 2001 Hydraulische Wirksamkeit von künstlichen Riffen unter besonderer Berücksichtigung des Energietransfers im Wellenspektrum, Bericht Nr. 863, LWI. Germany (in German)

PIV-Analyses:

Bleck, M. and Oumeraci, H. 2004. Hydraulic Performance of Artificial Reefs: Global and Local Description, Proceedings of the 28th ICCE 2002, pp. 1778-1790, Cardiff, Wales

Gemme D. 2005, application of PIV to Determine Wave Induced Velocities on a GSC Revetment, Student work, LWI.

Kendall M., Veron F., 2002, The Velocity Field under Breaking Waves, Journal of Fluid Mechanics, Cambridge University Press. Vol. 454 Pages 203-233

Oumeraci H., Bruce T. Klammer. P. Easson W. J.1995, PIV-Measurement of Breaking Wave Kinematics and Impact loading Of Caisson breakwaters, Proceedings International Conference on Coastal and Port Engineering in Developing Countries (COPEDEC), Rio de Janeiro, vol. 4, Part 3, pp. 2394-2410.

Friction Coefficients on Revetments:

Oumeraci H., Literature Review on Wave Run-Up Velocities, Internal Report, LWI.

Schüttrumpf H. 2001, Wellenüberlaufströmung bei Seedeichen (Experimentelle und theoretische Utersuchungen), PhD Thesis, LWI

Pilarczyk K. 1998, Dikes and Revetments, design, maintenance and safety assessment, A.A. Balkema, Rotterdam, the Netherlands.

Recio J., 2004. Hydraulic Processes on GSC-Revetments, Short Progress Report, LWI.

Annexes:

Annex 1: “Theoretical Background of PIV”

Chapter 2

Internal Movement of Sand inside a Geotextile Sand Container (GSC)

Several types of model tests of GSC-revetments were performed at Leichtweiß Institute (LWI) and at the Large Wave Flume (GWK) in Hanover (Hinz and Oumeraci 2002). However, observations of sand movements inside the containers were impossible to be performed. In addition, the variations of the contact area between neighbouring containers during wave action and its influence of the stability have not been investigated. Therefore, to quantify the variation of contact areas during wave action and to understand the internal movement of sand inside a container, several types of model tests involving a transparent permeable container were performed.
This Chapter is divided in three parts: (i) first, the experimental set-up implemented at LWI is briefly explained, followed by (ii) the results and analysis obtained from the model tests involving the transparent container and finally, (iii) the quantification of the variation of contact areas between neighbouring containers is discussed.

2.1. Experimental Set-Up

The model tests consist in a GSC-revetment built in the wave-flume of the LWI. Instead of a normal geotextile container, a container made of a transparent, permeable material was used. The filling material inside the transparent container consisted in different layers of sand with the same properties but different colours. The transparent container was laid next to the wave-flume window to record its internal movement of sand during wave action (video observations). The transparent container was large enough to observe easily the variations of the contact area during a wave cycle, but also small enough to suffer normal uplift deformations (Figure 2-1).

The **main objectives** of the model tests are:

(i) Observation and quantification of the internal movement of sand in the container during wave action. Its influence on the actual contact area and the effect of the movement of sand on the stability.
(ii) Quantification of the variation of the contact areas between neighbouring containers during wave action.

2.1.1 Materials Used in the Model Tests

A transparent and permeable plastic bag was selected as a transparent testing container. The holes in the bag are big enough to allow water to flow but small enough to retain the sand grains (Figure 2- 2).

The transparent bag was filled with **coloured sand**. The size of the transparent container was 0.40 m x 0.14 m x 0.07m (Figure 2- 5). The procedure for colouring the sand followed normal procedures used in soil mechanics: (i) sand was dyed with special ink, then (ii) putted into an oven to make the colour permanent and finally, filling of the container with the coloured sand (Figures 2-3 and 2-4).

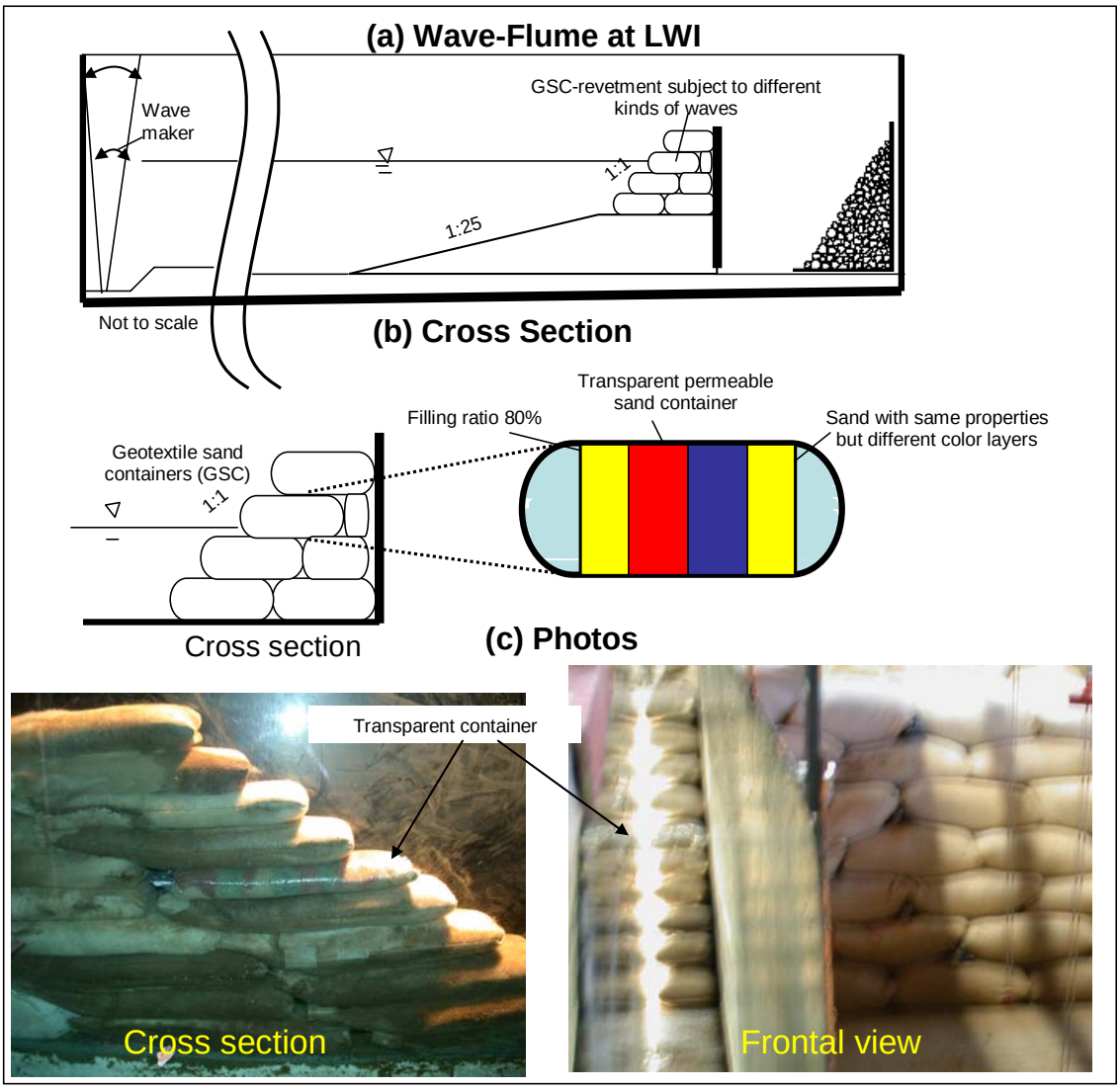

Figure 2- 1: Transparent GSC subject to Wave Action in the Wave-flume from LWI

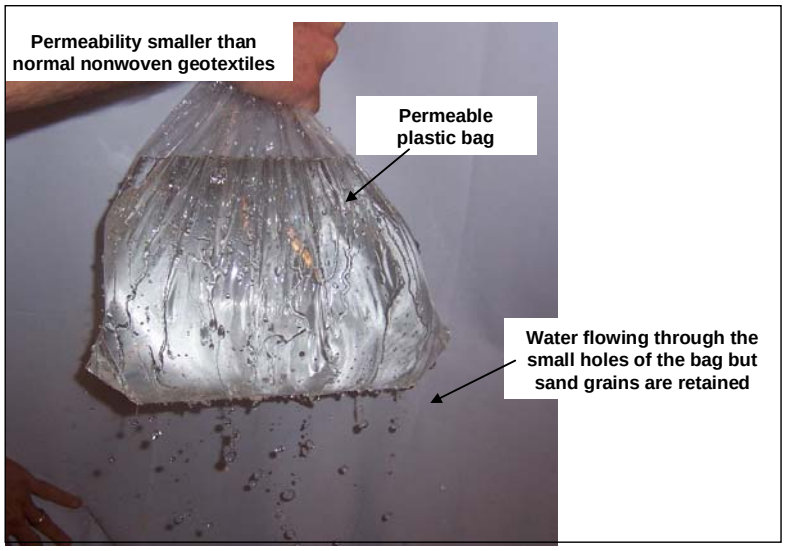

Figure 2- 2: Transparent-Permeable Bag Used as Container in the Model Tests

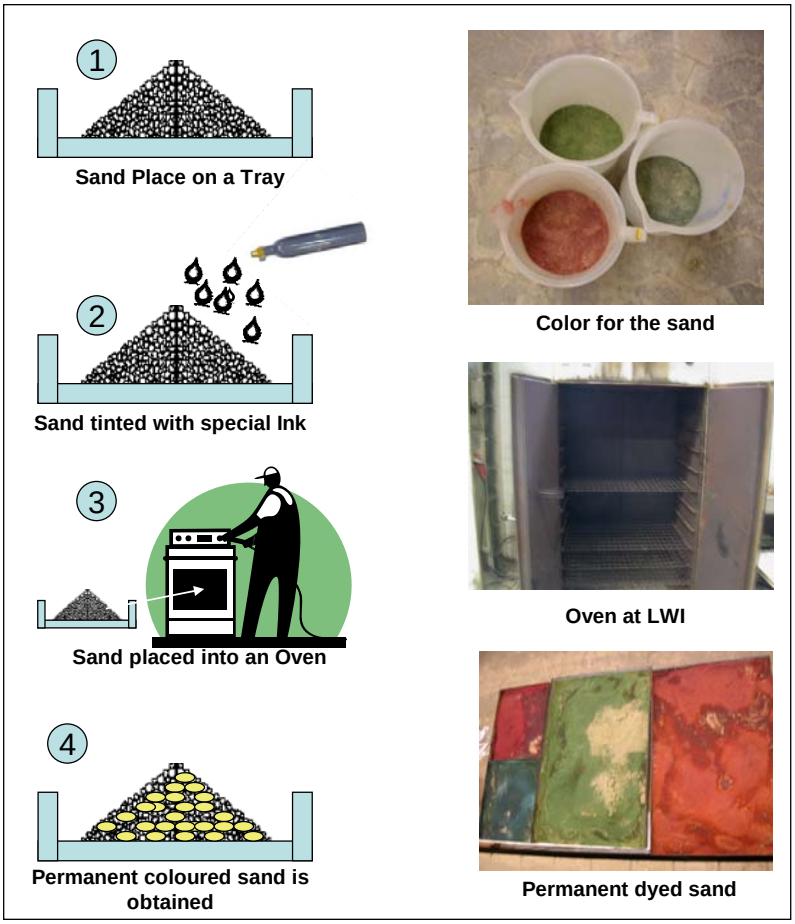

Figure 2- 3: Colouring Procedure of Sand

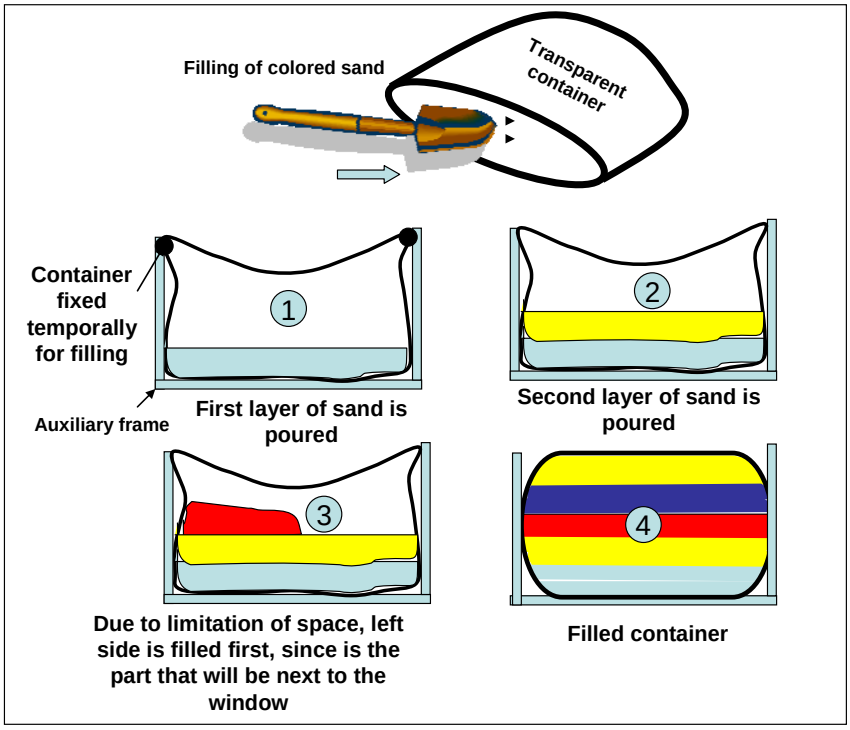

Figure 2- 4: Filling Procedure of the Transparent Bag

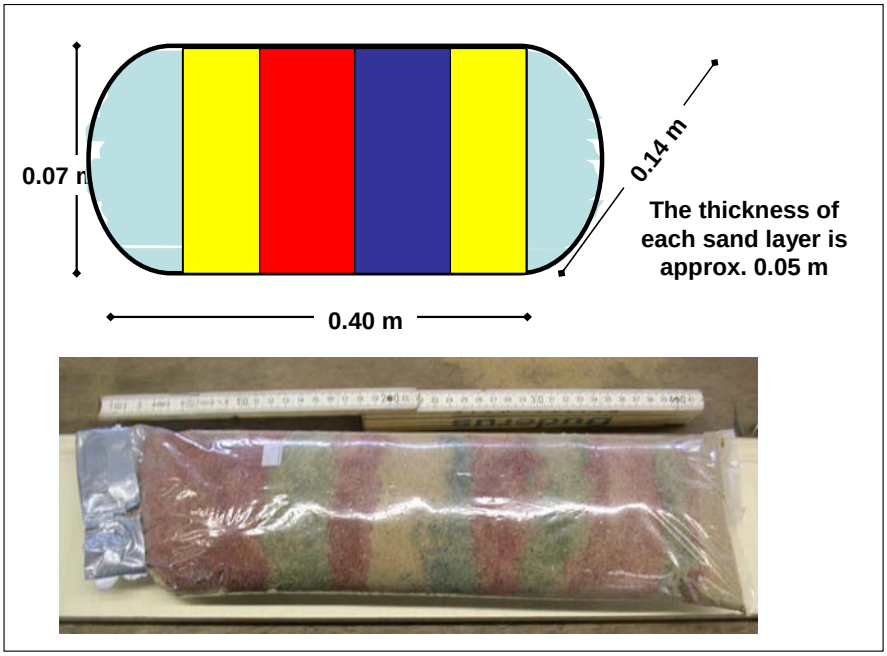

Figure 2- 5: Dimension of Transparent Bag and Thickness of Coloured-sand Layers

2.1.2 Wave Parameters

Regular waves were used during the model tests (Table 2.1).

Table 2.1: Wave parameters used in the Model Tests (Regular Waves)

		Wave Period (seconds)						
Depth (meter)	**Wave Height (meter)**	**1.50**	**2.00**	**2.50**	**3.00**	**3.50**	**4.00**	**4.5**
0.620	**0.16**			**R**				
	0.20		**R**					

High wave conditions were used to induce large movements of the sand inside the container. It was observed from previous model tests (without transparent container) that all deformations followed the same pattern. Therefore only two wave conditions were tested.

2.1.3 Visual Observation Procedure

The main measurements of these experiments were recorded by using two video cameras. One video camera was used record only a large and clear image of the container. The second video camera recorded the entire revetment (Figure 2- 6).

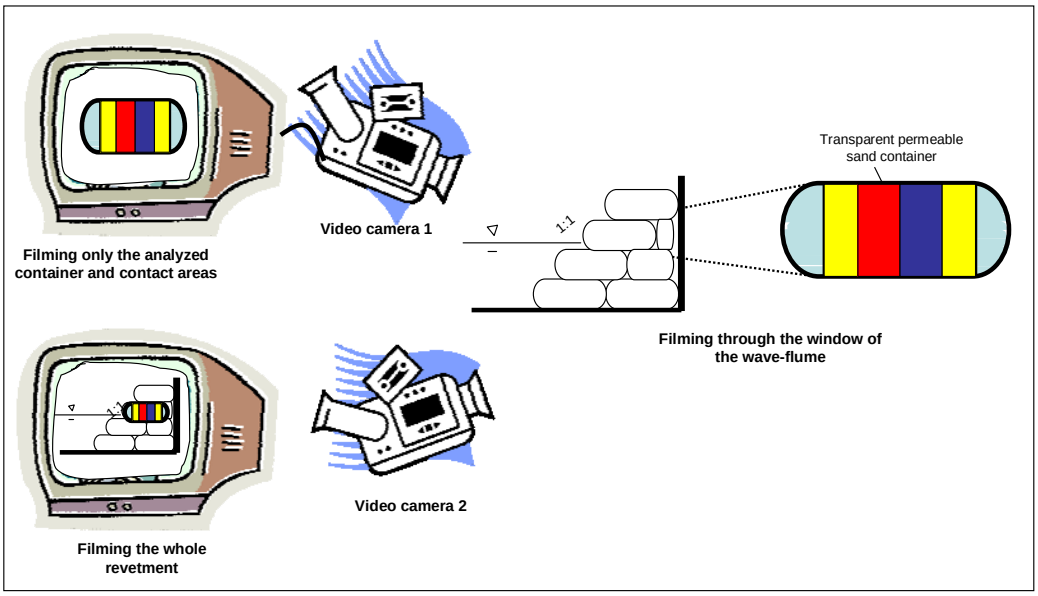

Figure 2- 6: Video Recordings

2.2. Selected Model Test Results

2.2.1 Movement of Sand inside the GSC

The observations of the coloured sand in the transparent permeable container subject to wave attack have shown that (Figures 2-7):

(i) Similar pattern of the sand motion occur for different wave conditions. As expected, noticeable movements of sand are only induced by larger incident waves.

(ii) The largest sand movements occur during the first 30 wave cycles, which then rapidly decrease. This means that the sand fill re-accommodates due to the wave induced forces on the container.

(iii) During wave uprush the dominant sand movement is rather rotational and directed upward (Figures 2-7a).

(iv) During wave downrush the movement is essentially directed seaward (Figures 2-7b). At this stage, displacement of the container occurs as soon as a given critical wave height is exceeded.

(v) After few wave cycles, the sand accumulates at the seaward end of the container, causing a deformation of the latter and reducing the contact areas with neighbouring containers (Figures 2-7c).

(vi) Conditions prevail (v) as long as no further horizontal displacement of the container occurs, internal movements of sand are triggered by any incremental horizontal displacement of the container. These movements of sand occur, because the contact areas of the GSC with the neighbouring containers are reduced. As a result, the entire process of sand movement will again repeat itself in a similar way as during the first wave cycles. (Figures 2-7d).

The clarification of the internal movement of sand inside GSCs proves that the deformation of a GSC affects the stability of GSC-structures. On the other hand, this conclusion has some very important implications for the construction of GSC-structures. As explained in Figures 2-7, the displacement of each GSC depends on the internal movement of the contained sand, thus, the filling ratio of each GSC is critical for the stability. A GSC with very low filling ratio will be much more

unstable as a GSC with an optimal filling ratio (balance between flexibility and small movement of sand).

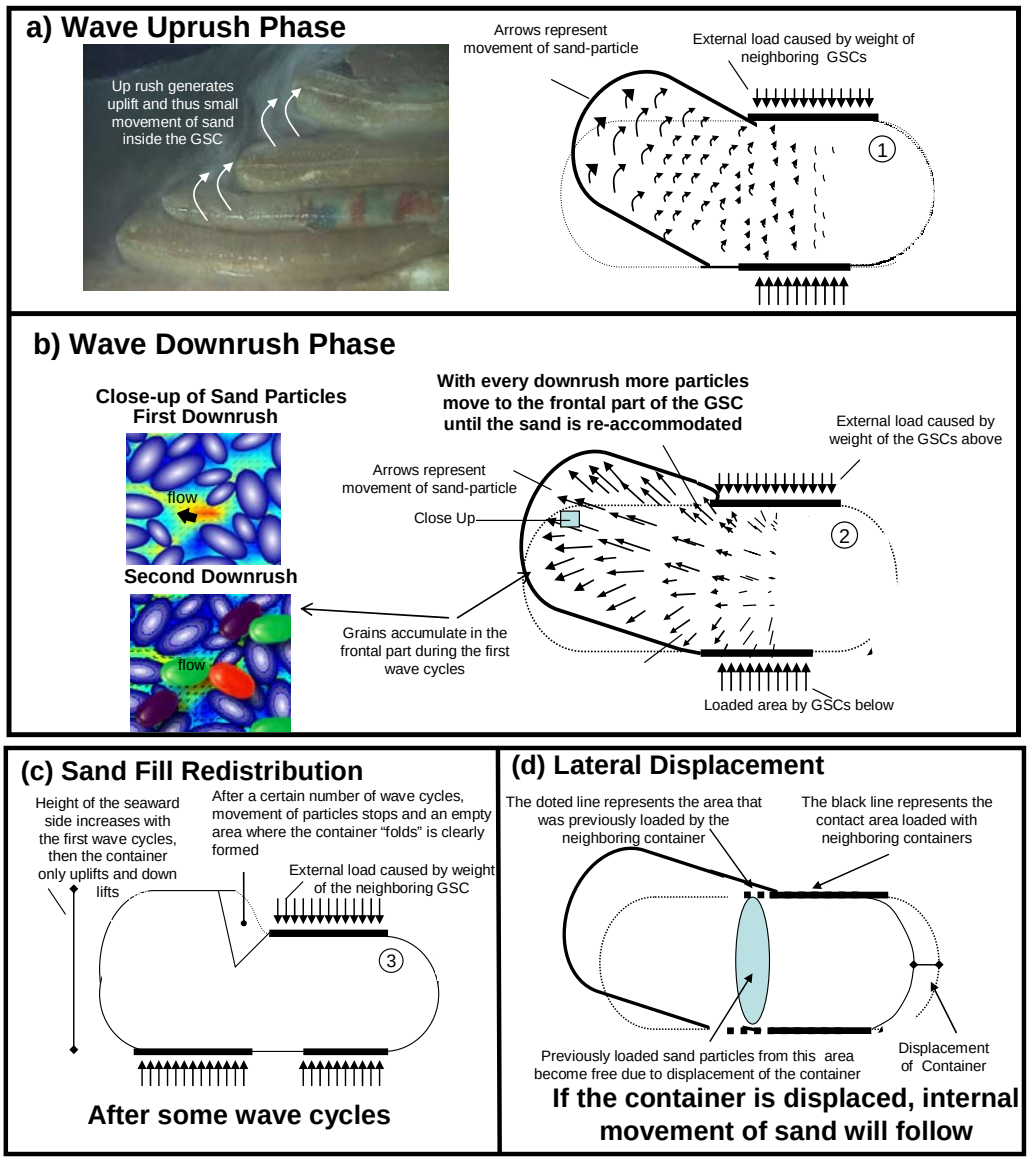

Figure 2-7: Internal Movement of Sand inside the Transparent Container

2.2.1.1 Observation from the Model tests Conducted at the Large Wave Flume at Hanover (GWK)

During the model tests at GWK, it was observed that several sand containers suffered deformation on its seaward face. These deformations are induced by the internal movement of sand in the container (Figure 2- 8).

2.2.1.2 Other Observations

Other interesting conclusions were drawn from the observations of the test at LWI with the transparent container: (i) during uprush, vortices are formed in the areas between the containers (Figure 2-9) and (ii) uprush and downrush velocities induced by higher waves acting on the containers generate high turbulence next to the revetment. This is one of the reason why measuring devices cannot give precise data

(ADV and PIV could not give values with an accuracy of more than 80%). These devices are disturbed when air bubbles appear in the measurement area.

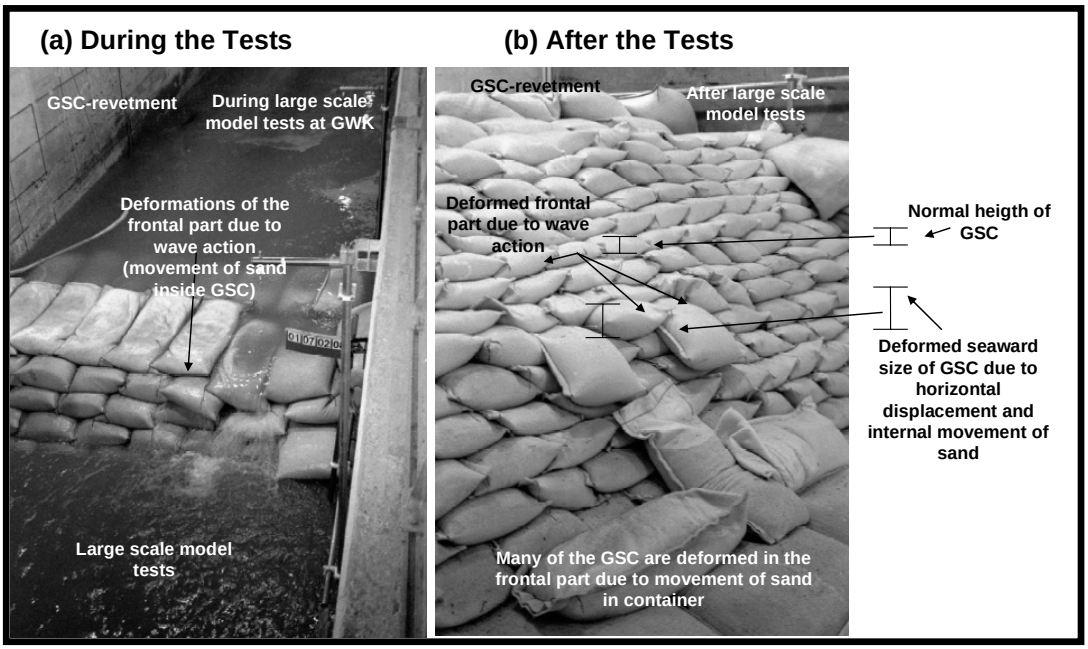

Figure 2- 9: Deformation of the Frontal part of GSC due to Internal Movement of Sand during Wave Action (Observed in GWK)

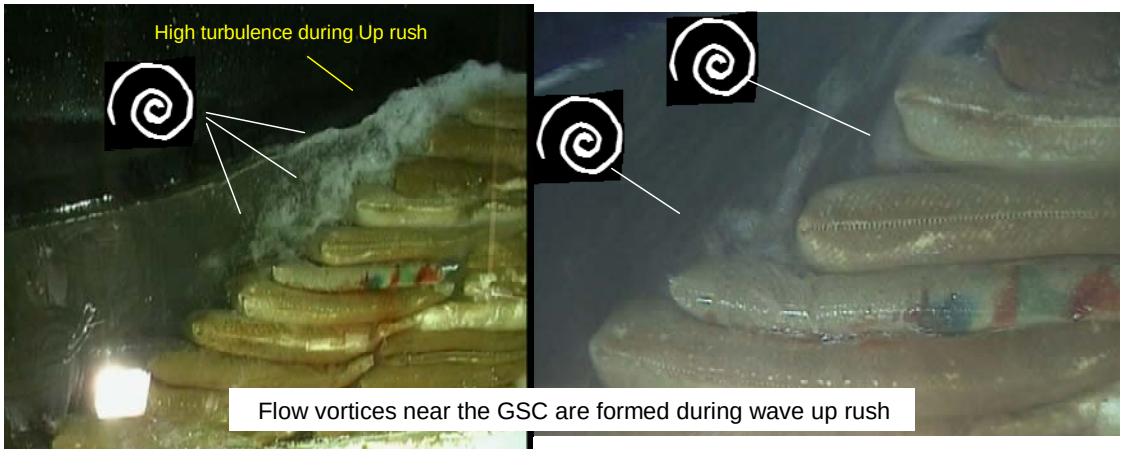

Figure 2- 10: Vortices formed next to the Containers during Uprush

It was also observed however, that a wave breaking hitting directly on the revetment could generate a larger uplift deformation of the container than non-breaking waves (Figure 2- 10).

2.2.1.3 Variation of Volume and Height of the GSC due Wave Action

Moreover, video observations of the GSC-structure were performed from the beginning of its construction until the end of the model tests to record any variations that the GSC-structure may suffer due to changing conditions.

The interesting and expected observations are that the height of the GSCs and thus, also the height of the GSC-structure is reduced due to the saturation of the sand material inside the container. In the tested GSC-structure, the height of both containers and GSC-structure was reduced approximately 4% from dry to wet

conditions (Figure 2- 11a-b). Further reduction of approximately 6% of the height occurred during wave action, leading to a total reduction of about 10% as compared with dry conditions. Thus, it was confirmed that wave action induces compaction of sand fill (Recio and Yasuhara, 2001). However, after analyzing the movement of sand inside the GSC, it was observed that the reduction of the height of the GSC (and thus the GSC-structure) is also induced by the internal movement of sand inside the GSCs to the frontal part of the containers (Figure 2- 11b).

This wave-induced variation in height of the revetment was also observed during the model tests conducted at GWK (Hinz and Oumeraci 2002, Figure 2- 12). At the large wave flume a reduction of approx 14% of the total height of the revetment was observed.

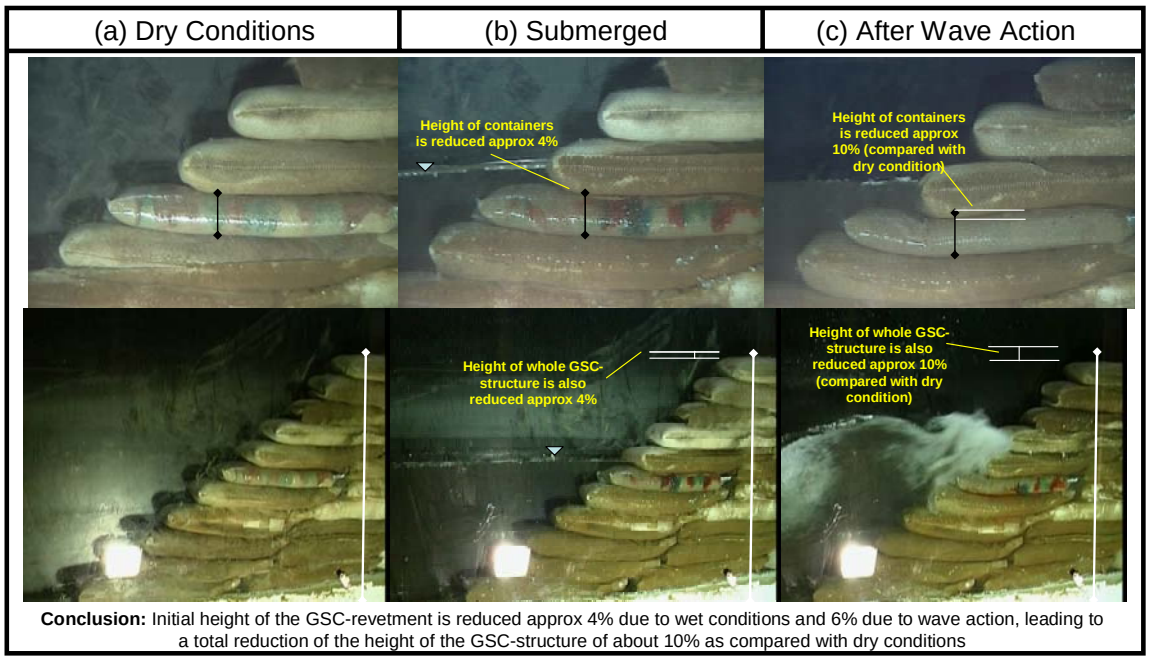

Figure 2-11: Reduction of the Height of a GSC-Structure Due to Internal Movement of Sand

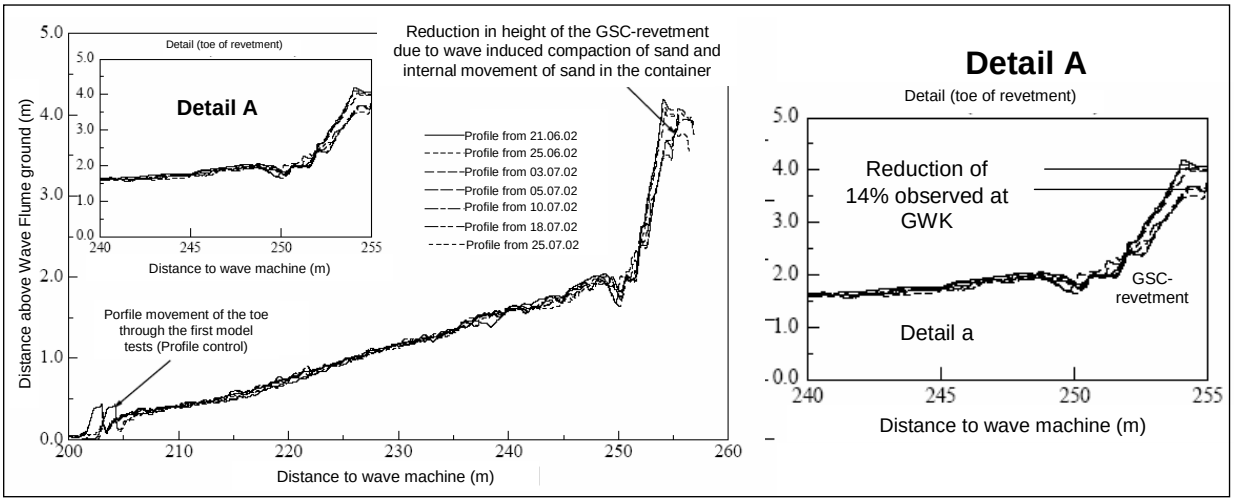

Figure 2- 12: Variations of Height of a GSC-Revetment Observed at GWK

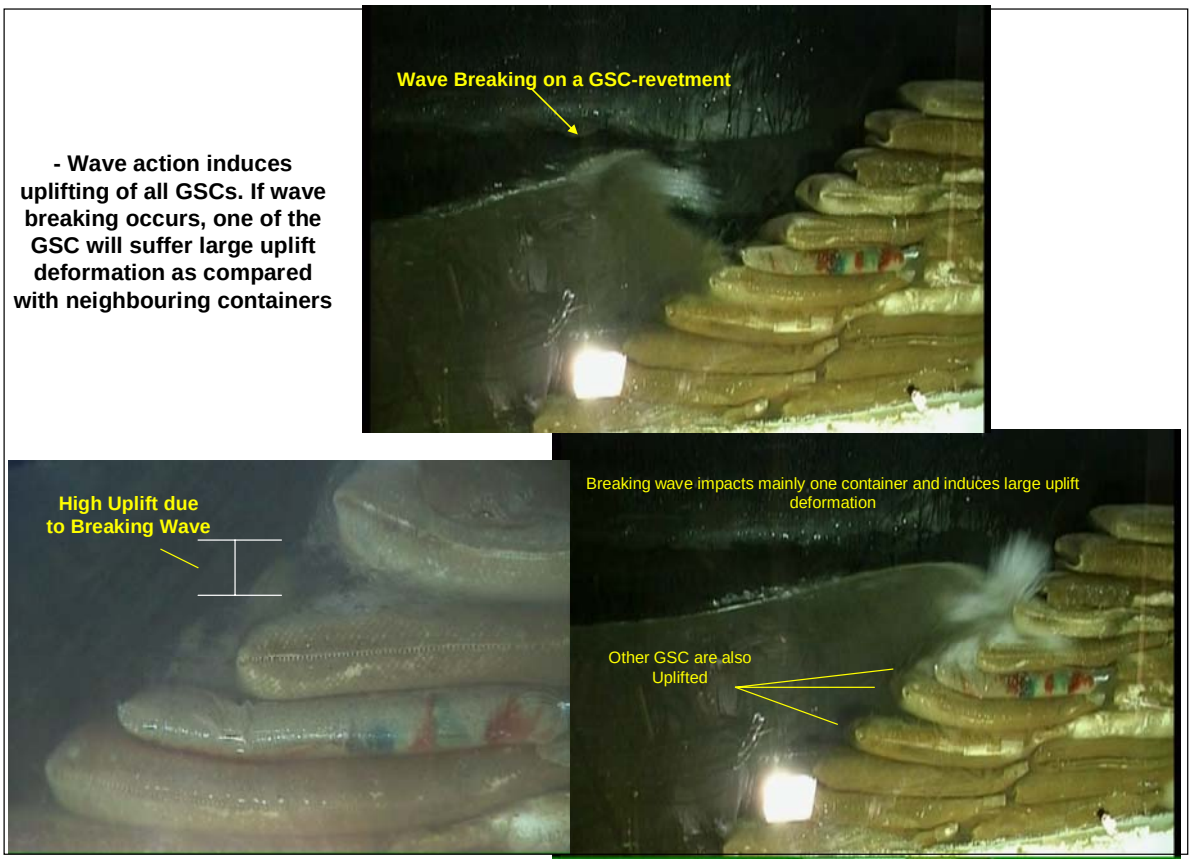

Figure 2- 13: Breaking Wave on a GSC-Revetment

2.2.1.4 Effect of Sand Movement in the GSC on the Stability of the Revetment

The most important objective of these model tests was to investigate the effect of sand movement inside the container on the stability of GSC-revetments.
To explain the influence of the internal movement of sand on the stability, the classic drag and lift equation are recalled:

$$F_D = 0.5\rho_w u^2 C_D A_s \qquad (2.1)$$

$$F_L = 0.5\rho_w u^2 C_L A_T \qquad (2.2)$$

where F_D is the drag force, ρ_w the density of water, C_D , C_L are empirical force coefficients which depends of the form of the element, u the horizontal velocity, and A_s and A_T are the areas normal and in the direction of the flow, respectively

The drag force is a function of the transversal area of the structure. During uprush and downrush the wave-induced velocities will act on the uplifted part of the container. Due to the movement of sand, this transversal area will be increased, therefore the larger the uplifted area, the higher the drag force (Figure 2- 14).
Considering that with every displacement of the container, movement of sand inside the container will follows, then, with every movement of sand, the forces acting on the container will be larger. Therefore, it can be concluded that the movement of sand strongly influences the hydraulic stability of GSC-structures.

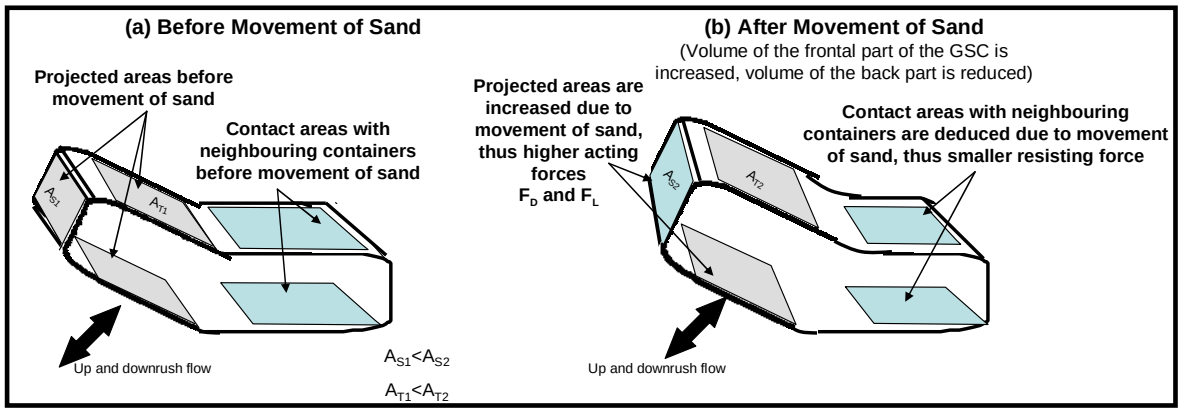

Figure 2- 14: Influence of the Internal Movement of Sand on the Stability of the Container

To clarify the influence of the sand movement on the stability, the approach by Wouters (1998) is considered. Wouters considered the stability of a revetments as a comparison between acting moments and resisting moments (Figure 2- 15). From this figure it is clearly seen that the mobilizing forces are the lift, drag and inertia forces while the resisting force is only the weight of the container.
Before sand movement, the centre of gravity of the container is at the middle part of the container (Figure 2-15a). However after sand movement, the centre of gravity of the container is moved to the left, thus, the resisting moment is reduced (Figure 2-15b).
Therefore it can be concluded that the internal sand movement in a GSC affects the stability of the container.

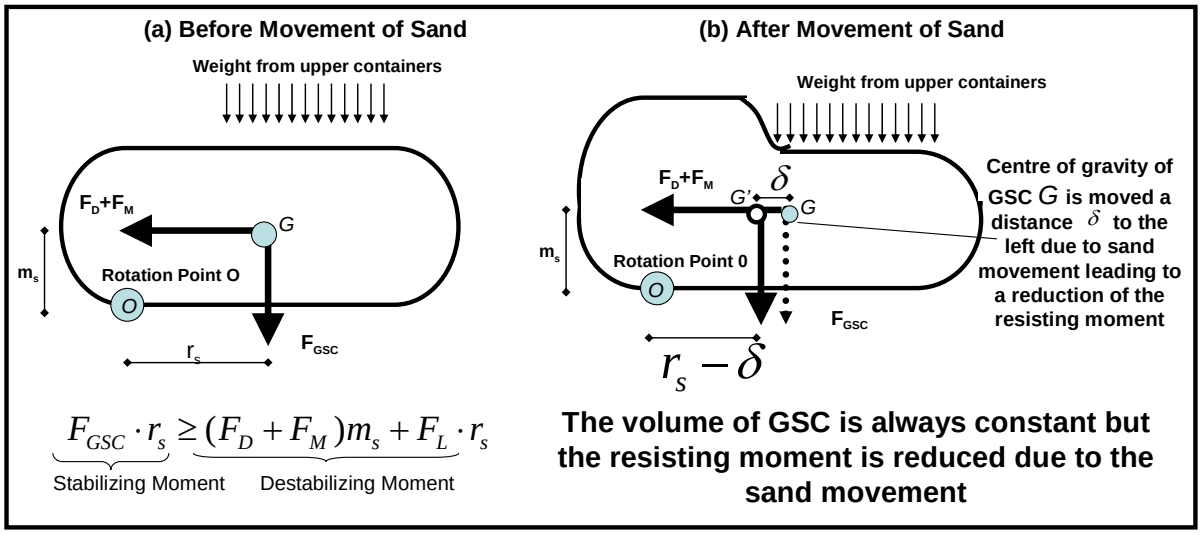

Figure 2- 15: Influence of the Sand Movement of the Stability of GSC

2.2.2 Variation of the Contact Areas During Wave Action

In addition, the video recordings were analyzed to quantify the variation of the contact areas between neighbouring containers during wave action.

2.2.2.1 Observation of Contact Areas During Wave Action

During the model tests, the variation of the contact areas among neighbouring containers during wave action was observed. It was seen that the contact areas are reduced due to the uplift deformation that the containers suffer on their frontal part (seaward). Recalling that the resisting force of the GSC is the weight projected on the contact area, thus, a reduction on these contact areas reduces the stability of the revetment (Figure 2- 16).

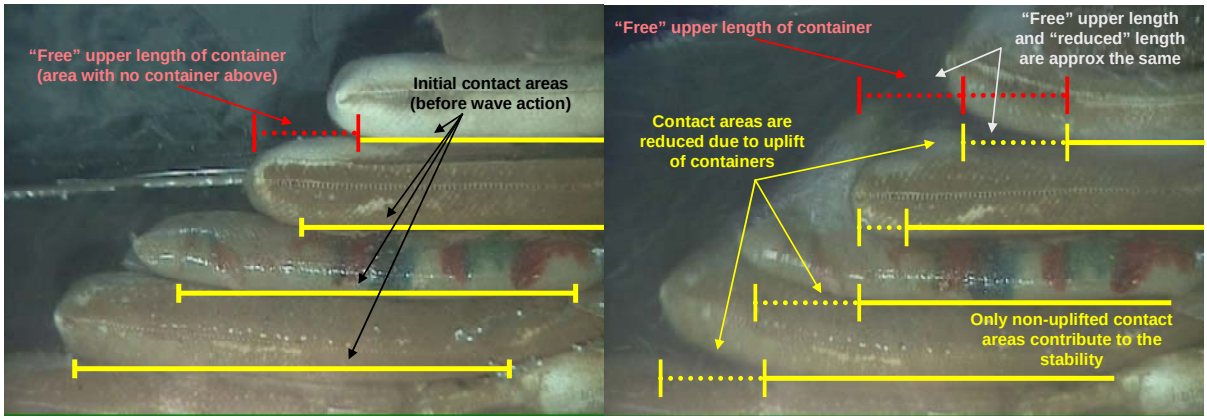

Figure 2- 16: Variation of the Contact Areas between Neighbouring Containers

2.2.2.2 Variations of the Contact Areas between GSCs During Wave Action

The "effective" length of the containers was quantified during the model test. The upper length of a container is reduced around twice the "free" upper lengths of the container. "Free" length means the length of a container that is not subject to any load from upper containers. "Effective" length means the length of the GSC that is never uplifted and actually resists the displacement of the container (Figure 2- 17).
To obtain the "effective" resisting length of the container:

(i) Draw a line following the slope of the revetment.
(ii) Measure the "free" upper length of a container.
(iii) Draw a horizontal line from the slope line to a distance equal to twice the "free" upper length.
(iv) Draw a line parallel to the slope which is separated two times the distance of the "free" upper length of a container as shown in Figure 2-17.
(v) The "effective" resisting length of the containers is the length from the point of line (4) to the landward-end of the container (Figure 2-17).

This clearly illustrates that there is a relation between the uplift deformation of the containers and the slope angle of the structure. The steepness of the structure is strongly related to the uplift deformation that the containers will suffer.

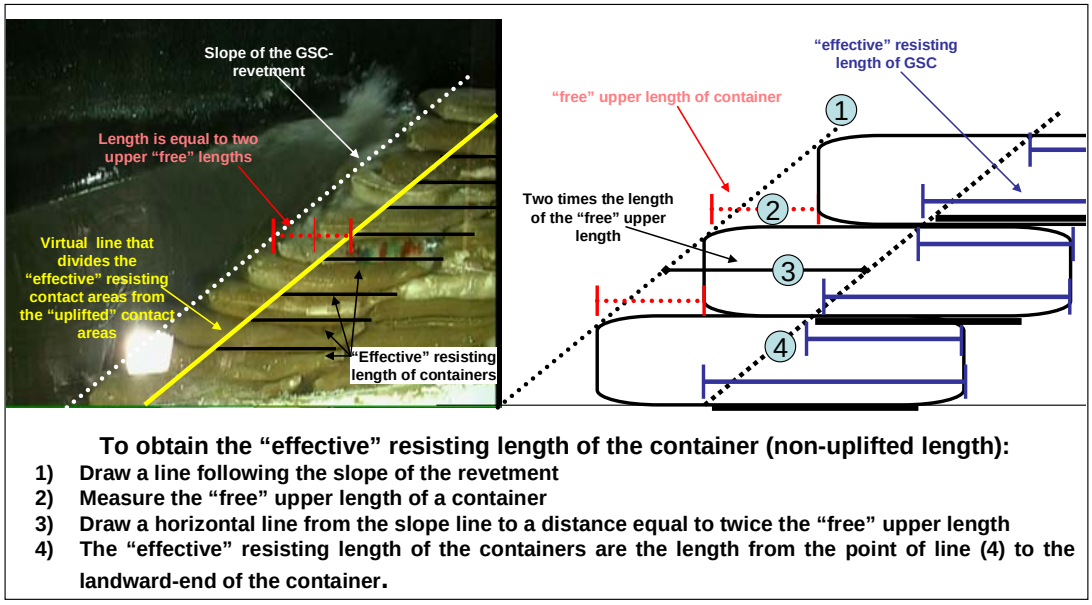

To obtain the "effective" resisting length of the container (non-uplifted length):

1) **Draw a line following the slope of the revetment**
2) **Measure the "free" upper length of a container**
3) **Draw a horizontal line from the slope line to a distance equal to twice the "free" upper length**
4) **The "effective" resisting length of the containers are the length from the point of line (4) to the landward-end of the container.**

Figure 2- 17: Resisting Contact Areas of GSC

2.3. Conclusions

The conclusions derived from this Chapter can be summarized as follows:

- The movement of sand inside the container during wave action strongly influence the stability of GSC-revetments.
- The movement of sand mainly occurs during the first waves and then after every incremental horizontal displacement of the container.
- The main direction of the movement of sand inside the container is seaward. Accumulation of sand in the face of the container is induced due to the movement of sand.
- An increase in the frontal volume of the container due to the internal movement of sand reduces the stability of the GSC-structure.
- The wave-induced forces compact the sand and induced a reduction of the total height of the revetment of approx 10%. This reduction in height is very important for GSC-revetments where the final height of the structure is important.
- The resisting contact areas of GSC are reduced due to the uplift deformation of the containers.
- Due to the uplift deformation of the containers, the "effective" resisting contact length of the containers can be calculated subtracting two lengths of the "free" upper length of the container (Figures 2- 6 and 2-17).

2.4 Acknowledgments

- The financial support of the first author by DAAD (Deutsche Akademischer Austausch Dienst) is deeply appreciated
- The model tests were supported by the Leichtweiss Institute (Hydromechanics and Coastal Engineering Department)
- NAUE GmbH & Co. KG provided the goetextiles and technical support.

Their help to this project is deeply appreciated.

2.5 **References**

Hinz M. and Oumeraci H. “Versuchtagebuch, Geotextile Sandcontainer Dünenbarriere” Internal Report, LWI, 2001, Germany (in German)

Matsuoka H. and Liu S. “New earth reinforcement method by soilbags”, Soils and Foundations, Vol 43, No. 6, Dec 2003, Japanese Geotechnical Society

Oumeraci, H.; Bleck, M.; Hinz, M.; Möller, J. 2002 Theoretische Untersuchungen geotextiler Sancontainer im Küstenschutz. Bericht des Leichtweiß-Instituts Nr. 866, Braunschweig (in German)

Hinz, M.and Oumeraci H.2002: Großmaßstäbiliche Untersuchungen zur hydraulischen Stabilität geotextiler Sancontainer unter Wellenbelastung. Bericht des Leichtweiß-Instituts Nr. 878, Braunschweig. (in German)

Recio J.; Yasuhara K. 2001. Model Test on Geosynthetic Reinforced Sand Revetment Subjected to Assailing Waves, Geosynthetic Engineering Journal, December, pag. 239-245.

Roberson, John and Crowe, Clayton, 1990 Engineering Fluid Mechanics. Houghton Mifflin Company, Boston, MA.

Chapter 3

Wave-Induced Forces on a Structure made of Geotextile Sand Containers (GSC)

Model Tests Using a Container Instrumented with Pressure Gauges

Introduction

In this Chapter, the analysis results and analyses obtained by performing model tests of a GSC-structure under wave action are presented. During the model tests two of the containers are instrumented with pressure gauges to record the wave-induced pressures on its surface. Therefore, this Chapter is divided in the following sections: (i) the experimental set up, (ii) the analysis and results of the laboratory investigations and (iii) finally, some concluding remarks.

3.1. Model Tests Using a Container Instrumented with Pressure Gauges Placed in a GSC-Structure

3.1.1. Experimental Set-Up

The model tests have been performed in the wave-flume of the Leichtweiss Institute. At one end regular and irregular waves were generated. At the other end a structure made with a geotextile sand container was build. Two of the GSCs in the structure are instrumented with pressure gauges to record the wave-induced pressures on its perimeter.

In addition, surface elevations were recorded in front of the structure and along the flume using common resistance type wave gauges (Figure 3-1). The gauges in front of the structure were combined with pressure gauges and AVD-proves (velocimeters) to measure the energy components simultaneously.

The instrumented container was placed at three different elevations in the structure to investigate the influence of the location of the GSC with respect of the sill water level on the wave-induced pressure. Then, by integrating the pressures around the containers, the total wave-induced forces and moments were derived.

The **objectives of the model tests** can be summarized as follows:

(i) Derivation and quantification of the wave-induced pressures geotextile sand containers (GSC).
(ii) Derivation of pertinent data for the validation of numerical models.
(iii) Further understanding of the processes associated with the stability of structures made of geotextile sand containers.

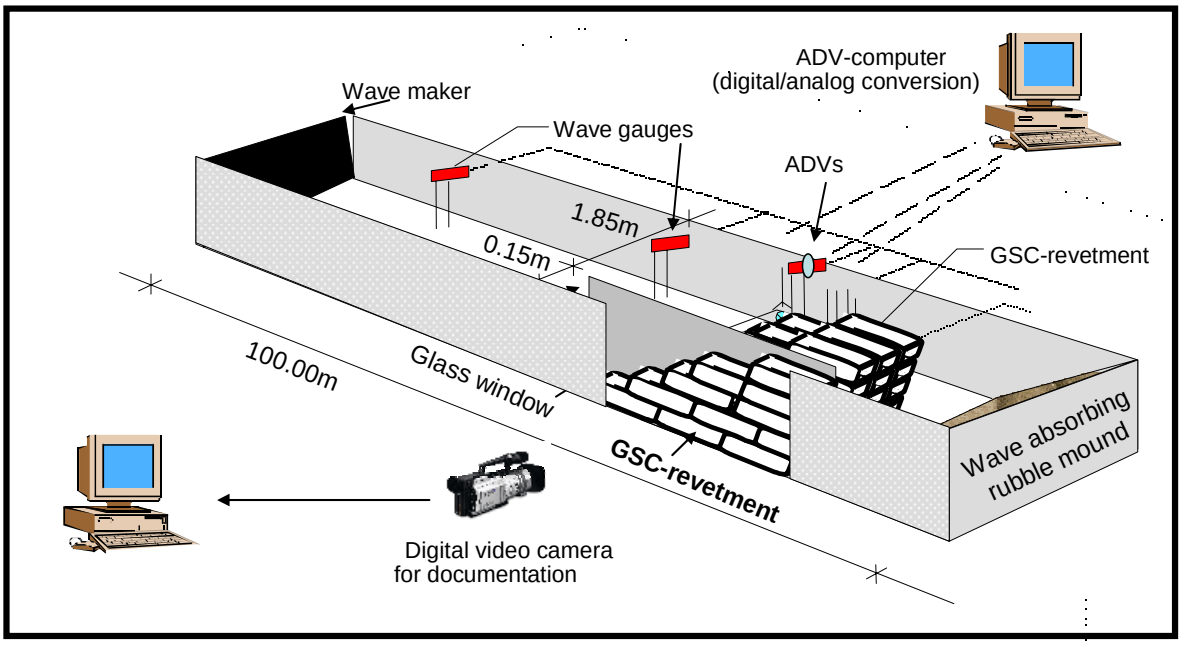

(a) Overview of the Wave-flume

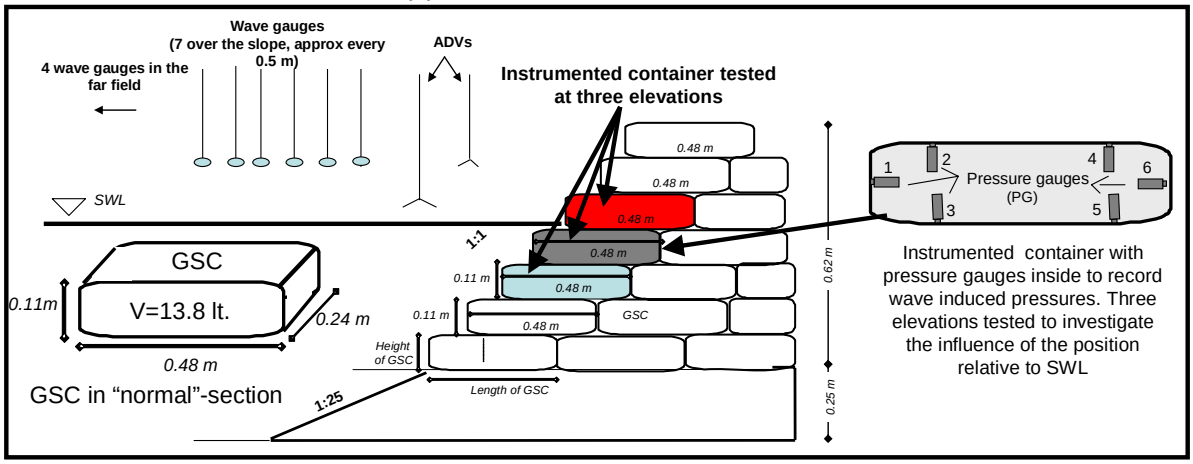

(b) Cross Section of the Model Tests

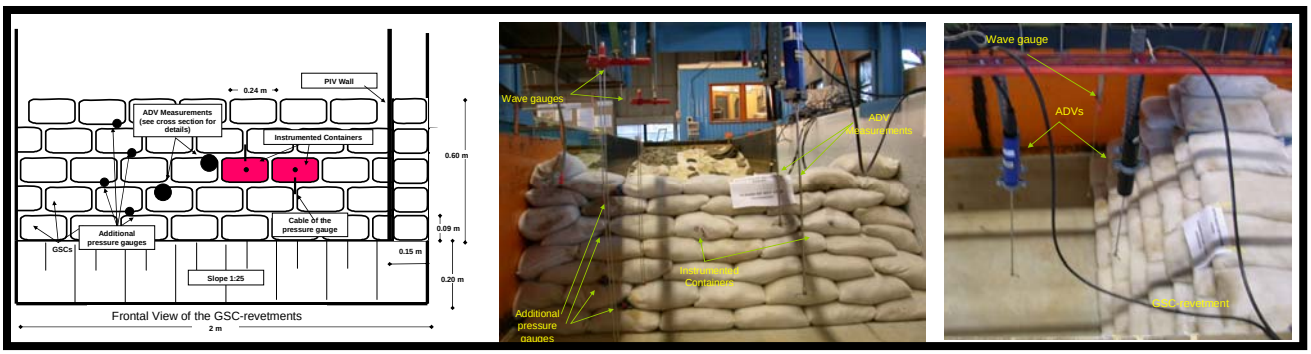

(c) Frontal View of the GSC-Revetment

Figure 3-1: Experimental Set-Up

3.1.2 Measuring Techniques

Local measurements at and near the GSC during the model tests consisted in wave gauges, pressure gauges inside the instrumented container, ADVs (Acoustic Doppler Velocimeters) and video records of the GSC-structure (Figure 3-2).

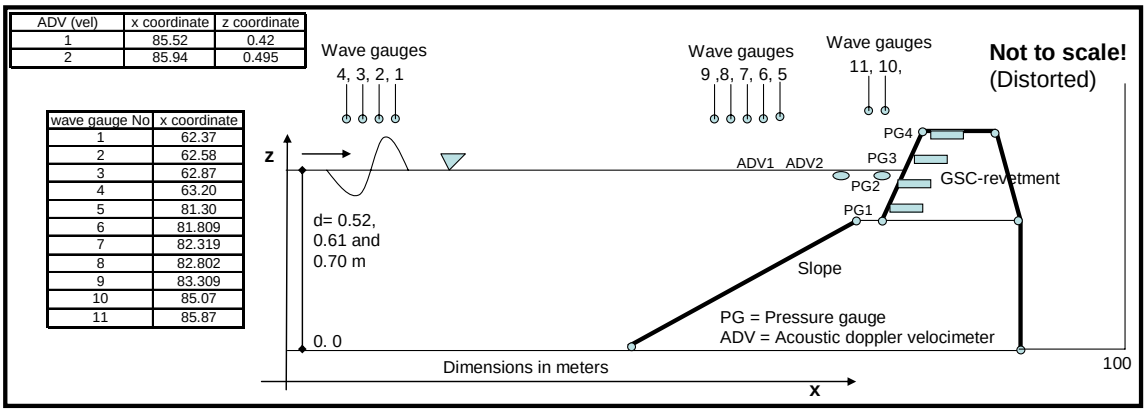

Figure 3-2: Location of the Measurement Devices

Instrumented GSC

The size of an instrumented container is shown in Figure 3-3. Two instrumented containers were used: one with pressure gauges measuring pressure on the top side of the container and the other container measuring the pressures on the bottom part of the container. Due to size limitations and scale effects only three pressure gauges per container were implemented. Additional pressure gauges on the front of the structure were also used to verify the recorded pressures.

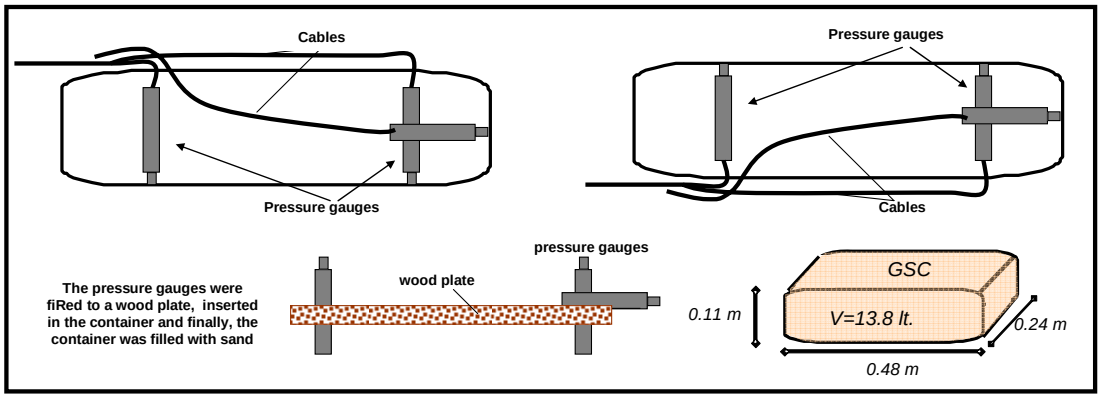

Figure 3-3: Instrumented Containers and Location of the Pressure Gauges inside the GSCs

Other Measurements

Two ADVs were used to obtain the velocities before the GSC-structure (refer to Figure 3-1). The ADVs record velocities up to 100 cm/s in three directions.

Additional pressure gauge were installed in the slope of the revetment in order to record wave induced pressures on the complete revetment (Figure 3-2)

During the model tests **video records** were perform by using available video cameras.

3.1.3 Stages of the Model Tests

The model tests were divided in three stages. Each stage had the instrumented container in different position to investigate the influence of the location of the GSC with respect of the still water level on the wave-induced pressures.

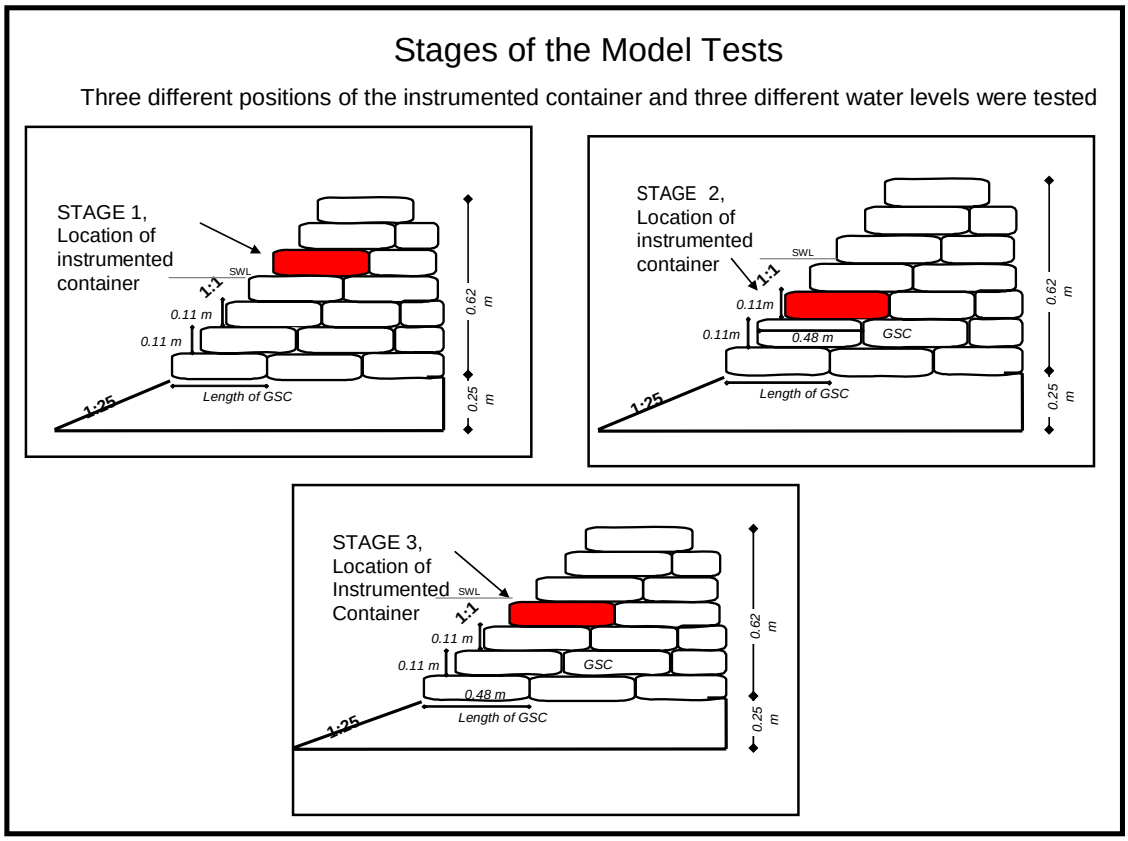

Figure 3-4: Stages of the Model Tests (instrumented container in three different positions)

3.1.4 Model Wave Conditions

Table 3.1 shows the wave conditions used in the model tests. More than 100 different model tests were performed. The wave conditions were selected based on the following criteria:

(i) Model test should be performed to obtained reliable data for the numerical simulations involving several wave conditions and water levels.

(ii) Pressures induced by breaking waves on GSCs should be investigated.

(iii) Enough tests should be performed to quantify the influence of the wave parameters on the wave-induced forces on the containers.

3.2 Selected Model Test Results and Analysis

3.2.1 Integration of Pressures on the Instrumented GSC

The main advantage of instrumenting a container with pressure gauges is that the pressure on the whole surface of the container can be derived at every time step of the wave cycle. Pressure on the GSC is interpolated from the values recorded by the pressure gauges.

The pressures were integrated by applying a simple MatLab routine (refer to Burg 2006 for details on the routine)

The program reads the data obtained from the pressure gauges inside the container and interpolates the values between them (based on the coordinates of the pressure gauges). From this integration the program calculates the resultant force and resultant moments in two and three dimensions (2D and 3D). 2-D dimensions consider the container as an element of infinite length in the transversal axis of the flow. The results can be used to clarify the wave-induced pressure at every time step

of the wave phases. Figure 5 shows one example of wave-induced pressures and forces on an instrumented container.

Table 3.1. Wave Conditions Used in All stages

		Wave Period (seconds)						
Depth (meter)	**Wave Height (meter)**	**1.50**	**2.00**	**2.50**	**3.00**	**3.50**	**4.00**	**4.5**
0.700	**0.08**		**R**	**R**	**R**	**R**	**R**	**R**
	0.12		**R**	**R**	**R/S**			
	0.16	**R**	**R**	**R**				
	0.20	**R**	**R/S**					
0.610	**0.08**		**R**	**R**	**R**	**R**	**R**	**R**
	0.12		**R**	**R**	**R/S**			
	0.16	**R**	**R**	**R**				
	0.20	**R**	**R/S**					
0.520	**0.08**		**R**	**R**	**R**	**R**	**R**	**R**
	0.12		**R**	**R**	**R/S**			
	0.16	**R**	**R**	**R**				
	0.20	**R**	**R/S**					
Experiments with Regular Waves and JONSPAW Spectra.								
Every model test consists in 200 waves.								

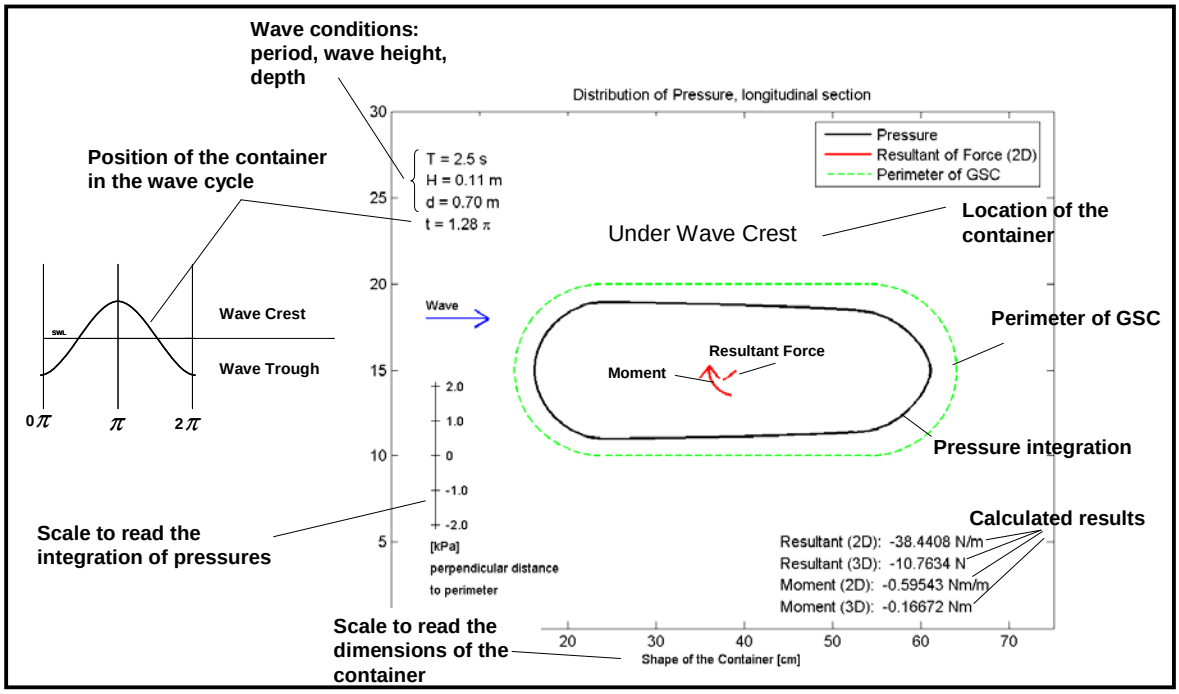

Figure 3-5: Explanation of the Calculated Results Obtained from Integration of Pressures around the Container

3.2.2 Influence of the Position of the Container in the Revetment on the Wave-induced Forces

As it is seen from Figure 3-4, the instrumented container was tested at three different positions to investigate the influence of the position of the container in relation to the still water level on the wave-induced forces.

3.2.2.1 Container Placed Far Below the Still Water Level (SWL)

Firstly, the container that is always submerged even during wave trough was investigated. Independent of the wave conditions the wave-induced pressures and forces on the containers follow the same pattern. Only the magnitude of the pressure/forces, deepens on the boundary conditions.

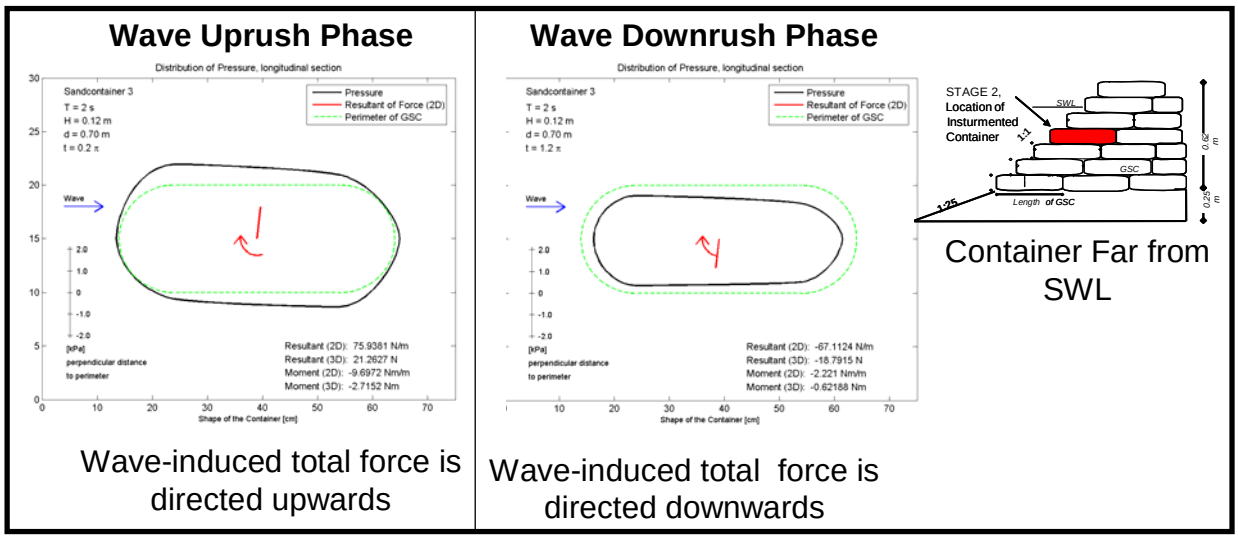

Figure 3-6: Wave-induced Pressures and Forces on a Submerged Container (always under the water level)

Wave Uprush Phase: the total force is directed mainly upward (Figure 3-6).

Wave Downrush Phase: during the wave downrush phase, the total force is mainly directed downwards, with a small horizontal component (Figure 3-6)

The wave-induced flow through the gaps between the containers does not affect the wave induced pressures on the containers that are far below the SWL. These wave-induced pressures are very similar to the ones recorded form a container laid directly of the sea bed (Chapter 4 of this report). It could be stated that submerged containers in the revetment far from the SWL behave almost independently of the wave-induced flow inside the revetment and are only affected by the wave conditions (i. e. permeability of the structure do not affect the wave-induced pressures on this container).

3.2.2.2 Container Placed Just Below the Still Water Level (SWL)

The instrumented container just below the SWL recorded the most “complex” wave-induced forces. This container behaves very different than its neighbouring containers.

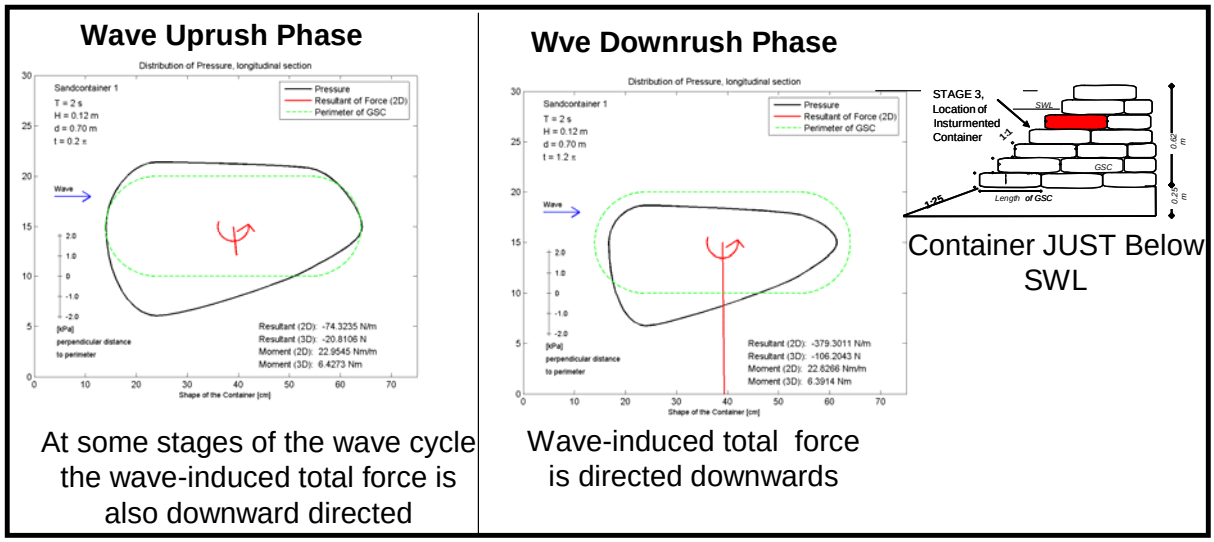

Figure 3-7: Wave-induced Pressures and Forces on a Container that is JUST below the SWL (see next figures for more details)

Wave Uprush Phase: during downrush, the container is compressed due to the wave crest. The is a pressure "build-up" inside the structure that generates large wave-induced forces on the container (Figure 3-7)

Wave Downrush Phase: the pressure build-up in the container generates a seaward induced force on the container that could be critical for the stability of the structure.

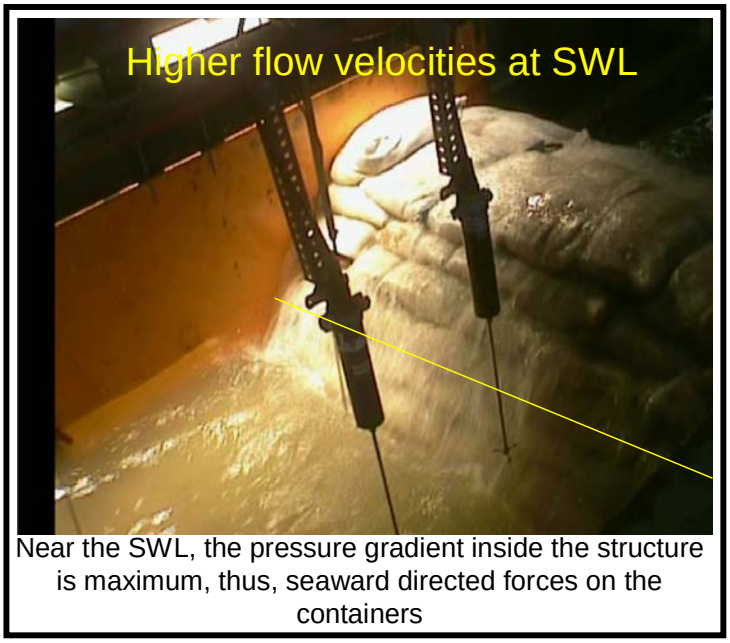

Figure 3-8: Pressures inside the Container Generate a Seaward Oriented Force on the Containers

Videos from the model tests were also investigated to clarify the wave-induced pressures in the structure. It was found that the critical area for the stability of the GSC-structure is just below SWL. This is due to the fact that wave up and downrush velocities in front and inside the GSC-structure are different, thus, inducing a "build-

up" of the hydraulic gradient inside the structure which has a maximum value at the beginning of downrush at the area just below SWL (Figure 3-9).

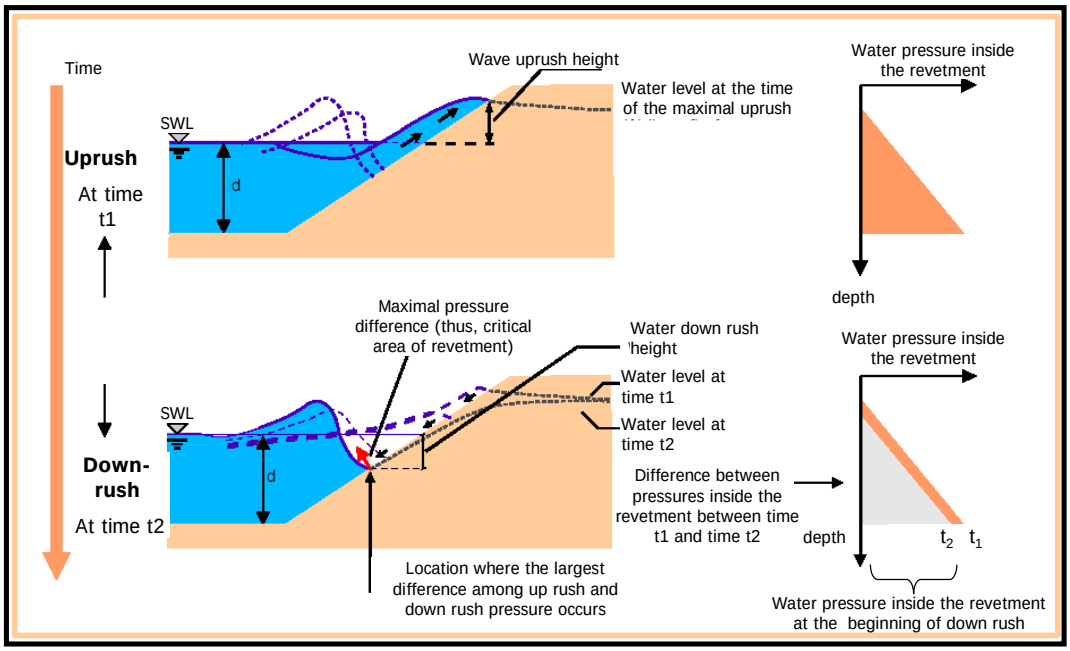

Figure 3-9: Wave-Induced Pressures in Front and inside a GSC-Structure

3.2.2.3 Container Placed Above the Still Water Level (SWL)

This container was only submerged during a part of the wave uprush. The wave-induced pressures on this containers showed similar pressures than the submerged containers (far below SWL) but with some particularities.

Wave Uprush Phase: during uprush, the total force on the containers is directed upward.

Wave Downrush Phase: as the submerged containers, the container above SWL suffered negative pressures. However, these pressures were much smaller than the submerged containers. This can be explained considering that the difference between pressures (Up and downrush) in not as big as in the submerged containers (figure 3-10).

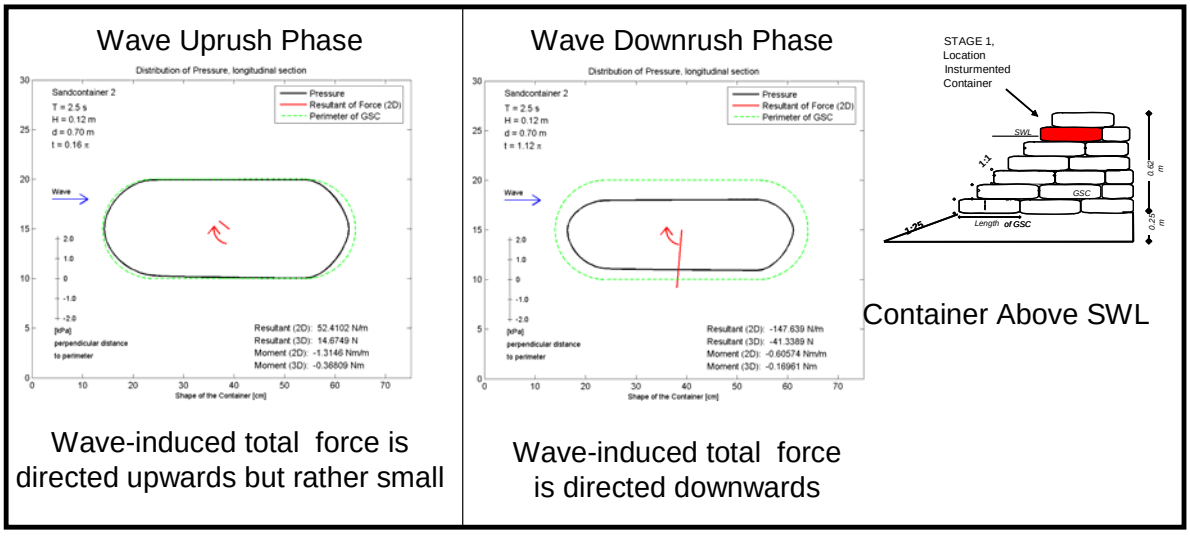

Figure 3-10: Wave-Induced Pressures and Forces on a Container that ABOVE the SWL

3.3.2.3. Interaction between Wave-Induced Forces

One of the objectives of placing the instrumented container in three positions is to investigate the interaction between the wave-induced forces on the containers during wave action. Therefore, containers with same wave conditions but different position were simultaneously analyzed (Figures 3-11 to 3-13 and Burg 2006).

The results obtained from the three different positions of the container in the GSC-structure are illustrated in Figure 3-11. It can be seen that the critical container for the stability of the structure is the container placed just below the still water level, while the least critical is the container placed far below the still water level since this container is not influence by the pressure gradient generated inside the structure.
It is also noticed that the lift force (upwards directed force) is influenced by the wave period.

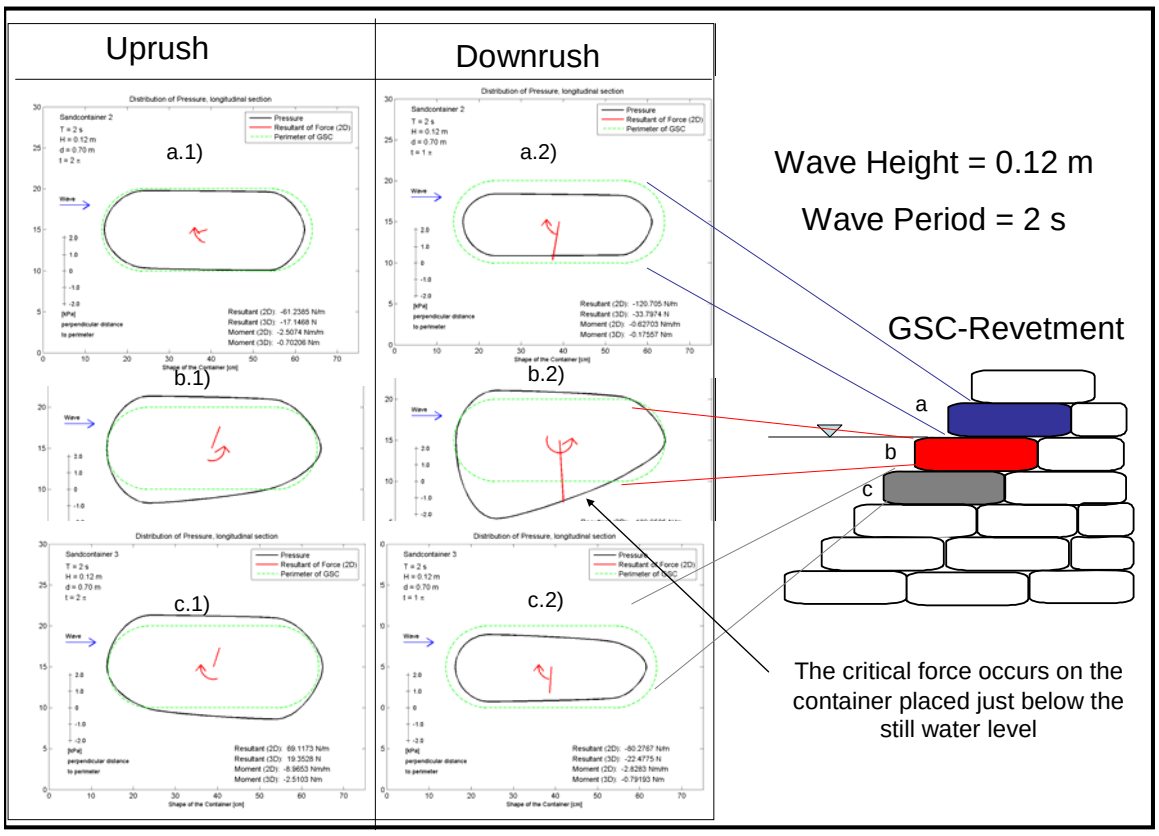

Figure 3-11: Interaction between Wave-Induced Forces on GSC (critical container placed just below the still water level)

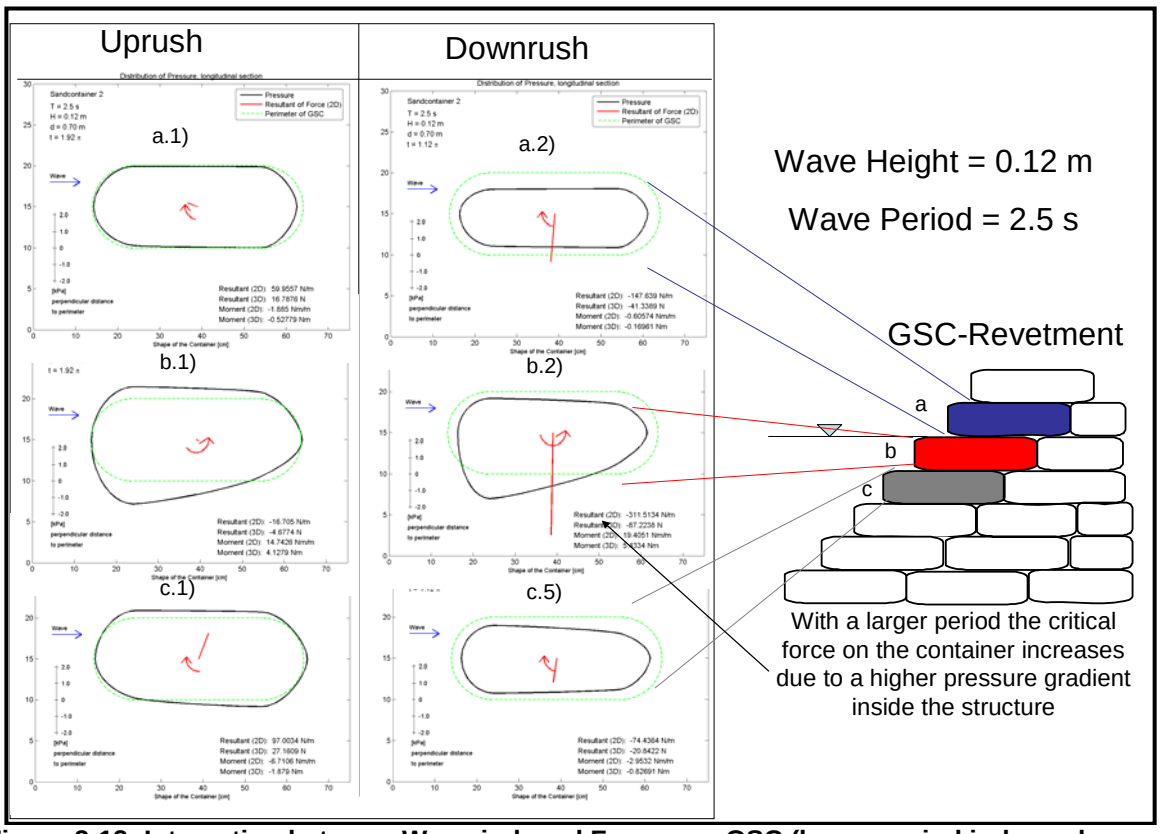

Figure 3-12: Interaction between Wave-induced Forces on GSC (larger period induces larger force on critical container)

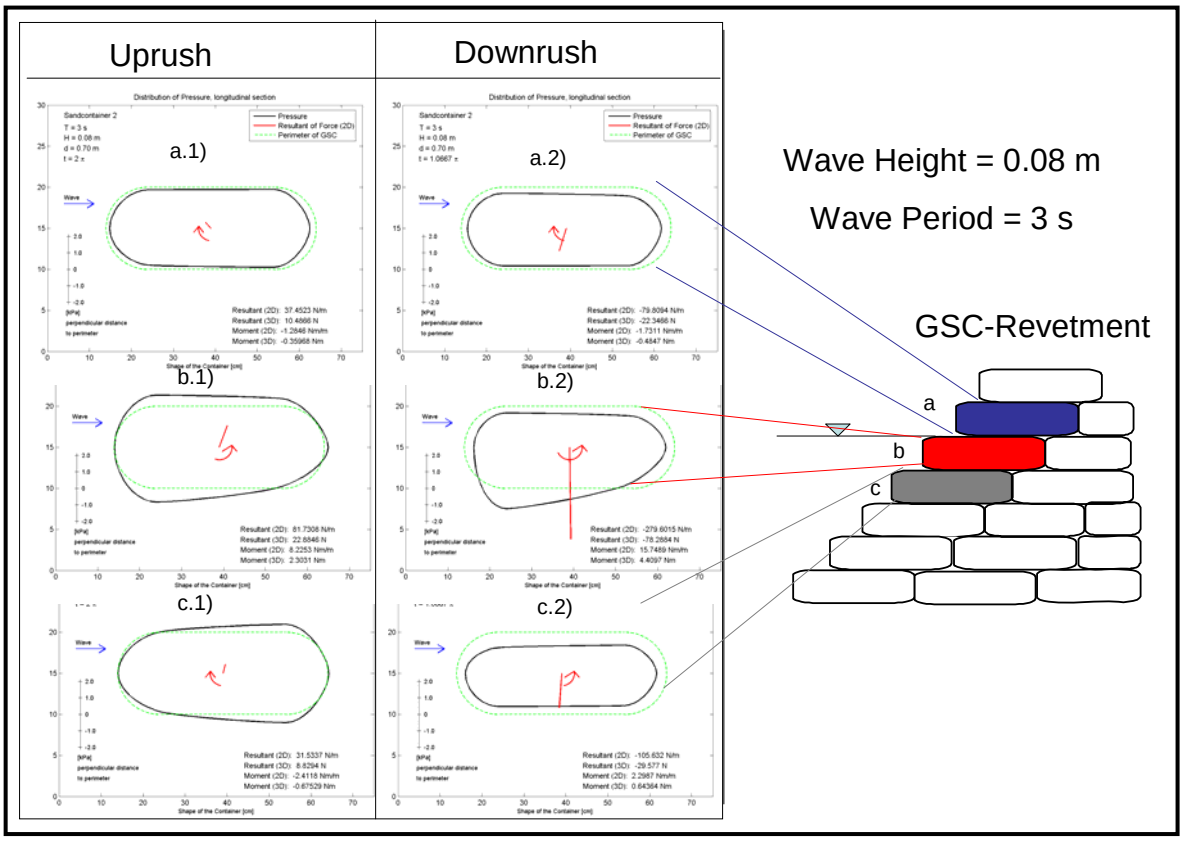

Figure 3-13: Interaction between Wave-Induced Forces on GSC

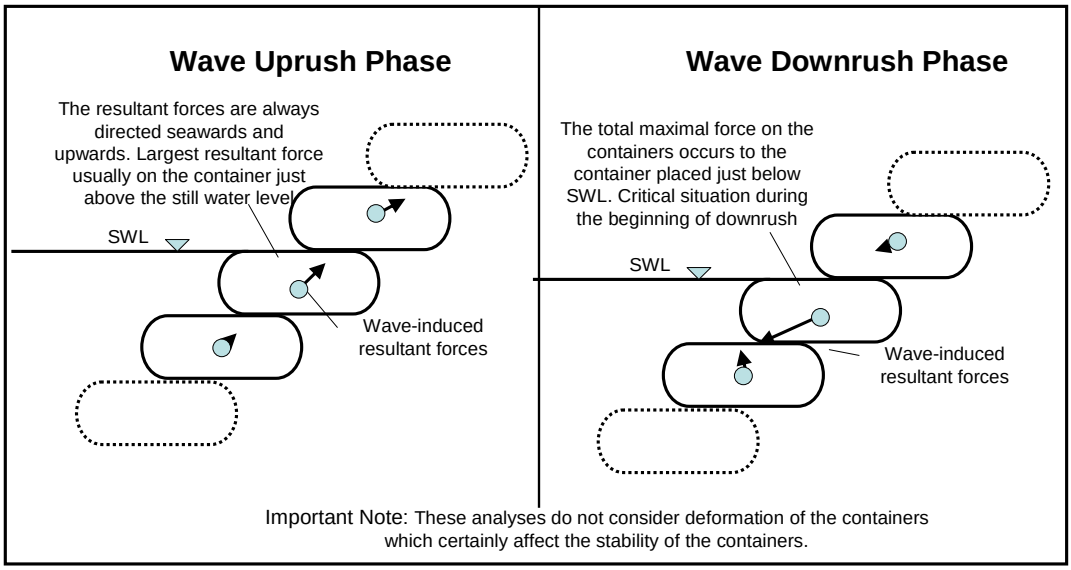

Figure 3-14: Resultant Forces on GSC During Wave Action (definition sketch)

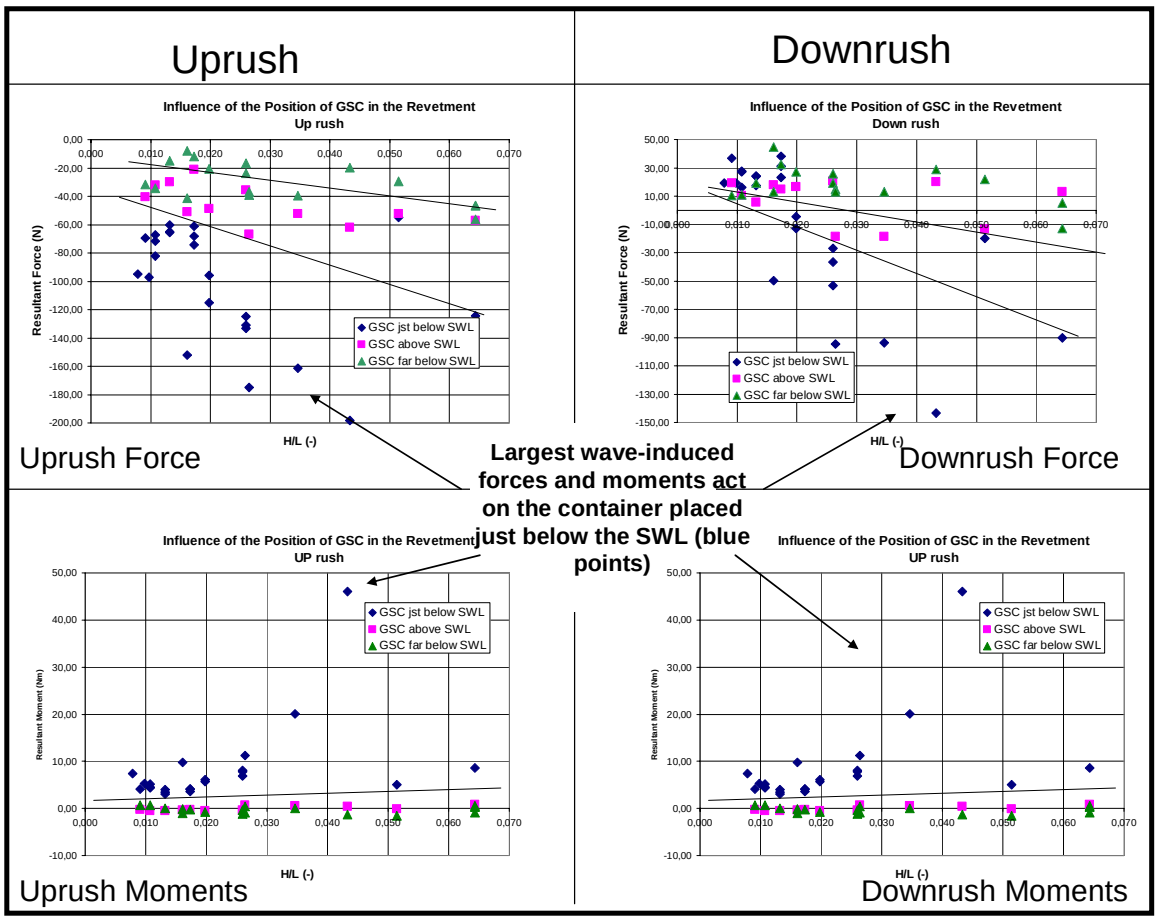

Figure 3-15: Resultant Forces and Moments acting on the three Analyzed Containers (container placed just below SWL has the largest wave-induced forces)

The wave-induced forces on the containers strongly depend of its position in the structure in relation to the still water level. This clearly shows that the permeability of the structure also influences its overall stability

In addition, using the data obtained from the model tests it was proved that the containers placed just below the SWL have the highest wave-induced forces and the highest wave-induced moments. The sign in the force graphs indicates the direction of the resultant (+ upwards, - downwards), while negative moments are clockwise directed (Figure 3-15)

3.2.4. Breaking Wave Loading on GSC-Structure

The hydraulic processes on a coastal structure are different when subject to breaking waves or non-breaking waves. Therefore, an investigation on the wave-induced forces by breaking waves on a GSC-structure was performed (Figure 3-16).

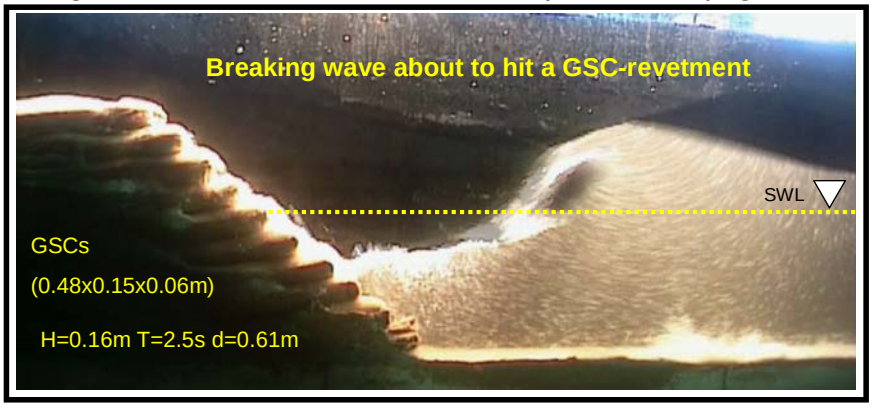

Figure 3-16: Breaking Wave on a GSC-Structure in the LWI-Flume

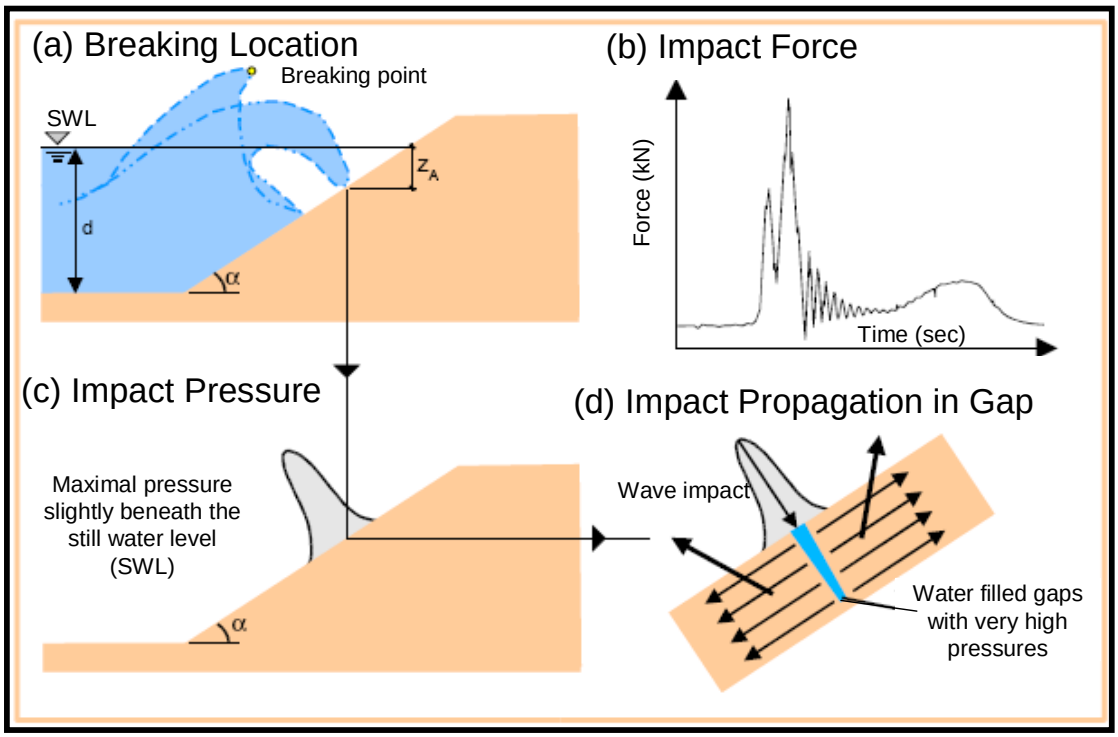

Figure 3-17: Breaking Wave Load on Dike Slope (definition sketches, modified from Hinz and Oumeraci, 2002)

Breaking waves induce the most destructive loads affecting coastal structures. In the case of structures with gaps (like in a GSC-structure) the combination of horizontal and uplift forces which are generated inside the horizontal gaps, might cause the collapse of a coastal structure.
High pressures at the entrance of the gap usually lead to high pressures inside the gap. The pressure propagation inside the gap will determine, how critical the total pressures on the constitutive elements of the structure are (Marth 2005).

However, there is no information available about the stability of GSC-structures subject to breaking waves and about the pressure propagation within the gaps between sand containers. Therefore, a detailed analysis of the wave-induced pressures inside the gaps between the containers was performed.

Führböter (1991) showed that a breaking wave induces a maximum pressure slightly beneath the still water level (SWL) (Figure 3-18a). The resulting impact force is characterized by a very high peak and a short duration (Figure 3-18b). The impact pressures propagate through the gaps into the structure, where they are redistributed and possibly amplified or damped, depending on the boundary conditions within the gap (Marth, 2005) (Figure 3-18d).

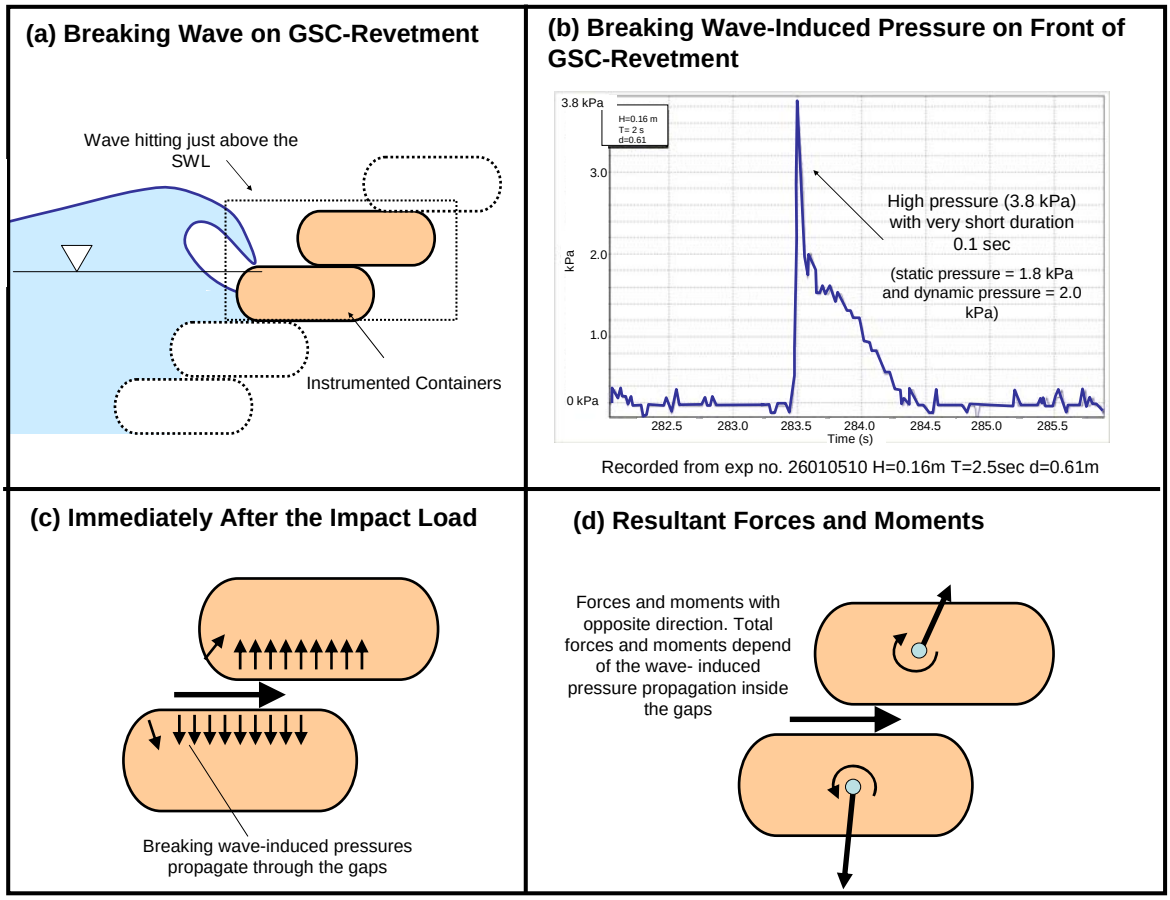

Figure 3-18: Breaking Wave Impact Loads on a GSC-Structure (definition sketch)

The same phenomenon, as qualitatively illustrated in Figure 3-18, was also recorded by the pressure gauges in the gaps between geotextile sand containers. The precise

time, when the breaking wave hits the structure, was recorded (Figure 3-19b). When a breaking wave hits the area just above the SWL, the instrumented container located in the impact zone, recorded higher pressures on its front. At the impact time the resulting forces will cause a separation of the two containers (Figure 3-19c). The upper container moves upwards and rotates in clockwise direction (Figure 3-19d), while the container below the impact point moves downward and rotate in opposite direction. In order to decide, whether this breaking wave-induced pressure inside the gaps, and thus, on the container, is critical for the stability of the structure, a detailed analysis of the pressure propagation inside the gap was performed.

Marth (2005) showed that the pressure impulse which enters a gap with rigid impermeable boundaries is damped while propagating through the gap. However, at the end of the gap the incoming pressures are reflected. Therefore, the pressures will be approximately doubled as a result of the superposition of the incoming and the outgoing compression wave. This superposition of the incoming pressure and reflected pressure signals could generate seaward displacement of elements of the coastal structure. Moreover, if the gaps are open at the end, the wave-induced pressures in the gap will be considerably smaller than those with “closed end”.

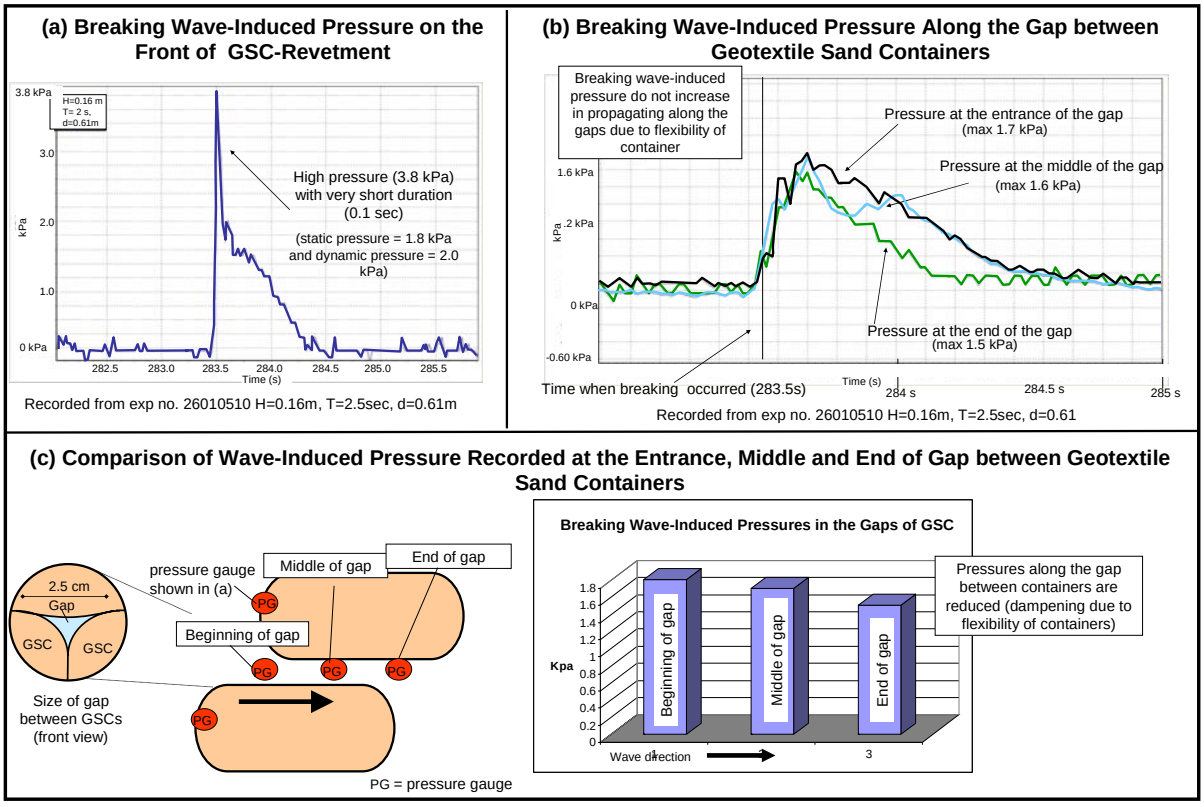

Figure 3-19: Pressure Propagation along a Gap between Geotextile Sand Containers

Using the results from the pressure measurements within the gap, it was observed that the pressure along the gap between the containers do not increase (Figure 3-19b). Moreover, at the end of the gap (just behind the instrumented container), the wave-induced pressure is lower than in the middle of the gap (Figure 3-19c). This

clearly shows that due to the flexibility and porosity of the containers, there is a decrease of pressure as it propagates along the gap. Recio and Oumeraci (2006b) also compared the wave-induced loads by breaking and non-breaking waves on GSC-structures (Table 3.2) and found that wave-induced forces by both types of waves are similar (higher instantaneous load for breaking wave). However, since the duration of the non-breaking waves is longer, it can be concluded that breaking waves are less critical for the stability of non-damaged GSC-structures than non-breaking waves. This is probably due to the flexibility of the GSCs which contributes to damp the pressure propagation along the structure.

Table 3.2: Comparison between Wave-Induced Pressures by Breaking / Non-Breaking Waves

	Breaking Wave	**Non- Breaking Wave**
Maximal wave-induced pressure (kPa)	3.8 (quasi static + impact =1.8+2.0=3.8)	1.8
Duration of maximal wave-induced pressure (sec)	0.1	1.2
Maximal total force (integration of pressures) (N)	33.49	55.87
Duration of maximal total force (sec)	≈0.40	≈0.60

3.3. Concluding Remarks

The conclusions from the model tests and analyses can be summarized as follows:

a) A further understanding of the wave-induced pressures and forces on GSCs has been achieved showing that the critical container for the hydraulic stability of a GSC-structure are the containers placed just below the still water level.
b) The critical situation for the revetment occurs during downrush.
c) The flow inside the revetment and the permeability of the structure strongly affect the stability of GSCs.
d) Breaking waves are not as critical as originally expected for the hydraulic stability of GSC-structures due to the flexibility and damping properties of the GSCs that attenuate the propagation of pressure inside the GSC-structure.

4. Acknowledgements

- The financial support of the first author by DAAD (Deutsche Akademischer Austausch Dienst) is deeply appreciated
- The model tests were financially supported by the Leichtweiss Institute (Hydromechanics and Coastal Engineering Department)
- NAUE GmbH & Co. KG provided the geotextile and technical advice on geotextiles used during the model tests.
- Some model tests, the numerical program for calculating the wave-induced forces and processing of data were performed by Sandra Burg.

Their help to this project is deeply appreciated.

5. References

Burg, S. 2006, Untersuchung zur hydraulischen Stabilität geotextiler Sandcontainer in einer Böschung unter Verwendung von MatLab, Studentarbeit (Master Student Project Report), Leichtweiss Institute for Hydraulic Engineering (in German).

Hinz M. and Oumeraci H. "Versuchtagebuch, Geotextile Sandcontainer Dünenbarriere" Internal Report, LWI, 2001, Germany (in German)

Führboter, A. Wellenbelastungen von Deich und Deckswerkböschungen. Jahrbuch der Hafenbautechnischen Gesellschaft, Band 46, 1991 (in German)

Marth R., Mueller G. and Wolters G., 2005. Damages of blockwork coastal structures due to internal wave impact induced pressures, Proceedings of the International Coastal Symposium, Ireland.

Oumeraci, H.; Bleck, M.; Hinz, M.; Möller, J. (2002a) Theoretische Untersuchungen geotextiler Sancontainer im Küstenschutz. Bericht des Leichtweiß-Instituts Nr. 866, Braunschweig (in German)

Oumeraci, H.; Bleck, M.; Hinz, M.; Kübler, S. (2002b): Großmaßstäbiliche Untersuchungen zur hydraulischen Stabilität geotextiler Sancontainer unter Wellenbelastung. Bericht des Leichtweiß-Instituts Nr. 878, Braunschweig. (in German)

Recio J. Analysis of a GSC laid on the Sea Bed. Internal Brief Report, 2005.

Chapter 4

Preliminary Model Tests on the Stability of a GSC and a Geotextile Mattress Placed on the Seabed

In this Chapter, the analyses of model tests of a GSC instrumented with pressure gauges placed on a mattress and on the stability of a geotextile mattress are presented. The Chapter is divided in three sections: (i) the analysis of instrumented GSCs placed on a sand mattress, (ii) a stability analysis of a geotextile mattress and (iii) a comparison of the measured and computed wave-induced velocity near the GSCs.

4.1. Analysis of an Instrumented Geotextile Sand Container (GSC) Placed on a Sand Mattress as Erosion Protection

The model tests were performed at the wave-flume of Leichtweiss Institute. The model tests consist in an instrumented GSC placed on a sand mattress subject to regular waves. Figure 4-1 shows the principle sketch of the model tests.

The **objectives** of the experimental investigations are:

- Clarification of the wave induced pressure-distribution on GSCs.
- Further understanding of the influence of wave parameters on the wave-induced pressures.
- Quantification of the variation of wave-induced velocities in front and over a GSC

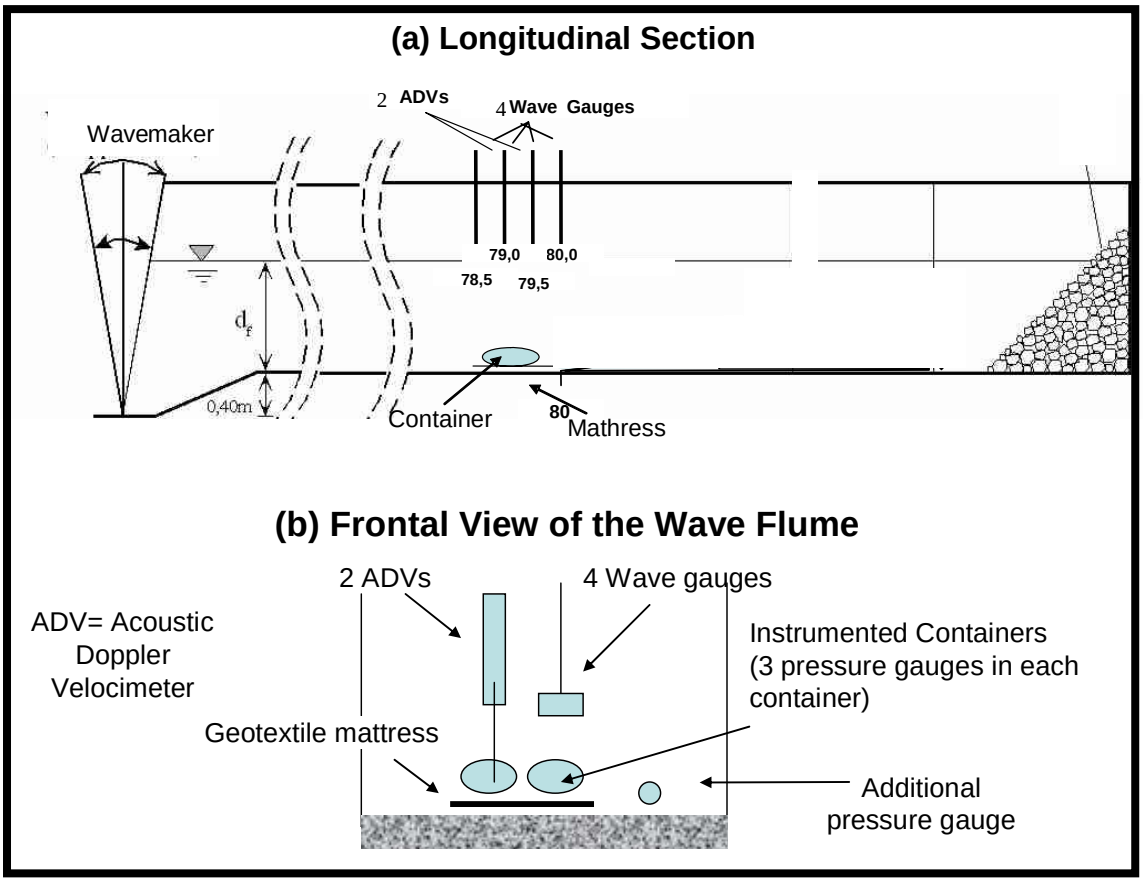

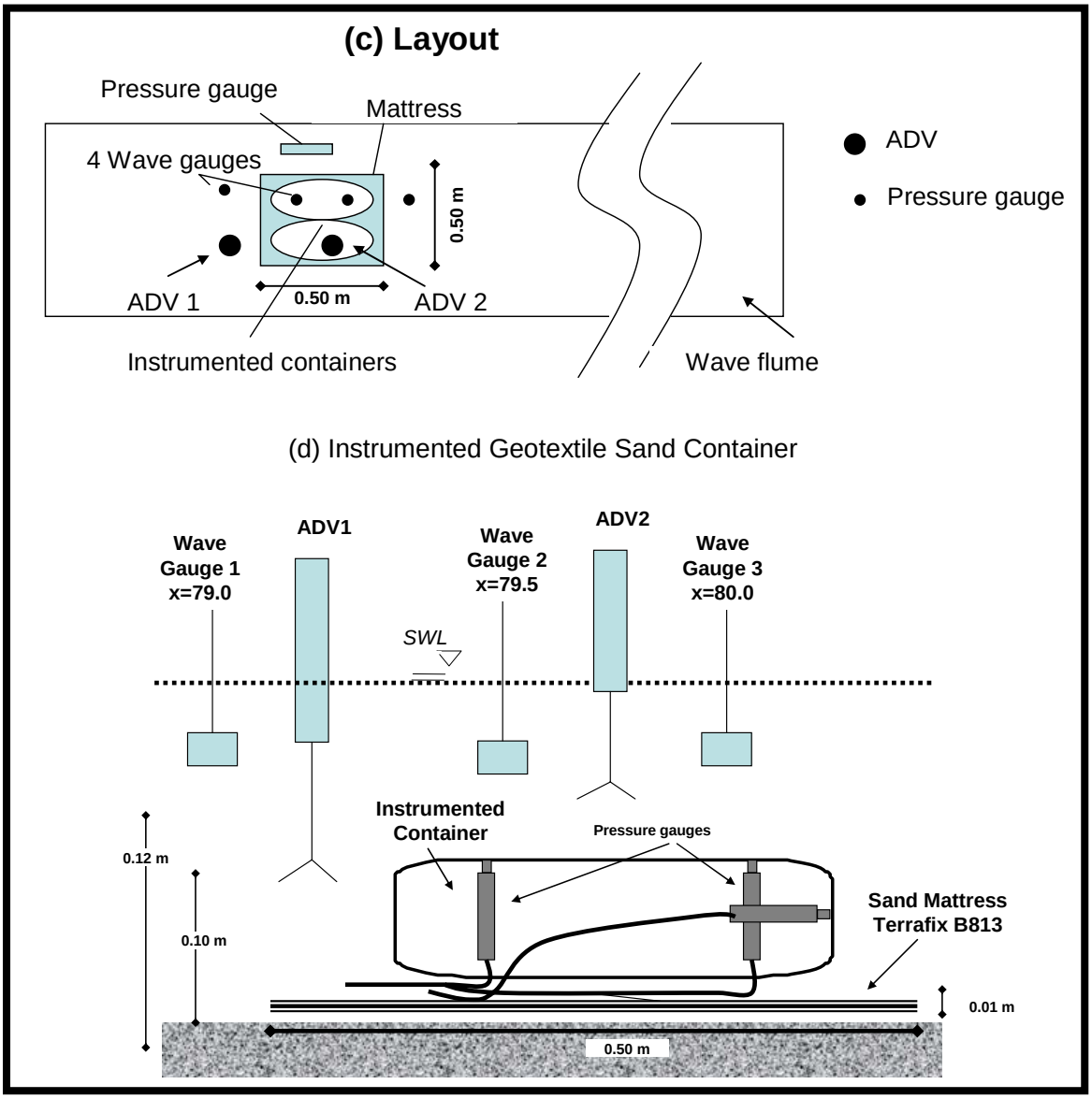

Figure 4-1: Experimental Set-Up (continued from previous page)

4.1.1 Measurements During the Model Tests

Local measurements at and near the GSC during the model tests consisted in wave common resistance type wave gauges, pressure gauges inside the instrumented container, ADVs (Acoustic Doppler Velocimeters) and video records of the area around the mattress and GSC (see Figure 4-1).

Instrumented GSC

The size of an instrumented container is shown in Figure 4-2. Two instrumented containers were used (same as used in Chapter 3 of this report): one with pressure gauges recording the wave-induced pressures on the top of the container and other with pressure gauges measuring the wave-induced pressures below the container. Due to size and scale limitations, only 3 pressure gauges per container were used.

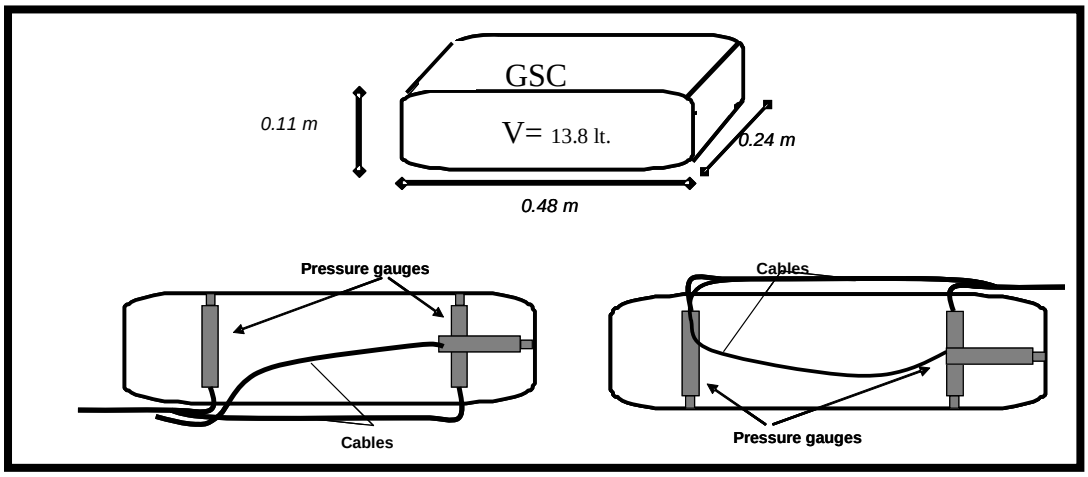

Figure 4-2: Instrumented Containers and Location of the Pressure Gauges inside the GSCs

Other Measurements

Two ADVs were used to record the wave-induced velocities in front and over the instrumented container (refer to Figure 4-1). The ADVs can record velocities up to 100 cm/s in three directions. ADVs were supplied by the company "Sontek".

An **additional pressure** gauge was placed on the bottom of the wave flume to record the wave induced pressures at the bottom of the wave-flume. The measurements from this pressure gauge are used to control the measurements from the instrumented container.

In addition, during the model tests, **video records** were performed. Since the containers are placed at the bottom of the flume, and considering that the water of the flume is it not very clean, quality of the records is not as it would be expected in clear water.

4.1.2 Photo Documentation

The model set-up and measuring devices are shown in Figure 4-3.

4.1.3 Geotextile-Sand Mattress

The geotextile mattress used in all stages was a "Goetextile Sand Mattress Terrafix B 813" with the following characteristics:
Mass per area: 6.100 g/m2, thickness: 11,5 mm, permeability 1.4 x 10^{-2} m/s (VI_{H50}Index), 2.63 x 10^{-3} m/s (k_{10}) (for more information on the sand mattress refer to Naue 2004). The dimensions of the sand mattress placed under the containers were 0.50 x 0.50 m.

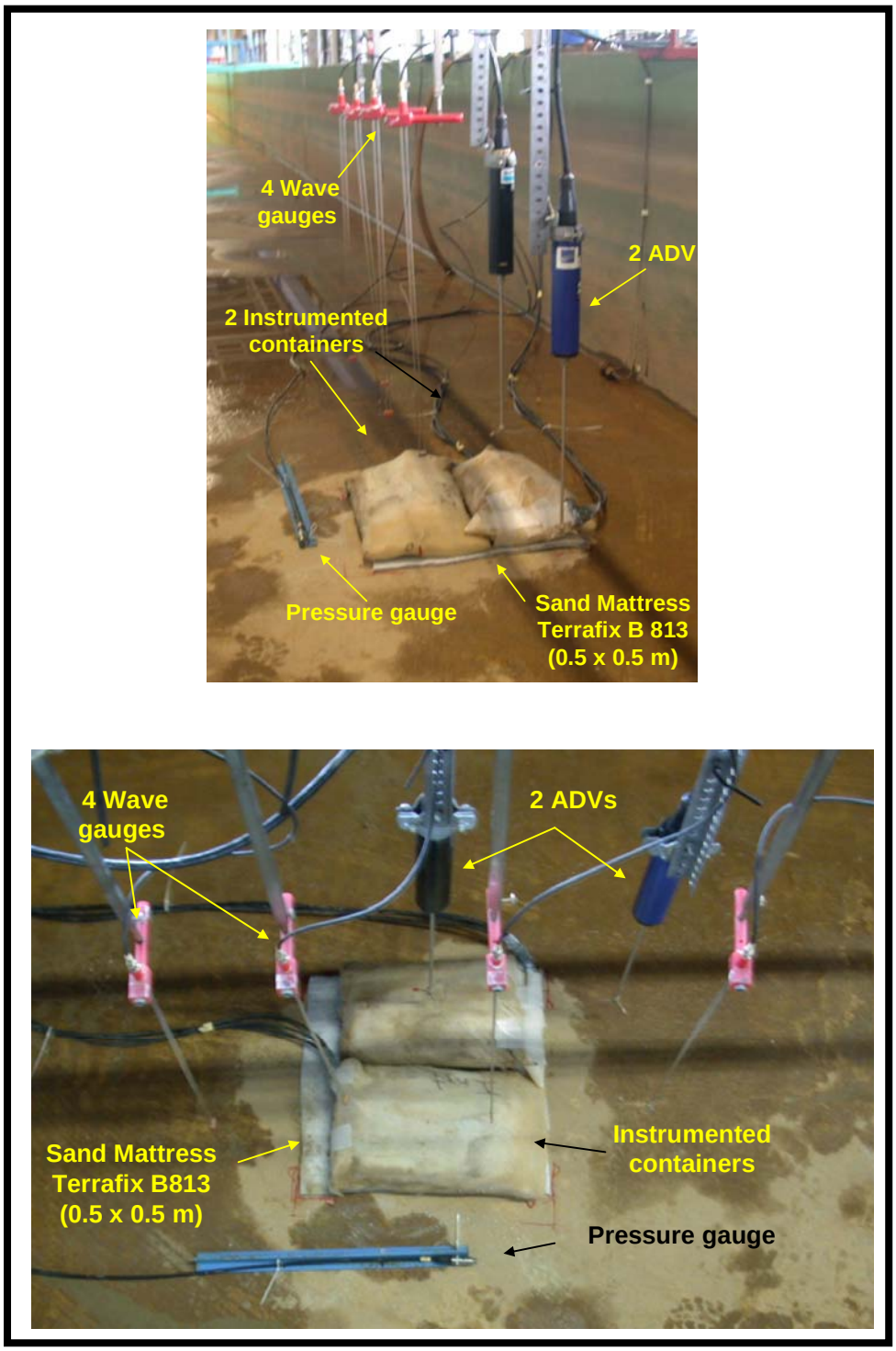

Figure 4-3 Photos of the Experimental Set-Up

4.1.4 Model Wave Conditions

The wave conditions used in the model tests are shown in Table 3.1 which were selected based on the following criteria:

- Wave conditions should approximately follow the same pattern of wave conditions tested at the GWK in Hanover for scour protection systems.
- Waves should include the longest wave that the wave maker can generate.

Table 4.1 Wave Conditions at LWI Wave-flume

		Wave Period (seconds)			
Depth (meter)	**Wave Height (meter)**	**1.5**	**2**	**2.5**	**3**
0.700	**0.11**		**R**	**R**	**R**
	0.14		**R**	**R**	**R**
	0.17	**R**	**R**	**R**	
	0.19	**R**	**R**	**R**	
0.610	**0.11**		**R**	**R**	**R**
	0.14		**R**	**R**	**R**
	0.17	**R**	**R**	**R**	
	0.19	**R**	**R**	**R**	
Experiments with Regular					
Every model test consists in 200 waves.					

4.1.5 Selected Model Test Results

The first analyzed results are those obtained from the pressure gauges installed inside the instrumented container (Figure 4-2).

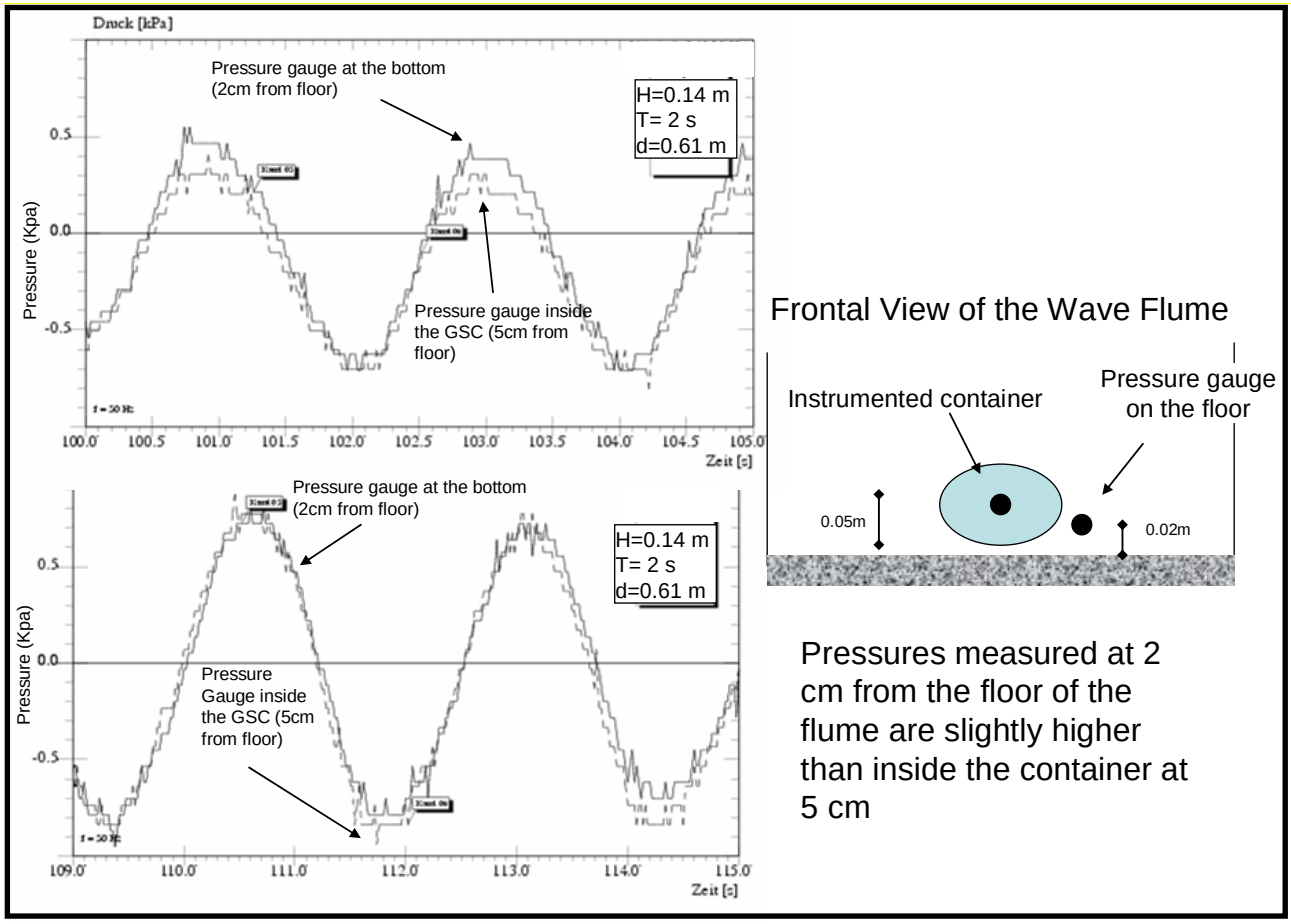

Figure 4-4: Comparison between Pressures at the Bottom of the flume (2cm from floor) and Pressure in the Frontal Part inside of the Container (5cm from floor).

Results show that the wave-induced pressures on the surface of the container and the pressure gauge placed at the bottom of the flume follow the same pattern. In

addition, waves with longer periods induce larger pressures on the container. For example, it was seen that a wave with a wave height of 0.14m and 2.5s induced smaller pressures than a wave with wave conditions of 0.11m and 3 s.

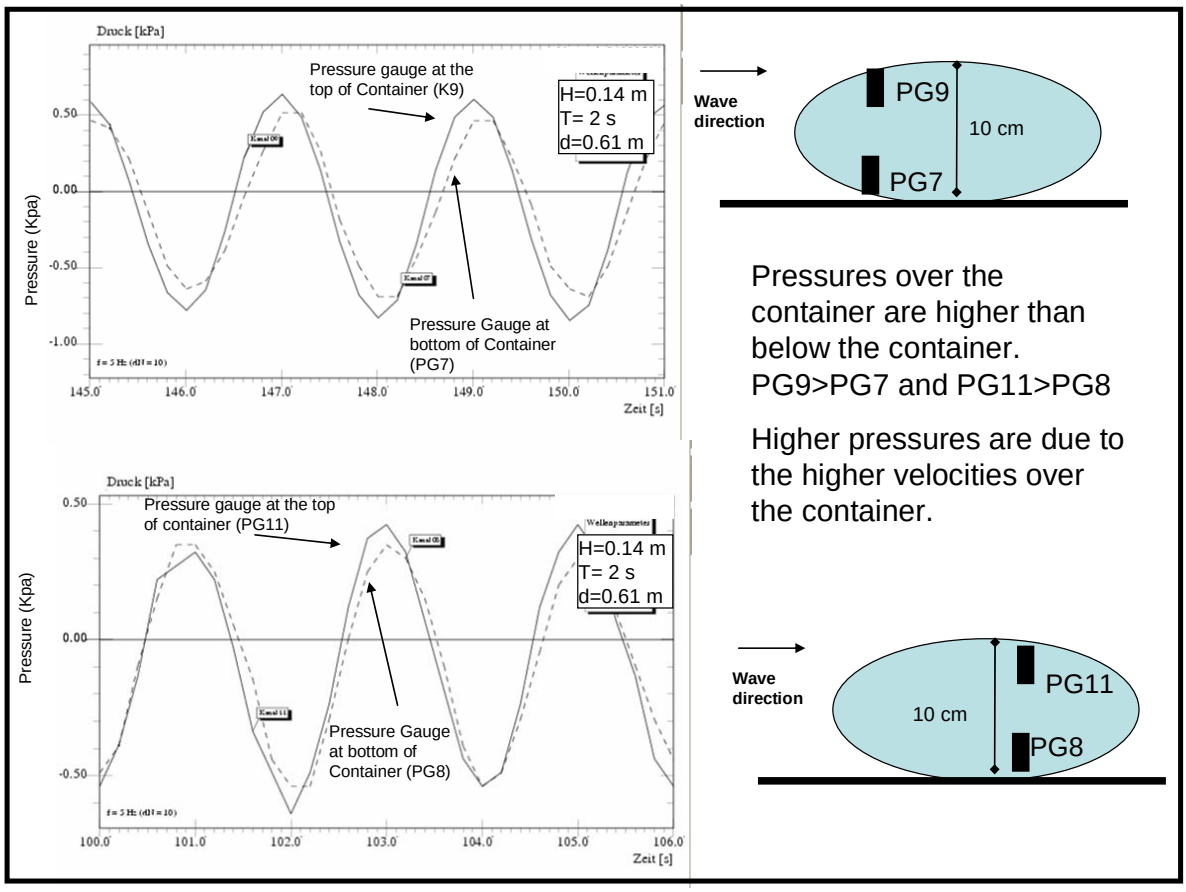

Figure 4-5: Comparison between Wave-induced Pressures Over and Beneath the GSC

Figure 4-4 shows the comparison between the pressures obtain from a pressure gauge that was near the bottom of the flume and the other inside the instrumented container. Both of the pressure gauges had the same “x” position but different “y” (one is 2 cm and the other 5 cm from the floor respectively). It can be seen that the pressures are very similar. The pressures at 2 cm are slightly higher than at 5 cm.
Figure 4-5 shows the comparison between pressure gauges inside the instrumented container. It can be seen that wave induced pressures over the container are higher than below. This can be explained due to the higher wave induced velocities over the container.

4.1.5.1 Pressure Integration of Instrumented GSC

The main advantage of having pressure gauges inside a container is that the whole pressure that acts around the container can be obtained by interpolating the values from the pressure gauges.
The integration of pressures around the container was performed by interpolating the values from the pressure gauges. The resultant total wave force (magnitude, direction) on the container could be calculated from the pressure-integration.
Figures 4-6 and 4-7 show the results of the two analyzed model tests. These graphs show how the wave is inducing pressure at different phases of the incident wave above the container (centre of the figure). This information further clarifies the wave-loading on the containers during wave action

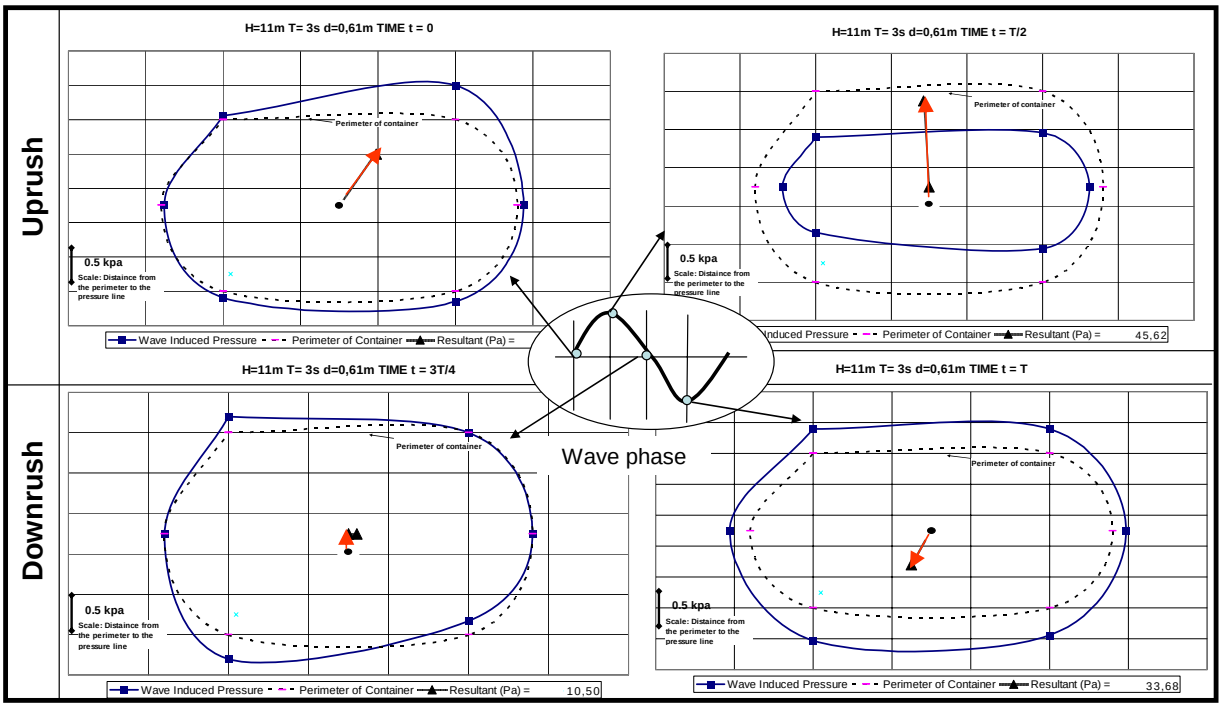

Figure 4-6: Wave Pressures and Total Force (H= 0.11m. T= 3 s, d= 0.61m)

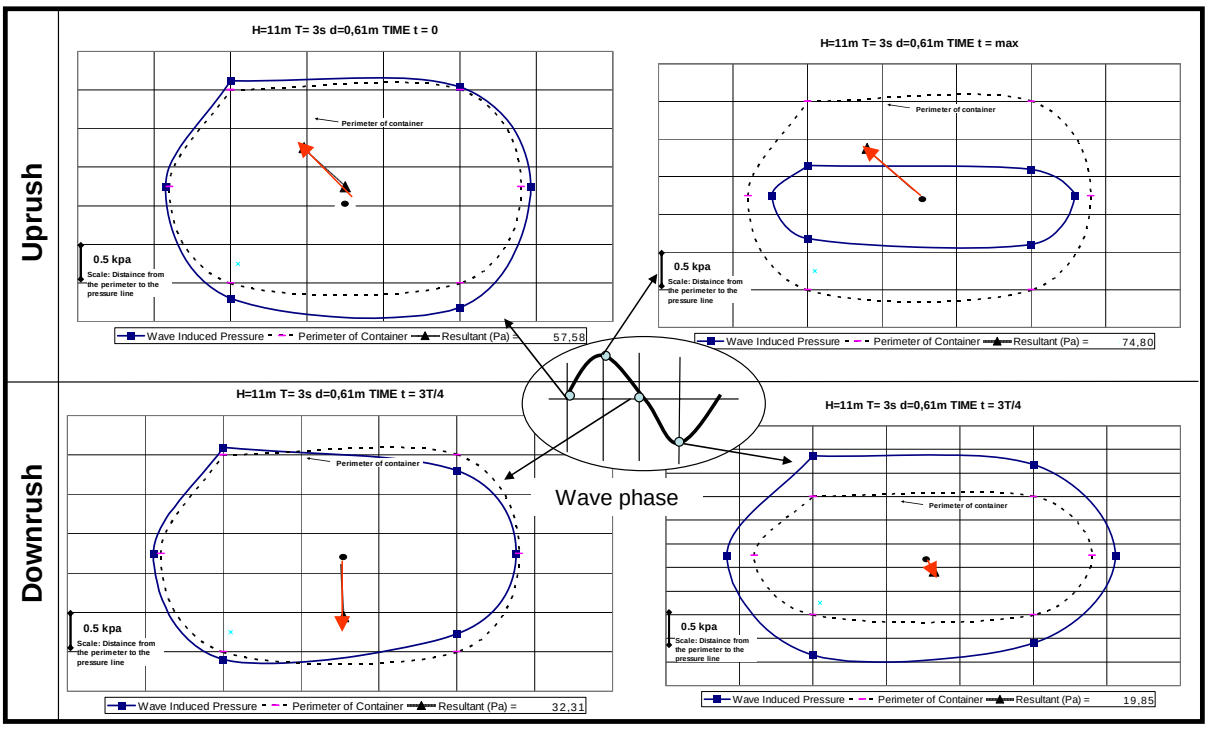

Figure 4-7: Variations of Pressures During Wave Action and Total Force (H= 0.11m. T= 3 s, d= 0.61m)

The most important advantage of having these wave induced pressures around the container is that the total resultant force of the container can be obtained at each time step of the wave cycle. This means that the most critical scenario for the container can be identified.

4.1.5.2 Wave Phases Obtained from the Model Tests

In an attempt to obtain the drag and inertia coefficients affecting the GSCs, the wave phases of some model tests were analyzed. It was found, however, that the scale effect does not permit to obtain reliable coefficients. The ratio between the wave length and the dimension of the container will restrict the applicability of the Morrison Formula (Diameter of GSC / Wave Length). However, in order to clarify the process, the phases acting on the centre of the GSC are shown in Figure 4-8.

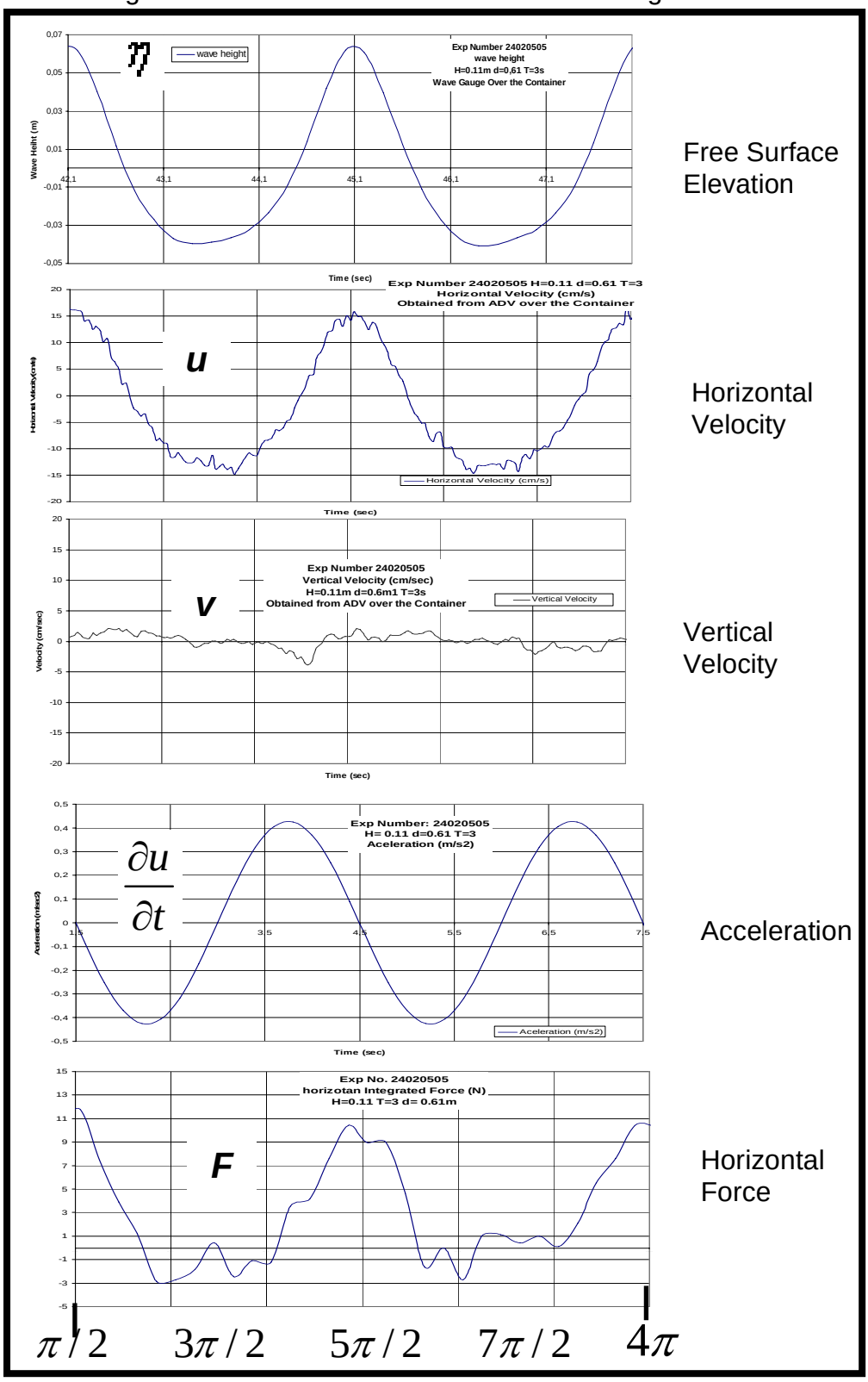

Figure 4-8: Wave Phases of Analyzed Model Test

It can be seen from Figure 4-8 that the peak of the horizontal velocity is close to the peak of the wave-induced horizontal force indicating that the drag force dominates over the inertia force. However, the peaks do not match and there is a slight “phase shift”, indicating that an inertia force component is also present.

4.1.5.3 Wave-Induced Velocities in front and over the Instrumented Container

As shown in Figure 4-1 the wave-induced velocity was recorded by means of acoustic velocimeters. The objective of these measurements was to quantify the variation of velocities around the container during wave action and then, derive a correlation between particle velocities and wave induced pressures.

Regarding the flow interaction at the containers (Figure 4-9) the streamlines are not symmetric to vertical axis, therefore there will be a drag force, inertia and lift force. The variations of the velocities in front and above the container during wave action help to the further understanding of the wave-induced loading on the containers.

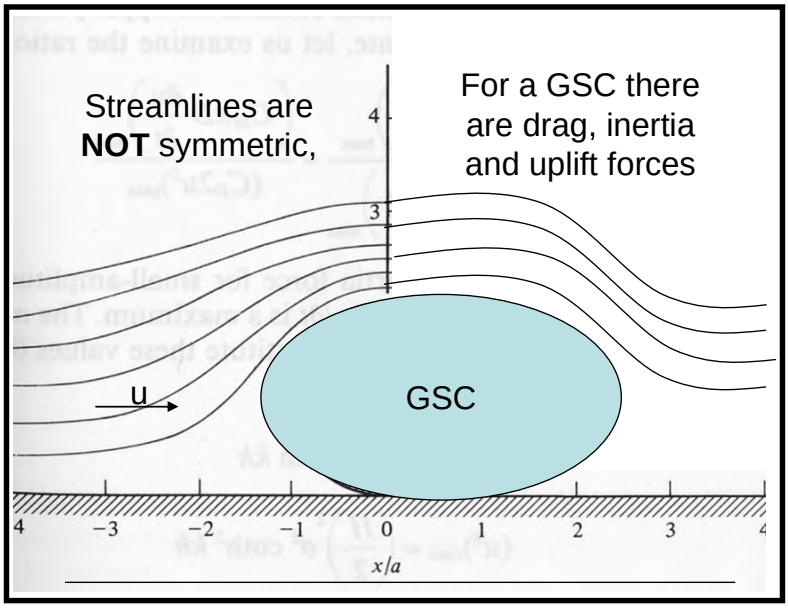

Figure 4-9: Flow Field over a GSC Placed on the Seabed

The data obtained from two ADVs is shown in Figure 4-10. Results show that the velocities over the container are higher than the velocities in front of the containers, velocities are however, in the same order of magnitude.

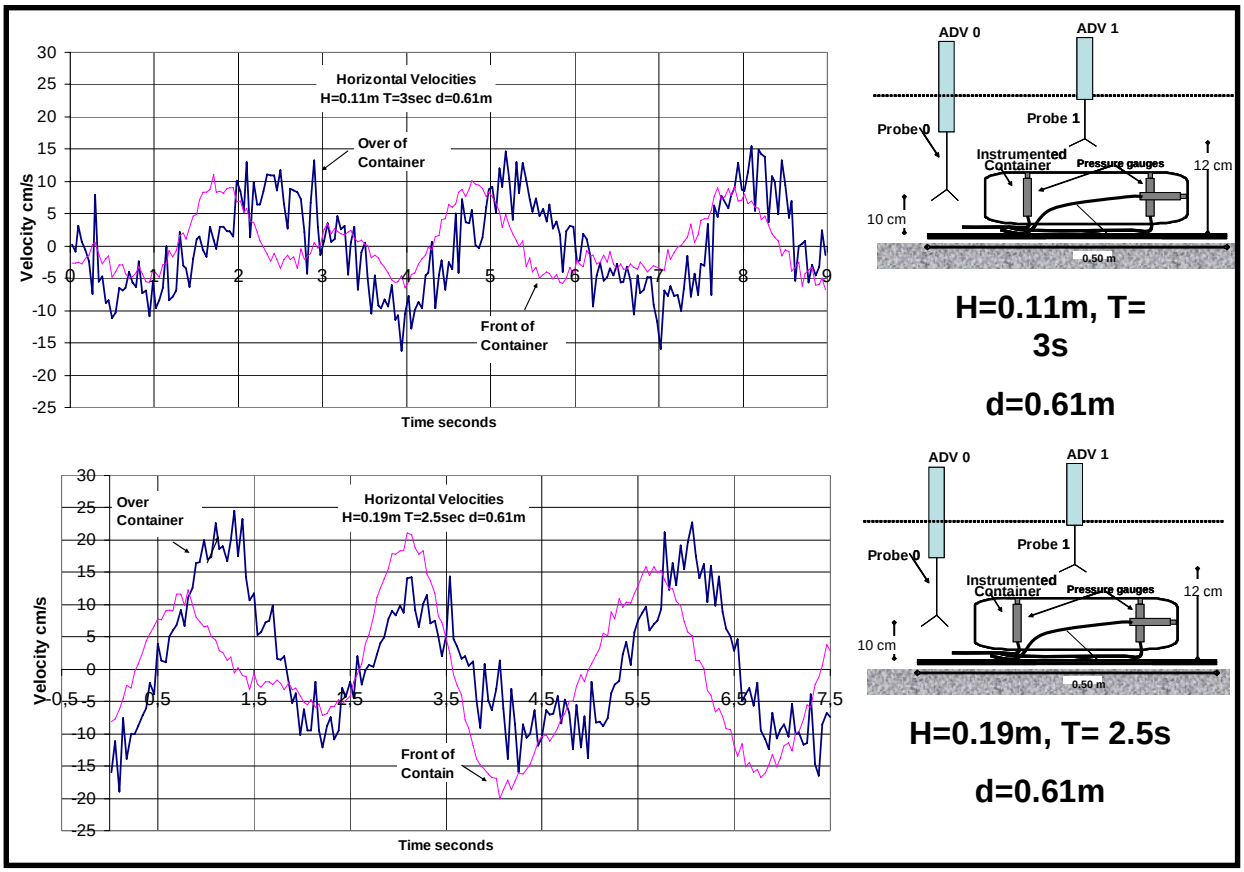

Figure 4-10: Wave-Induced Velocities in front and over a GSC During Wave Action

4.1.6 Concluding Remarks

The tentative conclusions from the analysis presented in this section can be summarized as follows:

(i) Instrumenting a GSC with pressure gauges allows to describe the stability behaviour and deformation of the sand container under varying wave loads. The wave pressures around the container follow the same pattern independently of the wave conditions.

(ii) By integrating the forces around the container, the resultant force at every time step could be obtained. This means, that the most critical situation for the container can be easily identified.

(iii) It was confirmed that the velocities over the container are higher than those in front of it.

4.2. Stability Analysis of a Geotextile Sand Mattress Terrafix B 813 for Seabed Protection

In this section, the stability of a sand mattress was investigated by means of model tests involving a sand geotextile mattress placed on the bottom of the wave-flume.
A "sand geotextile mattress" consists in two geotextiles "sandwiching" granular material. Such mattress are been used as innovative erosion protection systems for coastal structures.

4.2.1. Experimental Set-Up

The model test consists on a sand mattress laid directly on the floor of the wave-flume and then subject to different kinds of regular waves. The cross section and front view follow the same pattern explained in section 1 (Figure 1.1). Figure 2.1 shows the principle sketch of the model tests.

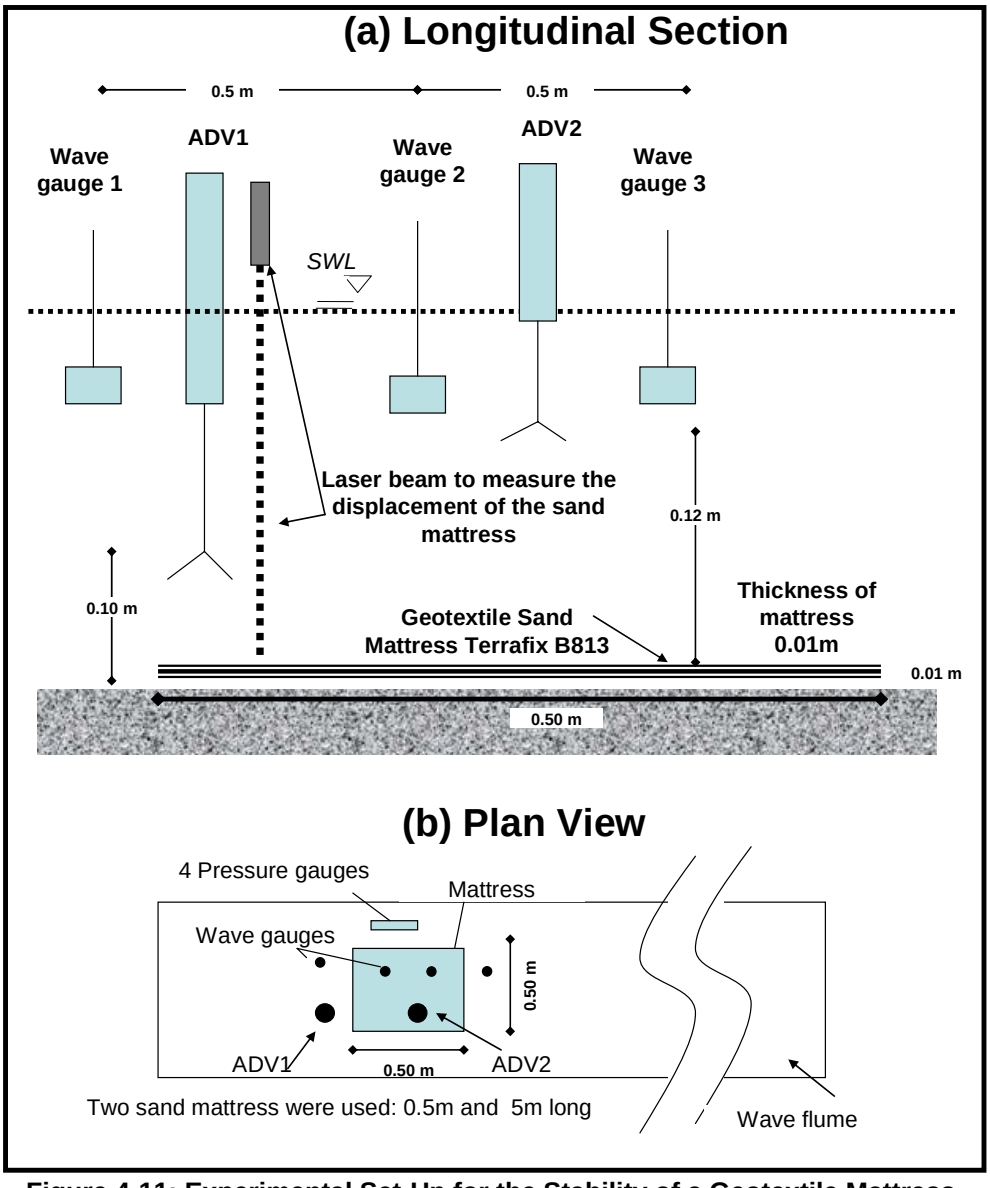

Figure 4-11: Experimental Set-Up for the Stability of a Geotextile Mattress

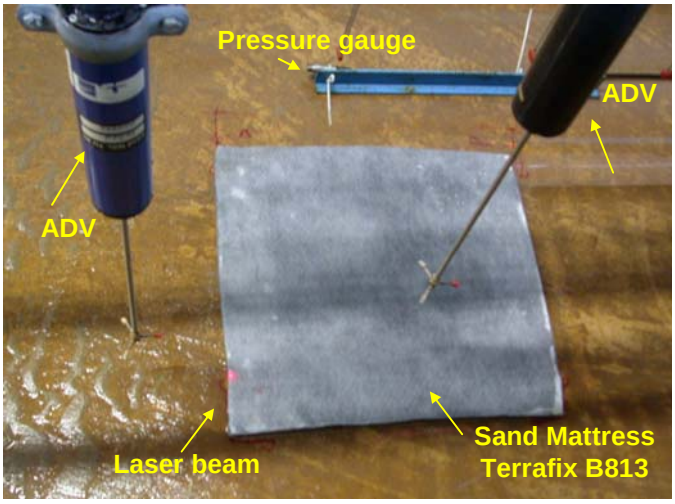

A laser beam was used to measure the displacement of the geotextile mattress

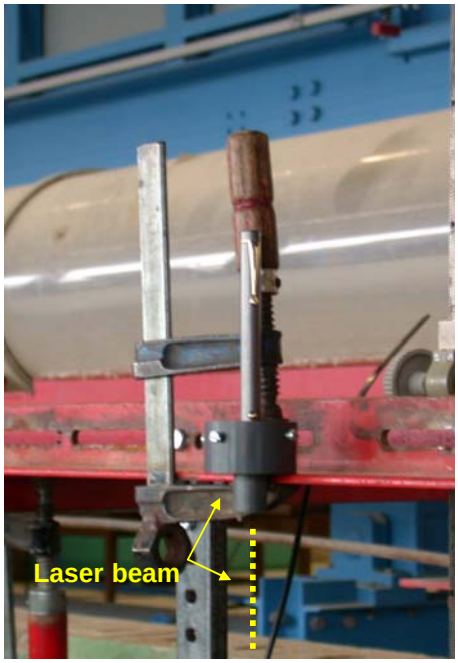

Figure 4-12: Model Set-Up of the Geotextile Mattress Tested in the LWI Wave-Flume

The objectives of the model tests are:

- Investigation of the stability of the geotextile sand mattress under wave action.
- Quantification of the influence of the wave parameters on the stability of the mattress.

4.2.2 Measurements During the Model Tests

Measurements during the model tests consisted in wave gauges, a pressure gauge on the floor of the wave flume, ADVs (Acoustic Doppler Velocimeters) and video records.

In order to **measure the displacement** of the sand mattress during the model test, a commercially available "laser" (commonly used for presentations) was installed in the wave flume (Figure 4-12). By using a laser as a reference, the displacement of the geotextile sand mattress can be accurately recorded.

4.2.3 Geotextile-Sand Mattress

The geotextile sand mattress used during the model tests was the "Terrafix B 813" produce by the company NAUE GmbH & Co. KG. Two mattress with different lengths were investigated (Figure 4-13).

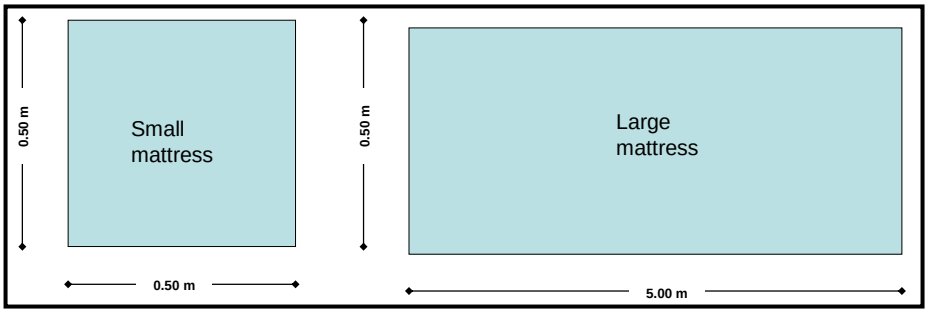

Figure 4-13: Dimensions of the Two Used Geotextile-Sand-Mattress

4.2.4 Wave Conditions

The wave conditions used in the model tests are shown in Table 4.2.

Table 4.2 Wave Conditions (for Small and Large Sand Mattress)

		Wave Period (seconds)			
Depth (m)	**Wave Height (m)**	**1.5**	**2**	**2.5**	**3**
0.61	**0.11**			**R**	**R**
	0.14		**R**	**R**	**R**
	0.17	**R**	**R**	**R**	
	0.19	**R**	**R**	**R**	
Experiments with regular waves					
Every model test consists in 200 waves.					

4.3 Selected Model Test Results

4.3.1 Stability Analysis of the Small Sand Mattress (0.5 x 0.5 m)

The results of the model tests are summarized in Table 4.3. The sand mattress was considered as unstable when its displacement was higher than 3cm.

Table 4.3; Model Test Results on the Stability of the Mattress (Small Sand Mattress)

Model test Number	Wave Height (cm)	Period (sec)	Stable?	Displ. (cm)	Observations
25020504	19	2.5	NO	63	The sand mattress also suffered rotation and moved in both directions. The sand mattress, also “floated” for approx 20 seconds
25020505	19	2	NO	+600	The sand mattress was transported by the waves, landing back in the floor approx 6 meters away
25020506	19	1.5	Yes	3	The sand mattress moved only few cms during the first waves and then remained stable for the rest of the test
25020507	17	2.5	NO	5	The sand mattress only moved with the first waves, and then remained stable for the rest of the test
25020508	17	2	NO	42	Sand mattress “floated” for some seconds and then remained stable for the rest of the test
25020509	17	1.5	Yes	0	No movement of the sand mattress
25020510	14	3	NO	46	Sand mattress was displaced constantly with the waves. Displacement was in both directions
25020511	14	2.5	NO	26	Sand mattress moved in both directions and rotated on its axis
25020512	14	2	Yes	0	No movement of the sand mattress
25020513	11	3	Yes	2	Mattress moved only 2 cm, it was not observed when the movement occurred.
25020514	11	2.5	Yes	0	No movement of the sand mattress

As expected higher wave conditions resulted in larger wave-induced velocities and thus, lower stability of the mattres against wave action.

In addition, the movement of the geotextile-mattress followed in most cases the same pattern which is illustrated in Figure 4-14.

The displacement of the mattress occurred mainly during the first waves. The mattress starts to “fold” in the upward direction (uplift-deformation). The “folding” occurs alternatively at both ends; this means when the front end is uplifted the back edge is on the floor.

Displacement occurs when the front end of the sand mattress is uplifted and cannot return to the bottom when the back end is also “uplifted”. This causes the sand mattress to “float” for a while. Subsequently, the mattress will be carried by the waves.

In some model tests, very small movement of the mattress was observed (less than 3 cms). For these cases, the displacement was not progressively noticed and therefore still to be explained.

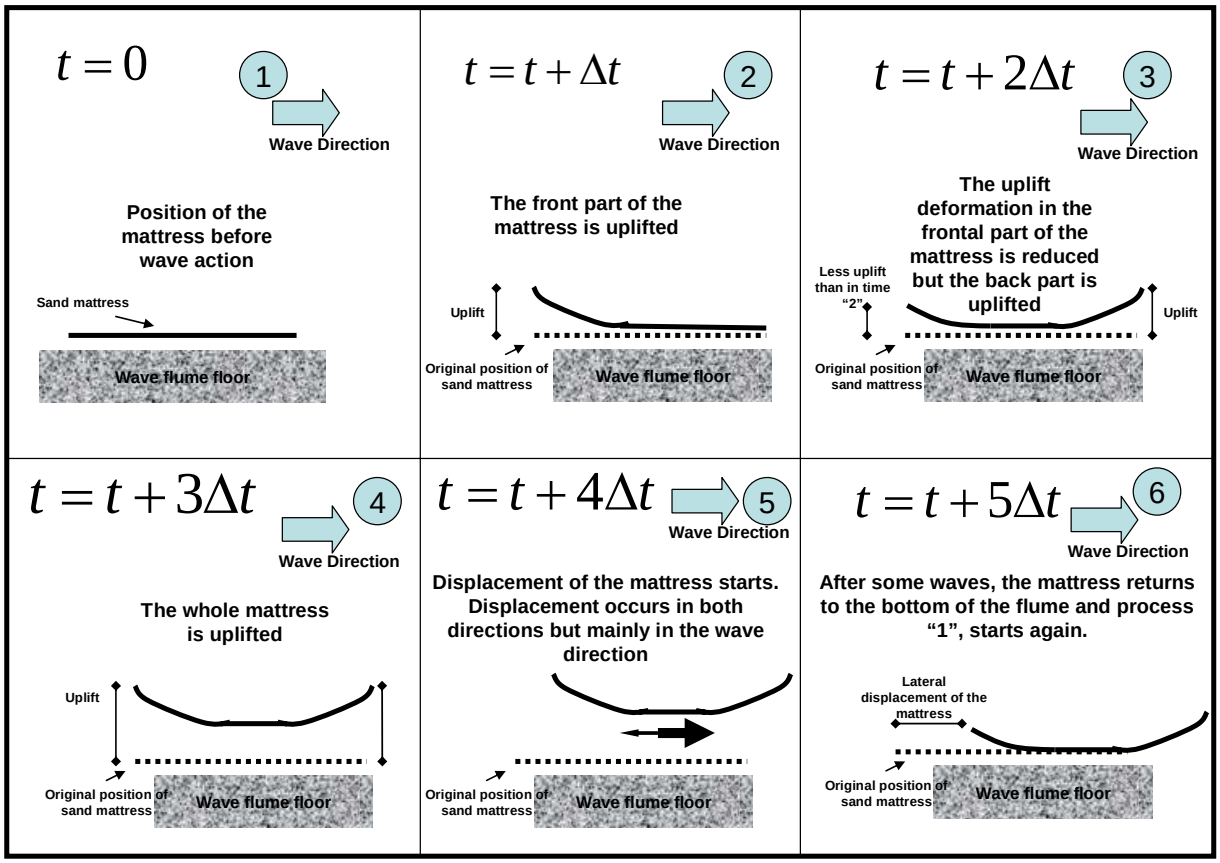

Figure 4-14: Displacement Mechanisms of Sand Mattress

4.3.1.1 Influence of Wave Parameters on the Stability of a Small Geotextile Sand Mattress

The influence of the wave conditions on the stability of the geotextile sand mattress is shown in Figure 4-15. Higher wave conditions induce lower stability of the mattress while a stability threshold is well defined.

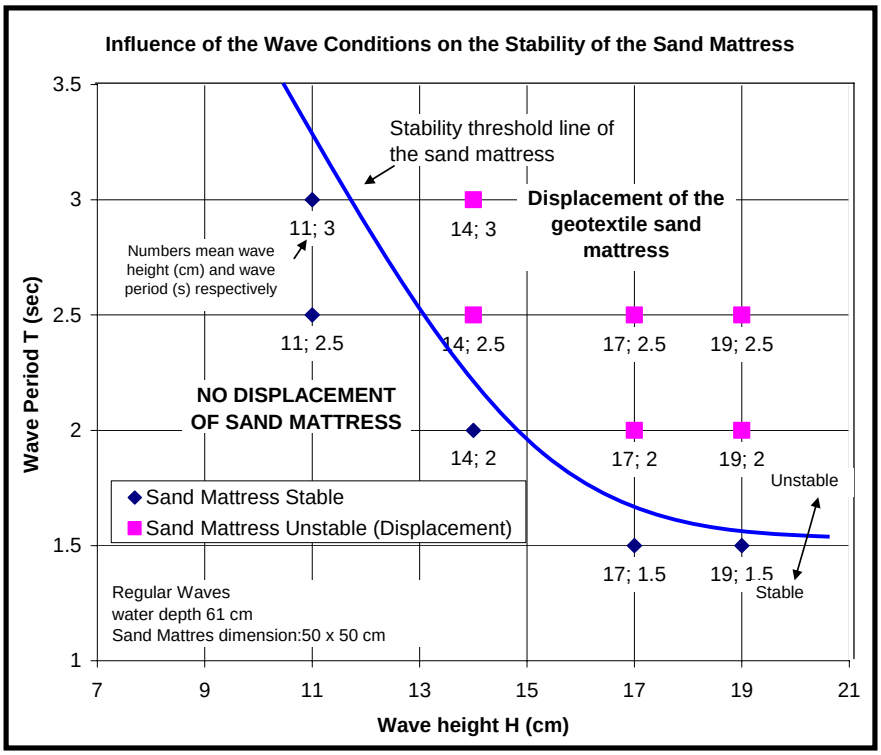

Figure 4-15: Influence of the Wave Parameters on the Stability of the Mattress

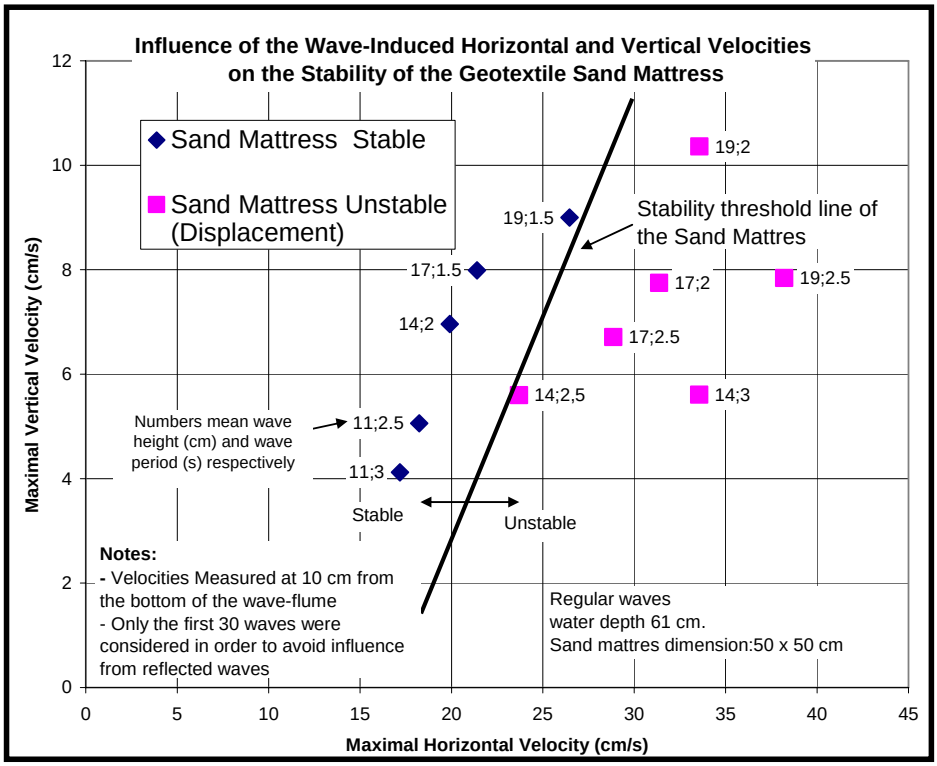

Figure 4-16: Influence of Wave-Induced Horizontal and Vertical Velocities on the Stability of the Geotextile Sand Mattress

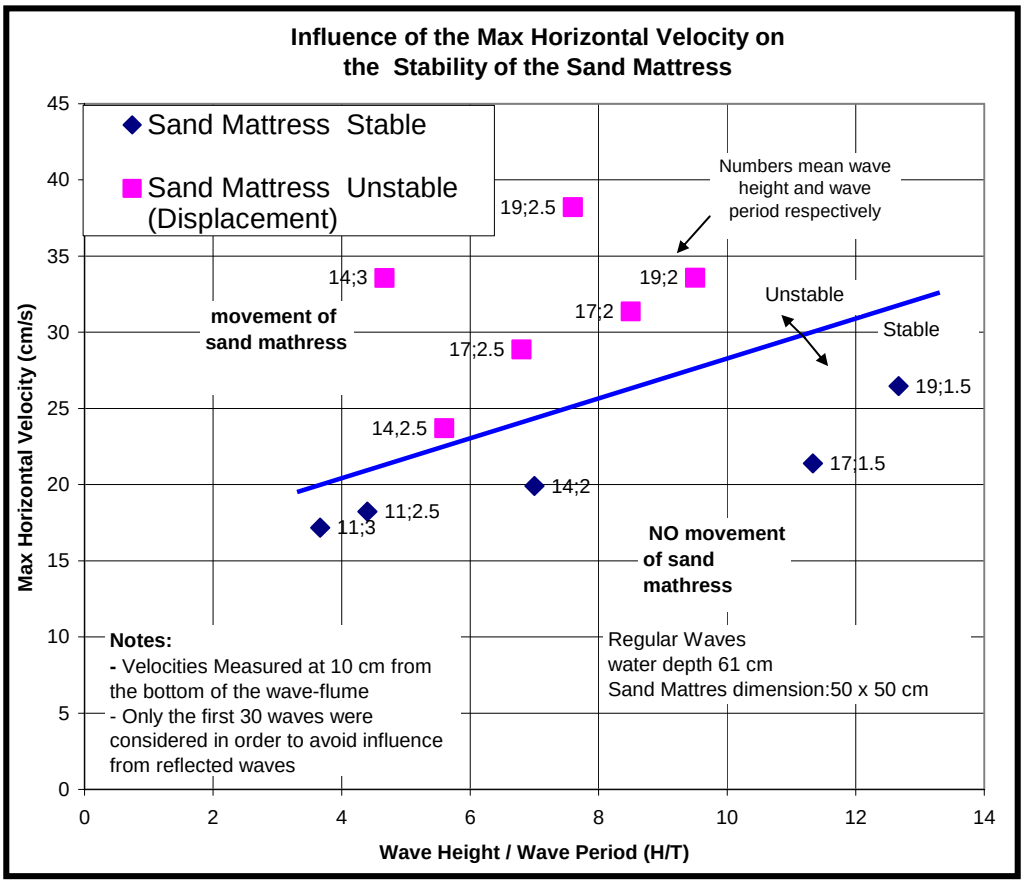

Figure 4-17: Influence of the Wave-Induced Horizontal Velocity on the Stability of the Geotextile Sand Mattress

On the other hand, Figure 4-16 shows the influence of the velocities on the stability of the sand mattress showing that the horizontal velocity influences considerably more the stability of the mattress than the vertical velocity.

Moreover, Figure 4-17 shows the relation between the horizontal velocity and the wave conditions (H/T) showing that the threshold of displacement is for approximately a wave-induced horizontal velocity of 20 cm/s.

4.3.1.2 Influence of the Wave Parameters on the Stability of a Large Geotextile Sand Mattress (0.5 m x 5m)

Model tests were also performed using a large geotextile sand mattress to investigate the influence of the size of the mattress on the stability. However, for all the tests, the large geotextile sand mattress remained stable (Figure 4-18 and Table 3.4)

Table 4.4 Stability of a Large Sand Mattress (d=0.61m)

Model test Number	Wave Height (cm)	Period (sec)	Stable?	Displ. (cm)	Observations
25020515	19	2.5	Yes	0	No movement of the sand mattress
25020516	19	2	Yes	0	
25020517	17	2.5	Yes	0	
25020518	17	2	Yes	0	
25020519	14	3	Yes	0	

4.3.1.3 Comparison Results from Small and Large Sand Mattress

The influence of relation wave length- length of mattress (L/l) is shown in Figure 4-18 showing that that the stability threshold is clearly defined.

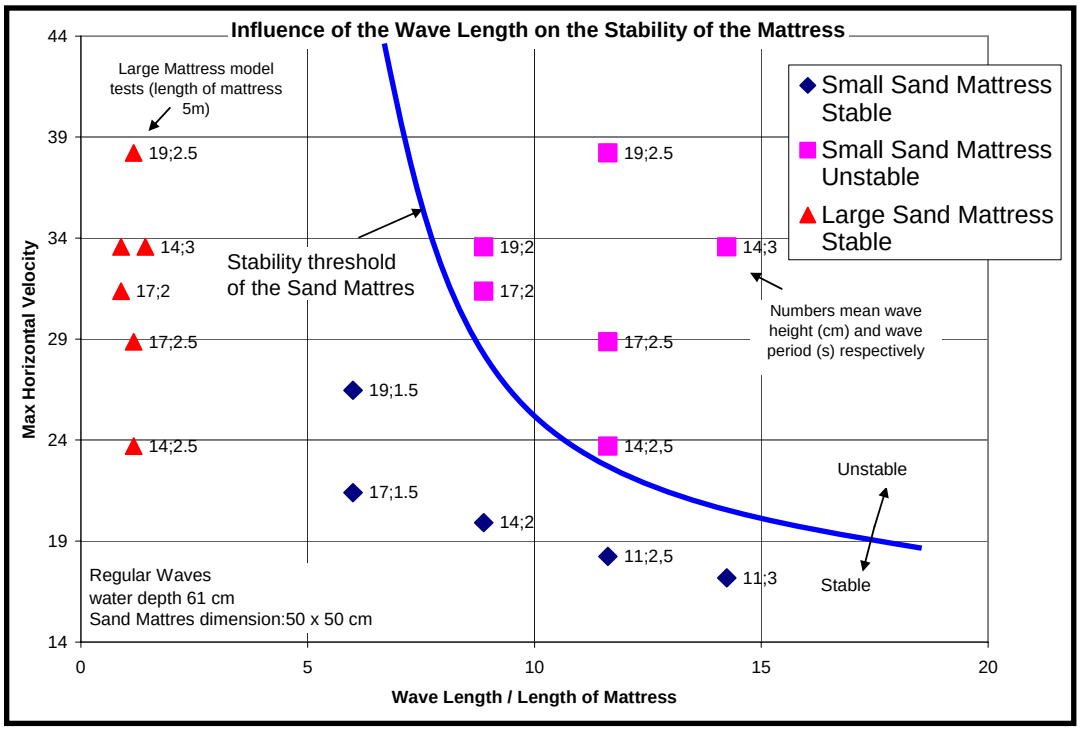

Figure 4-18: Influence of the Wave Length on the Stability of the Mattress

4.3.2 Concluding Remarks

The conclusions of the stability analysis of the sand mattress can be summarized as follows:

- The wave period has a large influence on the stability of the sand mattress, the longer the period, the lower the stability of the sand mattress.
- The wave induced horizontal velocity influences more the stability of the sand mattress.

IMPORTANT NOTE: The stability analysis presented in this section did not consider any scaling effect. This means that the prototype was directly used in the small-scaled model tests. Therefore most of the relations are presented related to the wave induced velocities. Further testing considering scale effects have to be conducted.

4.4 Comparison between Experimental and Numerical Results

In this section, results obtained from model tests are compared with results obtained from numerical simulations. The numerical simulations were performed by using the commercial available software “Wave Loads”.

4.4.1 Objectives

The objectives of this section can be summarized as follows:

- Validate the results obtained from model tests.
- Investigate the agreement between measured results and available wave theories.

4.4.2 Experimental Set Up

The data used in this section was obtained from model tests involving an acoustic velocitmer as shown in Figure 4-19.

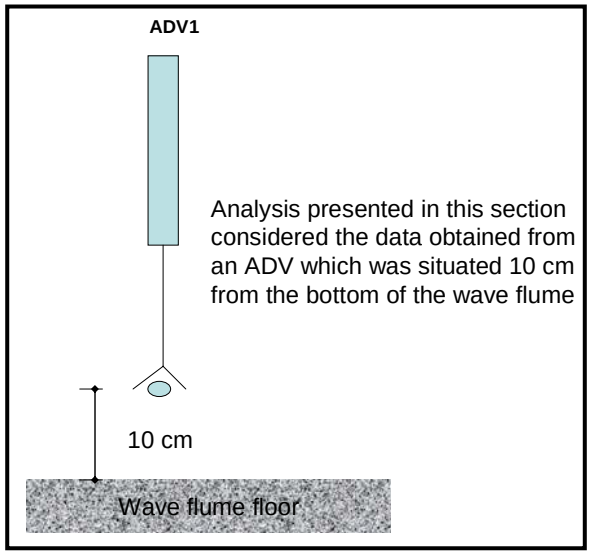

Figure 4-19: Location of the ADV in the Wave Flume

4.4.2.1 Data Used for the Comparisons

The data used for the comparisons was obtained from an ADV situated 0.10m from the bottom of the wave flume (Figure 4-19).
The ADV records velocities in the horizontal and vertical direction; however only horizontal velocities were used for the analysis.

4.4.2.2 Wave Conditions Used in this Section

Table 3.1 shows the wave conditions compared in this section.

4.4.3 Brief Description of the Commercial Software “Wave Loads”

“Wave Loads” was originally develop at the University of Hannover and its main capabilities are: (i) derivation of wave-induced velocities at any depth and (ii) derivation of wave-induced forces on slender elements (“hydraulic transparent structures”)

Table 3.5: Wave Conditions Analyzed in this Section

		Wave Period (seconds)			
Depth (meter)	**Wave Height (meter)**	**1.5**	**2**	**2.5**	**3**
0.700	**0.11**				**R**
	0.14		**R**		
	0.17				
	0.19	**R**		**R**	
0.610	**0.11**				**R**
	0.14		**R**		
	0.17	**R**			
	0.19			**R**	

4.4.4. Comparison between Obtained and Calculated Wave-Induced Velocities

The comparison of wave-induced horizontal velocities between the model tests and the simulations is shown in Figure 4-20. The comparisons were performed considering the velocities measured at a distance of 0.10 m from the bottom of the wave-flume.

It can be clearly seen that model tests results and the different wave theories are in good agreement. The maximal velocities have better agreement than the minimal velocities. However, it is impossible to decide which wave theory has the best agreement with the measured data.

4.4.5 Concluding Remarks of This Section

From the comparisons presented in this section it can be summarized that:

- Experimental and numerical results are in relatively good agreement.
- From the present data it is impossible to decide which wave theory is more suitable for simulating waves in a wave flume. Further investigation and discussions are necessary.
- “Wave Loads” is a helpful tool for obtaining the velocities at any depth.

References

Dean G. R. and Dalrymple 1998, Water Wave Mechanics for Engineers and Scientists, World Scientific, Volume 2.

Naue Fasertechnik 2004, Sandmatten Terrafix B609 G5 and Terrafix B813, Technical Broschure (in German).

Führboter A. 1992, „Strömungenverhalten von Geotextilen“ (Current behaviour of Geotextiles), Report for Naue Fasertechnik

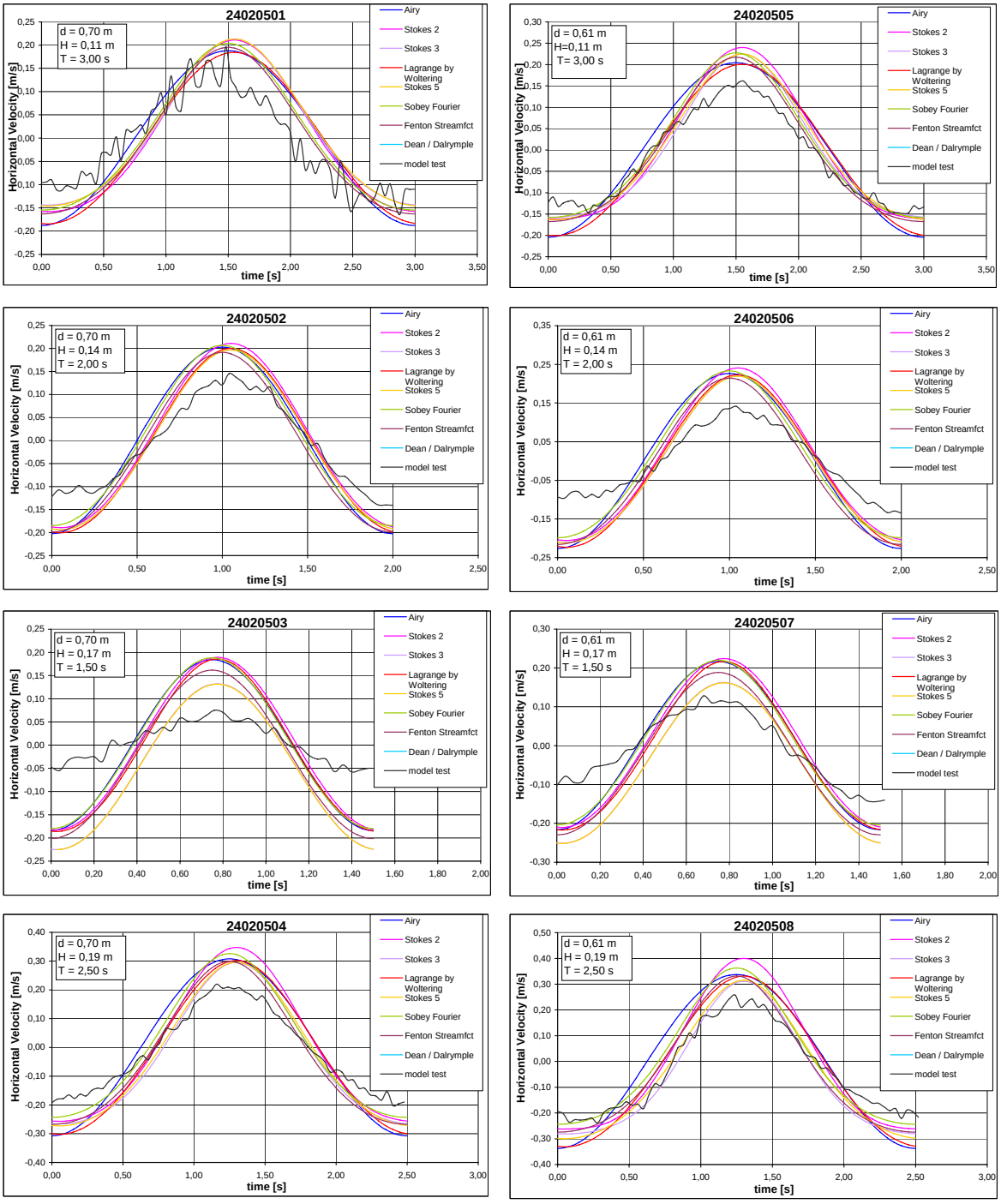

Important Note: Model Test velocities were obtained at 10 cm from the bottom while the results from the numerical simulations are **mean** velocities in the range from the bottom to 10 cm

Figure 4-20: Comparison between Results Obtained from Model Tests and from Numerical Simulations Obtained by Using "Wave Loads".

ANNEX 1:
Theoretical Background of PIV

Introduction

In this annex, a brief explanation of the theoretical background behind PIV is explained. The annex explains the main elements of a PIV system and explains their most important numerical basis.

Particle Image Velocimetry (PIV) is a relatively new method being used to determine velocities within a fluid in motion.

The theory behind Particle Image Velocimetry is very simple. By adding tracer particles into a fluid, it is possible to see exactly how the fluid is moving and how it reacts to structures or anything else that may disturb the flow. Images of the flow field can be analyzed to create velocity vector fields showing the speed and direction of movement of the fluid throughout the entire flow field at any instant. In practice, however, the method is much more complicated. Very sophisticated equipment is required and the experiment must be carefully and meticulously constructed and run if the results are to be satisfactory. In general, PIV experiments use a laser (or other sources of light) that emits a pulse of light in the form of a thin sheet, which illuminates a small section of a flow field containing tracer particles. These tracer particles have fluid mechanical properties very similar to the fluid used in the experiment, which allow them to move freely with the fluid and not be influenced greatly by any outside forces. At the exact instant that the flow field is illuminated, an image of the field is taken by a highly sensitive digital camera that is equipped with a charge coupled device, or CCD, sensor. These images are transferred onto a computer, where they are analyzed by a special PIV calculation program (such as DaVis).

Figure A-1 shows the principle of the PIV method.

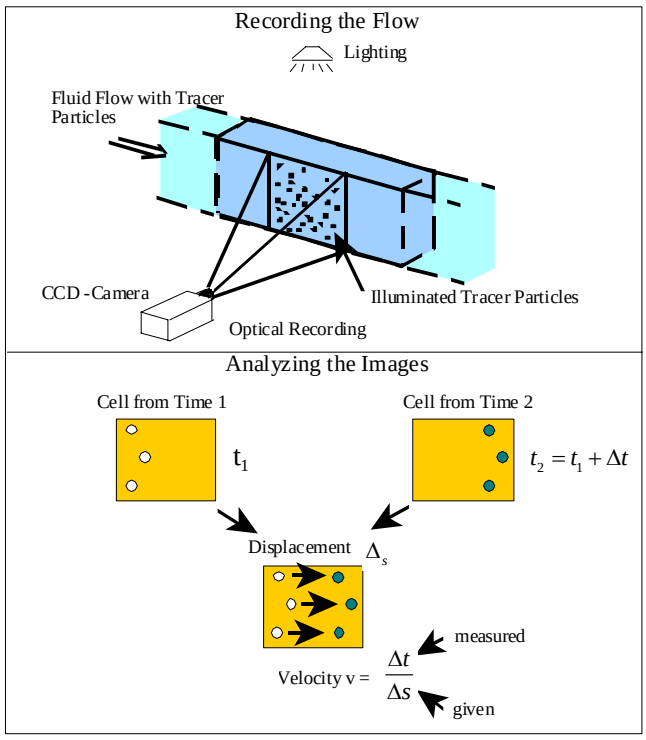

Figure A-1: The Principle of Particle Image Velocimetry (modified from Bleck, 2001)

1. Theoretical Background

The technical and mathematical background behind PIV is briefly explained in the following paragraphs.

1.1 Tracer Particles:

The PIV method would be impossible without tracer particles and therefore, selection of the particles used in experiments is of the utmost importance. The fluid mechanical properties of the particles must be determined to see if they will yield correct results. Two equations are useful in determining the particle's behavior under the influence of acceleration. The first (Eq. 1) is used to determine the gravitationally induced velocity $\boldsymbol{U_g}$ and is derived from Stokes' drag law. It is assumed that the particles are spherical and in a viscous fluid with a very low Reynolds number. We have:

$$U_g = d_p^2 \frac{(\rho_p - \rho)}{18\mu} g \qquad (1)$$

where d_p is the diameter of the particle, ρ_p and ρ are the densities of the particle and the fluid, respectively, μ is the dynamic viscosity of the fluid, and g the acceleration due to gravity. Similarly, Eq. 2 is used to derive an estimate of the velocity lag of a particle that is in 1a fluid with constant acceleration, a:

$$U_s = U_p - U = d_p^2 \frac{(\rho_p - \rho)}{18\mu} a \qquad (2)$$

with U_p and U being the particle and fluid velocities, respectively.

Another very important characteristic of the tracer particles is their ability to scatter light. The tracer particles used in a PIV experiment should ideally reflect as much light as possible, since the intensity of the particle image is what is used in the PIV analysis. Mie's theory of scattering gives the intensity of reflected light, q, is a function of the particle's diameter, d_p, and the wavelength of the light, λ.

$$q = \frac{\pi d_p}{\lambda} \qquad (3)$$

Since the wavelength of light used in the experiment should be constant, it is necessary to use particles with as large a diameter as possible to reflect the most amount of light. However, referring to equations 1 and 2, which deal with fluid mechanics, one would want to use as small a particle diameter as possible. It is with all these equations in mind that the tracer particles must be selected. It is necessary to choose a particle whose diameter is small enough so that its fluid mechanical properties are close to that of the fluid, but also large enough to reflect a sufficient amount of light for analysis.

1.2. Digital Image Recording

Nowadays, images are recorded using digital cameras, with which images are immediately available for inspection. The digital cameras used for PIV analysis are equipped with an electronic sensor called a charge coupled device (CCD). A CCD sensor (generally an array of many individual CCD elements) converts light, or more specifically, photons, into an electric charge, or electrons. An individual CCD element is called a pixel (from picture element) and it is on the order of 10 x 10 μm^2 in size. In other words, there are 100 pixels per mm.

Figure A-2 shows a simplified cross-section of a pixel. The CCD consists of a semi-conductive substrate, below the substrate are three layers: an insulating oxide layer, followed by an n-layer (an anode), followed by a p-layer (a cathode). An electric field in the semi-conductor is generated by applying a small voltage between the metal conductors. If a photon enters the p-n junction in the semiconductor, an electron-hole pair is created (the photoelectric effect). The hole is absorbed in the p-layer and the electron moves into the potential well (an area below the center of the pixel which is characterized by a lack of electrons), where it is then stored.

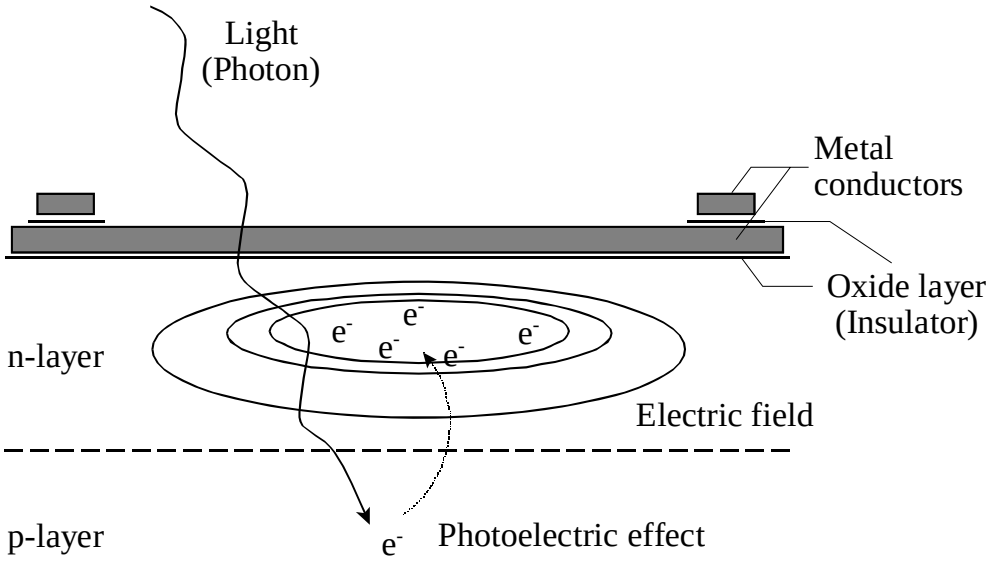

Figure A-2: Simplified Model of a Pixel (modified from Bleck, 2001)

A problem that is associated with all electronic devices is electronic noise. In electronic imaging, noise can be quite significant, because the visual perception of the image is corrupted. It is often necessary to go to great lengths to reduce the amount of noise that will be picked up by the CCD sensor, especially while performing PIV experiments. Background noise can often be only slightly less intense than the light scattered off of the tracer particles, making it extremely difficult to perform analysis on the images.

There are four main types of CCD sensors: standard, or full-frame CCD, frame transfer CCD, partial-frame interline transfer CCD, and full-frame interline transfer CCD (used at LWI). Figure A-3 shows the layout for all four of these types.

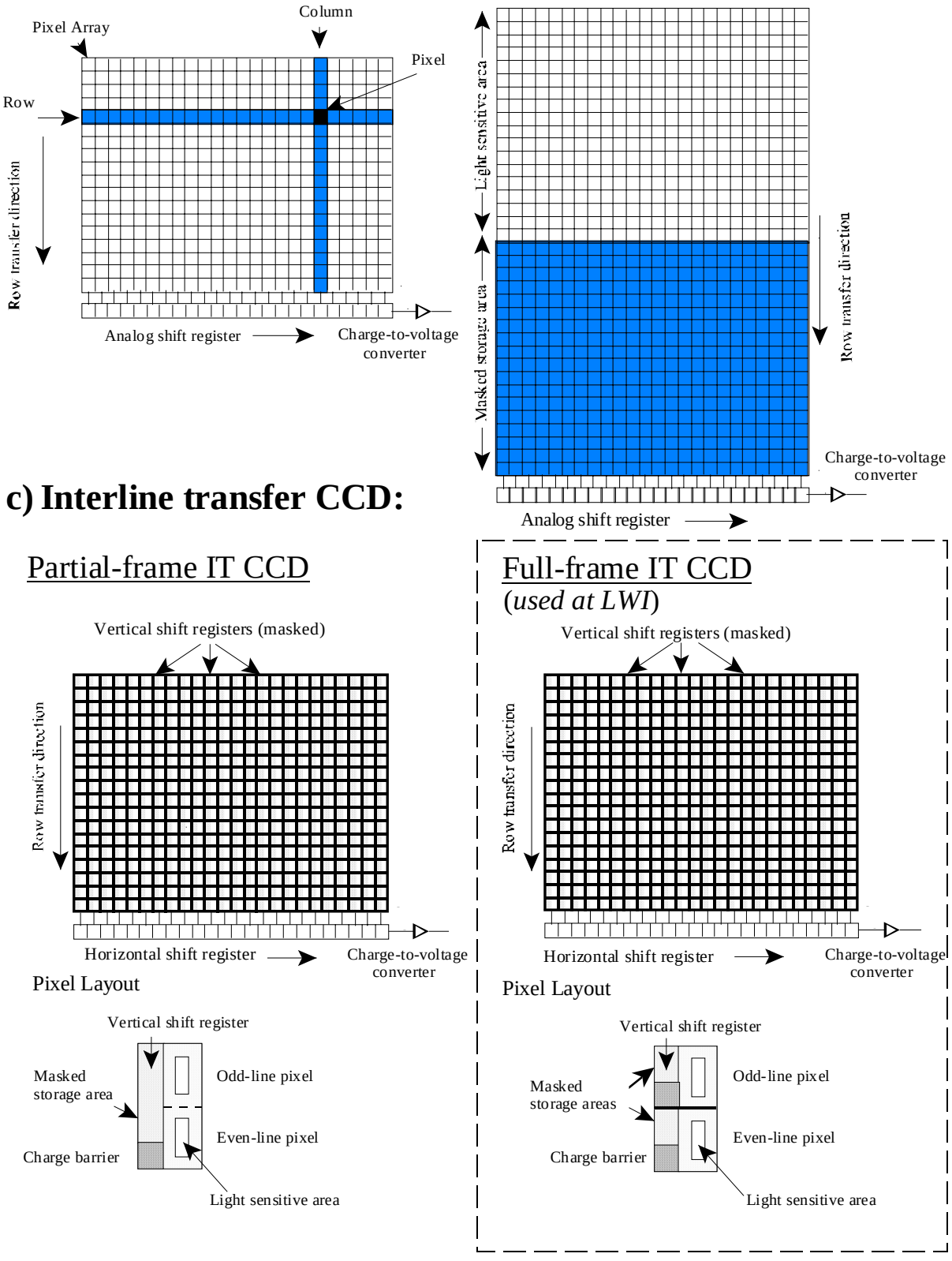

Figure A-3: Layout of the Four Types of CCD Sensors

For more information on the operation of each different type of CCD sensors, refer to section 4.2 of the PIV book by Raffel et al.

1.4 Mathematical Background of PIV Image Evaluation

When evaluating images for PIV analysis, it first must be determined which method, auto- or cross-correlation, will be used. Given an image that contains information from two instances in time (double exposure), one would use the auto-correlation method. If the information is contained on two separate images, then the cross-correlation method would be used. Once this is determined, then the correlation function can be found.

For the cross-correlation method, two pictures are being analyzed. The first image is at time t_0 and has a size of *M x N* pixels. The second image has the same size and shows time $t_0 + \Delta t$. There is a spatial transformation between the two images (between *f(M,N)* and *g(M,N)*), which will be referred to as the displacement field. This displacement field is what is needed to calculate the velocity vector field. Each image is broken up into smaller interrogation cells of size *m x n* pixels. Next the interrogation cells from the first image, *f(m,n)*, are compared to the corresponding cells of the second image, *g(i,j)*, where *i* and *j* are equal to *m* and *n*, respectively. The result is a displacement vector *(i-m, j-n)*. If one knows the time between the images, then one only needs to divide the displacement vector by the given time to determine the velocity vector.

The continuous cross-correlation function for the two-dimensional case is:

$$\Phi_{fg}(x,y) = \int_{-\infty}^{\infty}\int_{-\infty}^{\infty} f(\xi + x, \zeta + y) g(\xi,\zeta) d\xi d\zeta \qquad (4)$$

However, since the digital images are not continuous, we must use the discrete cross-correlation function:

$$\Phi_{fg}(m,n) = \sum_{k=-\infty}^{\infty}\sum_{l=-\infty}^{\infty} f(k+m, l+n) g(k,l) \qquad (5)$$

Given the fact that the images are of a finite size, we must also use a finite sum:

$$\Phi_{fg}(m,n) = \sum_{k}\sum_{l} f(k+m, l+n) g(k,l) \qquad (6)$$

In practice, executing these sums during PIV analysis would take an extremely long time, therefore they are performed numerically with a Fast-Fourier-Transformation, or FFT. Figure A-4 shows the mathematical procedure involved in PIV evaluation. The result of performing an FFT, $\hat{\boldsymbol{I}}$, multiplied by the complex conjugate of the inverse FFT, $\hat{\boldsymbol{I}}'^{*}$, will be the cross-correlation, ***R***:

$$R_{II} = \hat{I} \cdot \hat{I}'^{*} \; R_{II} = \hat{I} \cdot \hat{I}'^{*} \qquad (7)$$

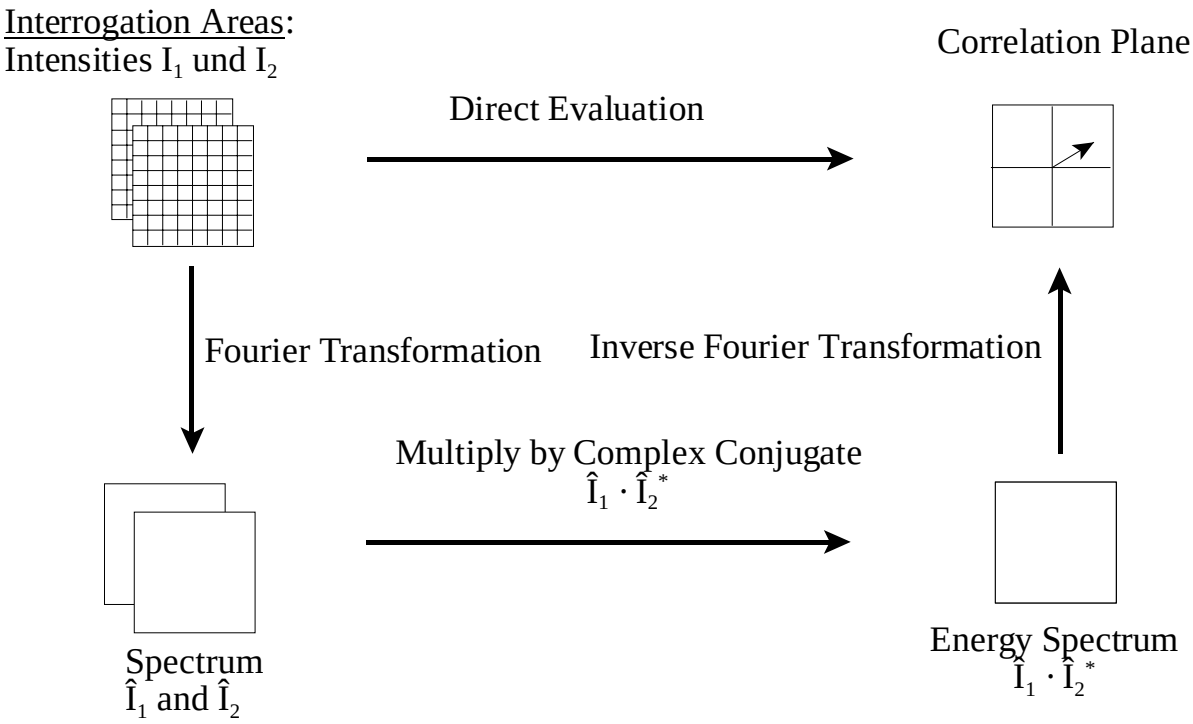

Figure A-4: Mathematical Procedure of PIV Evaluation

The highest peak in the x-y-plane given by the cross-correlation is the most likely displacement (Figure A-5). All the smaller peaks are background noise.

The continuous auto-correlation function is very similar to the continuous cross-correlation function (Eq. 4), however, instead of finding a correlation between two separate images, the auto-correlation function finds a correlation with itself. It is defined as:

$$\Phi_{ff}(x,y) = \int_{-\infty}^{\infty}\int_{-\infty}^{\infty} f(\xi + x, \zeta + y)\, f(\xi,\zeta) d\xi d\zeta \qquad (8)$$

Like the cross-correlation function, the continuous auto-correlation function must be reduced to a finite sum:

$$\Phi_{ff}(m,n) = \sum_{k}\sum_{l} f(k+m, l+n)\, f(k,l) \qquad (9)$$

Unlike cross-correlation, the highest peak given by the auto-correlation is not the displacement. The highest peak for an auto-correlation is always at (0,0) because the highest correlation of something is with itself. Therefore, the value of the second highest peak in the correlation plane is the most likely displacement. However, there are always two equal and symmetrical peaks in the auto-correlation plane. This is due to the directional uncertainty of the auto-correlation function. Figure A-5 shows an example of an auto-correlation plane (left) and a cross-correlation plane (right).

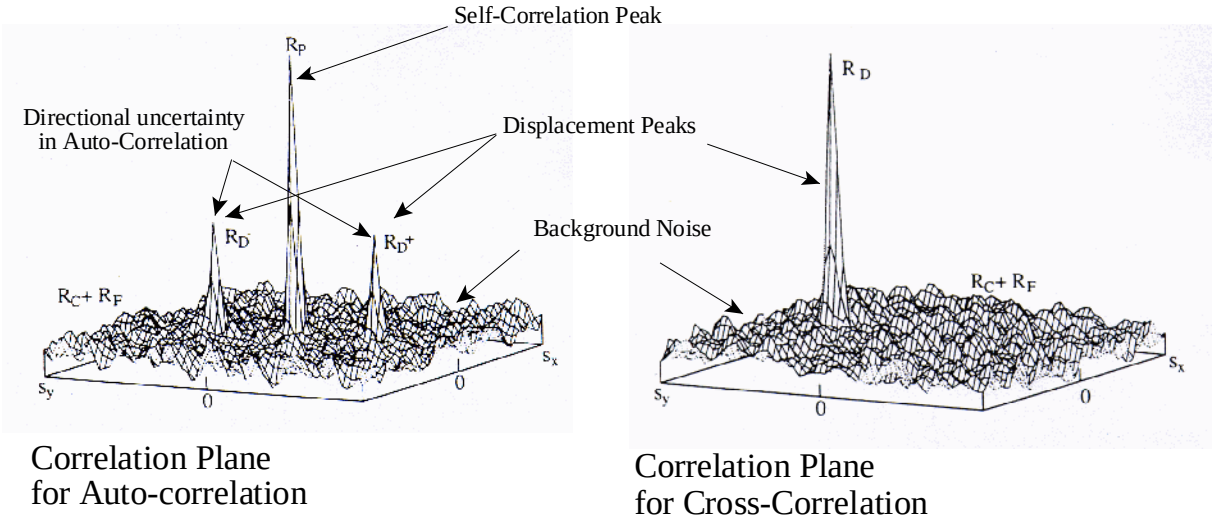

Figure A-5: Example of an Auto-correlation Plane (left) and a Cross-correlation Plane (right), (modified from Bleck, 2001)

References

LaVision 1999 DaVis PIV Manual; LaVision, Göttingen

LaVision 2000 PIV FlowMaster Manual; LaVision, Göttingen

Raffel, M.; Willert, C.; and Kompenhans, J. (1998) Particle Image Velocimetry – A Practical Guide; Springer Verlag, Berlin, Heidelberg, New York